Evaluation of microstructural and mechanical properties of multilayered materials

by

Samikshya Subedi

Submitted in partial fulfillment of the requirements for the degree of

Doctor of Philosophy

in

Materials Science and Engineering
Carnegie Mellon University
Pittsburgh, PA

Thesis Committee:

Professor Anthony D. Rollett (MSE, advisor)

Professor Marc DeGraef (MSE, CMU)

Professor Yoosuf Picard (MSE, CMU)

Professor Irene J. Beyerlein (MechE, UCSB)

Abstract

Microstructure controls many physical properties of a material such as strength, ductility, 1density, conductivity, which, in turn, determine the application of these materials. This thesis work focuses on studying microstructural features (such as grain size, shape, defects, orientation gradients) and mechanical properties (such as hardness and yield strength) of multilayered materials that have undergone different loading and/or operating conditions. Two materials that are studied in detail are 18 nm Cu-Nb nanolaminates and 3D printed Inconel 718.

Copper-Niobium (Cu-Nb) nanolaminate is a highly stable, high strength, nuclear irradiation resistant composite, which is destabilized with application of high pressure torsion (HPT). This work focuses on understanding the deformation and failure behavior of Cu-Nb using a novel orientation mapping technique in transmission electron microscopy in (TEM) called Automated Crystal Orientation Mapping (ACOM) and Digistar (ASTAR^{TM}) or Precession Electron Diffraction (PED). A new theory is postulated to explain strengthening mechanisms at the nanoscale using a data analytics approach. In-situ TEM compression and tensile testing is performed to image dislocation movement with the application of strain. This experiment was performed by Dr. Lakshmi Narayan Ramasubramanian at Xi'an Jiaotong University in China.

Another major aspect of this research focuses on the design, fabrication, and microstructural characterization of 3D printed Inconel 718 heat exchangers. Various heat exchanger designs, machine resolution, printing techniques such as build orientation, power, and velocity of the laser beam are explored. Microstructural and mechanical properties of printed parts (before and after heat treatment) are then analyzed to check

consistency in grain size, shape, porosity, hardness in relation to build height, scan parameters, and design. Various tools have been utilized such as scanning electron microscopy (SEM), electron backscatter diffraction (EBSD), x-ray computed micro-tomography (at Advanced Photon Source at Argonne National Lab), hardness and micro-pillar compression testing for this study.

Acknowledgements

This thesis would not have been possible without the contribution of many people. First and foremost, I would like to thank my advisor, Prof. Anthony D. Rollett for being the best advisor and for his endless guidance and support. His intellect, positivity and patience always inspire me. I sincerely would like to thank him for helping me grow intellectually and professionally. I would also like to thank my committee members, Prof. Irene Beyerlein, Prof. Marc DeGraef and Prof. Yoosuf Picard for their help, support and feedback. I am very grateful to have all of them on my committee. Special thanks to Irene for mentoring me at Los Alamos National Lab. I would also like to thank my former advisors, Prof. Brent L. Adams and Prof. David Fullwood for providing me undergraduate research opportunity and instigating the desire to do research in the field of materials science.

I am also indebted to Tom Nuhfer for helping me with ASTAR^{TM} work. I would like to extend my sincere gratitude to everyone who have helped me with additive manufacturing work, Colt Montgomery, Recep Onler, Sudhanshu Nahata, Luke Scime and Ed and John from machine shop. I should also thank all my collaborators that I have been very fortunate to work with, Prof. Richard LeSar from Iowa State University, Prof. Vinod Narayanan and Dr. Erfan Rasouli from University of California, Davis, Dr. Lakshmi Narayan Ramasubramanian from Carnegie Mellon University and Prof. Javier LLorca, Dr. Jon Molina and Alberto Palomares from University of Madrid at Spain. Their contribution has been very crucial to my thesis, thank you! I would also like to thank my undergraduate students, Shuchen Cong, Edward Cao, Cajer Gong, Kimberly Justl,

who have helped me with metallography and other works. I enjoyed working with you all.

Shivram Kashyap, Tugce Ozturk, Dr. Brian Gockel, Dr. Brian Lin, Dr. Sean Donegan, Dr. Reeju Pokharel, Dr. Ben Anglin, Dr. Clayton Stein, Ross Cunningham, Dr. Megha Jampani, Deepoo Kumar, Ming Tang, thank you. You guys made my PhD cheerful, memorable and intellectually fulfilling. Special thanks to Sudipto Mandal for always being there, and always willing to teach me (materials concept or anything else) and for helping me throughout, I am forever indebted to your help, support and friendship.

I would also like to thank my other friends in CMU and Pittsburgh, Monisha, Prabhat, Ankita, Samrachana, Amsul, Shreya, Suman, Prativa, Isha, Ichhuk, Tom, Gavin, Dikshya, Ali for your love and support. My PhD would not go with such ease without you and life outside of CMU would not have been the same.

This would all have not been possible, if it were not for my parents, Bhagwat and Kamala Subedi. Thank you for letting me pursue my dreams and being my biggest supporters. I would also like to thank my brother, Samip Subedi, for always inspiring me to do better and for motivating me, I cannot imagine my life without your support. I would also like to thank my fiancé, Ashish Kafle, for his unconditional love and support. You inspire me, support me, believe in me, lift me up when I am low, and above all, keep up with my PhD journey with same level of perseverance. Thank you for listening to all my talks about “dislocations" and “superalloys"! You are the best. I am also grateful to have a very loving family, Kumar, Prava, Amol, Smriti, Anusha and Shristi.

Lastly, I want to thank my funding sources, especially the US Department of Energy,

and materials science department at CMU without the support of which my thesis would not have been possible. Sincere thanks to all MSE staffs, mainly Adam, Jeanna, Suzy, Neetha, Val, Kelly, and Marygrace.

Samikshya Subedi

Jan 31st, 2017

Contents

List of Tables

List of Figures

List of symbols and abbreviations

σ_y	Yield Strength
σ^*	Critical Stress
τ_{Orowan}	Orowan Stress
σ_o, K	Hall-Petch Constants
(φ_1, ϕ, φ_2)	Euler Angles
G	Shear Modulus
ν	Poisson's ratio
b	Burger's vector
ARB	Accumulative Roll Bonding
AM	Additive Manufacturing
APS	Advanced Photon Source
ASTAR^{TM}	Automated Crystal Orientation Mapping (ACOM) and Digistar
CCD	Charge Coupled Device
CAD	Computer Aided Design
CI	Confidence Index
CLS	Confined Layer Slip

DED	Direct Energy Deposition
DMLS	Direct Metal Laser Sintering
$d\gamma$	Increment of shear Strain
EBSD	Electron Backscatter Diffraction
FIB	Focused Ion Beam
GNDs	Geometrically Necessary Dislocations
H-P	Hall-Petch
Hv	Hardness
HX	Heat Exchanger
HT	Heat Treatment
HPT	High Pressure Torsion
IQ	Image Quality
IPF	Inverse Pole Figure
KAM	Kernel Average Misorientation
KS	Kurdjumov-Sachs
h	Layer Thickness
MRD	Multiples of Random Distribution
ODF	Orientation Distribution Function
PVD	Physical Vapor Deposition
PBF	Powder Bed Fusion
PV	Power and Velocity

PED	Precision Electron Diffraction
ROI	Region of Interest
HRC	Rockwell Hardness C
SEM	Scanning Electron Microscopy
SLM	Selective Laser Melting
SPD	Severe Plastic Deformation
TEM	Transmission Electron Microscopy
UTS	Ultimate Tensile Strength
X-ray CT	X-ray Computed Tomography
XRD	X-ray Diffraction

Chapter 1

General Introduction

This thesis focuses on studying microstructural and mechanical properties of different metallic multilayered structures, such as Copper-Niobium (Cu-Nb) nanolaminates and 3D printed Inconel 718 superalloy. Due to its layer by layer fabrication technique 3D printed Inconel 718 is categorized as a multilayered material. Because of their unique fabrication methods (or loading conditions), each of these materials possess unique features that require careful and detailed investigation.

Accumulative roll bonding (ARB) fabricated Cu-Nb was studied in great detail in the past, however, mostly using conventional TEM techniques. In this work we introduce an orientation mapping technique in transmission electron microscopy (TEM) known as automated crystal orientation mapping (ACOM) and digistar (ASTAR^{TM}) to reveal microstructure of ARB material that has been destabilized by the application of another form of severe plastic deformation, i.e. high pressure torsion (HPT). ASTAR^{TM} is a very effective technique, which can capture diffraction patterns up to a resolution limit of 1 nm to resolve the orientation information. The provided map can be used to analyze texture, orientation gradients, orientation distribution function (ODF) and other microstructural features. This study helps to analyze the deformation behavior of these

nanolaminates and understand their extreme material properties. This work is the first attempt to characterize such highly deformed ultrafine-grained Cu-Nb materials, that have undergone two times of severe plastic deformation, using ASTAR a.k.a precession electron diffraction (PED).

The second chapter of this work focuses on strength behavior of nanolaminates. It is a well known fact that dislocations strongly control the strength of a material, whether that be the movement, pile-up or climbing of dislocations. Such a phenomenon is studied in the second part of this work by both data fitting and performing TEM experiments. It is important to understand the dislocation behavior in the nanoscale regime to accurately predict the materials strength behavior. For this, experimental data of various metal-metal nanolayers are collected from the literature and different strength theories are fitted to these data. Two competing theories, Confined Layer Slip (CLS) and Hall-Petch (H-P) theory, are studied in detail. It was found out that the CLS, one of the most discussed strength theory at a length scale of 5-50 nm, fails to accurately predict the strength behavior. Therefore, in this work, a new theory is formulated that can accurately explain strength behavior at the CLS range. In-situ experimental TEM work is also presented that shows the movement of dislocations during both compression and tensile tests.

The third and last chapter of this thesis presents a study of microstructural and mechanical properties of 3D printed Inconel 718. 3D printed IN 718 is referred to as multilayered materials, because of the way it is fabricated i.e. using a layer by layer deposition and melting technique via 3D printing. IN 718 is a nickel-chromium based high performance alloy that has high strength, corrosion and creep resistive properties at high temperature. Besides controlling the strength through grain size, shape, texture,

porosity and twin content, the strength in IN 718 is also controlled by the formation of γ and γ" precipitates. In this work we investigate each of these properties for a 3D printed Inconel 718. A laser based additive manufacturing is adopted, where the base plate is heated at a low temperature. Because of this, there is a high thermal gradient between each melting powder layer (which is at a very high temperature) and the previous layer that was melted. This results in rapid cooling and solidification of parts leading to unique materials properties such as very fine or no precipitates and heterogeneous microstructures. Different printing techniques, process parameters result in varied microstructural and mechanical properties, all of which have been investigated in this study. For both as-printed and heat treated IN 718, different characterization tools such as EBSD, SEM, X-ray computed tomography, micropillar compression test and hardness test have been used to thoroughly understand laser 3D printed IN 718 properties.

As a whole, we attempted to address some of the unanswered microstructure and strength related questions of these uniquely fabricated or highly deformed materials.

Note that each chapter has its own literature review, hypothesis, tools and techniques and results and discussion. The last chapter summarizes all the findings and outlines the future directions.

Chapter 2

Investigation of microstructural stability of Cu-Nb composites after high-pressure torsion (HPT)

2.1 Introduction

Nanoscale metallic multilayers are nanostructured materials composed of alternating layers of two or more different materials, as shown in Figure 2.1 [1]. The components of nanolaminates vary from metals to glasses to intermetallics to ceramics. There are different types of metallic nanolaminates pairs, that either have FCC-FCC lattices (Cu-Ni, Cu-Ag, Au-Ni, Ag-Ni, Ag-Cu, Al/Al_3C) [2, 3, 4, 5, 6] or FCC-BCC lattices (Cu-Nb, Fe-Pt, Cu-Fe, Cu-Cr, Cu-330 SS) [2, 3, 7] that are currently being explored. Depending on the choice of material for the bilayer, properties and mechanical responses change drastically. The interfaces can be classified as coherent, semi-coherent and incoherent depending on the lattice parameters at the contact plane [8]. If the two crystals at the interface plane match perfectly, the interface is called a coherent interface. An example of a coherent interface is (001) Cu-Ni plane. However, if the two crystals

have completely different atomic configurations at the interface, it is called an incoherent interface. Between coherent and incoherent is the semi-coherent interface, which has defect-free lattice at some places but lattice mismatch at other places [9]. In this study, we focus on Cu-Nb which has an incoherent interface system.

Multilayer metallic thin films have gained tremendous attention over the past few decades because of their extraordinary properties such as high conductivity, high strength, high irradiation damage resistance and resistance to deformation at large strains [9, 10, 11, 12, 13, 14, 15, 16, 17, 18]. High strength in these nanolaminates is achieved by a reduced layer thickness from the order of μm to nm, thereby increasing the density of interfaces and increasing resistance to dislocation transmission across interfaces [19]. Strength increases substantially during this process, i.e. it goes up from the order of MPa to GPa. Controlling laminate thickness (microstructure) thus helps control mechanical properties of materials.

In addition to strength, Cu-Nb nanocomposites have a high radiation damage tolerance unlike their single phase counterparts [11, 18]. The high density and incoherent nature of the interfaces in these nanolaminates act as a sink (sometimes referred to as a “super-sink") for annihilation and removal of helium bubble accumulation and radiation-induced defects, making it a nuclear irradiation resistive material. For this reason, it is also denoted as a “self-healing" material. Their high strength, high conductivity and light weight properties make Cu-Nb nanolaminates a very attractive material for automotive, energy, nuclear and high-strength applications, garnering the attention of scientists all over the world for over two decades [18].

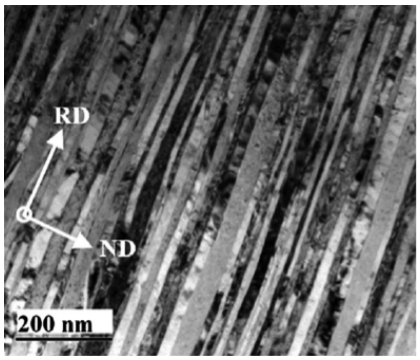

(a)

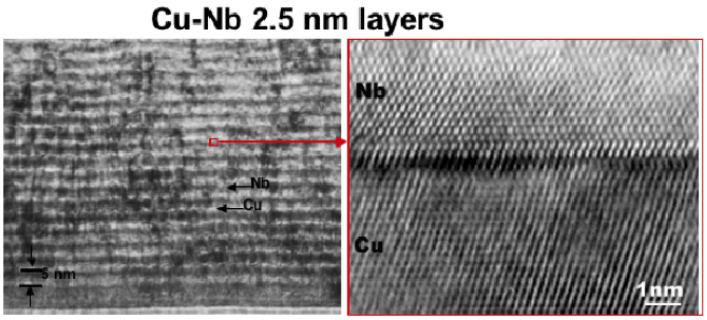

(b)

Figure 2.1: TEM image of a typical Accumulative roll bonded (ARB) Cu-Nb of thickness a) 17 nm [15] and b) 2.5 nm [20] showing Cu and Nb layers, rolling direction and interface lattices.

2.2 Motivation

Initially, the main motivation in highly deformed composites was to develop materials that have higher strength along with good ductility. For example, highly strained pearlitic steel, such as the one used in cable wires in bridges, car tires, and musical instrument strings, are one of the strongest nanostructured bulk materials with a tensile strength greater than 6 GPa [21]. ARB is one of the severe plastic deformation (SPD) processes that imposes ultrahigh plastic strain in sheet materials for producing nanoscale microstructure. The ARB process is used, in this work, to produce Cu-Nb

nanocomposites. Details on the fabrication method will be explained in the following section. ARB Cu-Nb nanolaminates with individual layer thickness of 10 nm have very high hardness (Hv = 4.13 GPa) and tensile strength ($\sim$ 2 GPa) which is about 5-10 times higher than either bulk Cu or Nb [11, 13]. They also have excellent thermal stability. Thus, ARB is an exceptionally efficient technique that combines two softer materials, with hardness in the range of MPa, and heavily rolls and strains them to produce a composite that have strength in the range of GPa. A comparison of ultimate tensile strength (UTS) between Cu and Nb and 18 nm layer thickness Cu-Nb nanocomposite is shown in Table 2.1.

Material	UTS
Copper	210 MPa
Niobium	325 MPa
Cu-Nb (18 nm)	1.7 GPa

Table 2.1: Strength of bulk Cu and Nb compared with nanocomposite Cu-Nb.

Although Cu-Nb nanolaminates can be applied to a wide variety of applications, it is also of crucial importance to test the materials' behavior at extreme physical conditions, beyond its normal service conditions. It is very important to see how the materials behave when the strain path changes from pure shear (during ARB) to simple shear (during HPT). HPT, to be discussed in detail later, is another form of severe plastic deformation where the sample is applied to both compressional (applied pressure) and torsional pressure at the same time. It is also worth mentioning that the initial idea with HPT was to homogenize a Cu-Nb composite by force mixing of dislocations or "super-diffusivity" under SPD, based on molecular dynamics (MD) simulation [22]. A homogeneous Cu-Nb alloy could be then treated as a regular nanocomposite whose

length scale can be controlled via the temperature at which the deformation takes place [22]. Recent experiments by Ekiz et al. revealed unusual localized shear patterns suggesting local shear velocity gradients within the thin film [15]. The focus of this work is to look into these destabilized “Z" and “S" shaped swirls and folds in order to examine distinctive features such as:

- Orientation
- Grain aspect ratio
- Layer thicknesses
- Intermixing of Cu and Nb

In this work, microstructural evolution and stability of Cu-Nb was tested to investigate whether there is atomic mixing of Cu and Nb, grain fragmentation or any unusual microstructural features after being subjected to HPT. For this, a novel microstructural characterization technique, ASTAR^{TM} or PED was employed for characterization of HPT microstructure. ASTAR^{TM} was first applied to unstrained Cu-Nb by Lui et al. and Carpenter et al. [17, 23]. But this is the first time ASTAR^{TM} has been applied to characterize highly strained material that has undergone two consecutive SPD. This work attempts to use ASTAR^{TM} to characterize texture, orientation and phase mapping of highly deformed Cu-Nb.

2.3 Background

2.3.1 Crystal orientations

Crystal orientations are represented as Euler angles. Euler angles are the three angle (φ_1, ϕ, and φ_2) required to bring the sample reference frame (normal direction (ND),

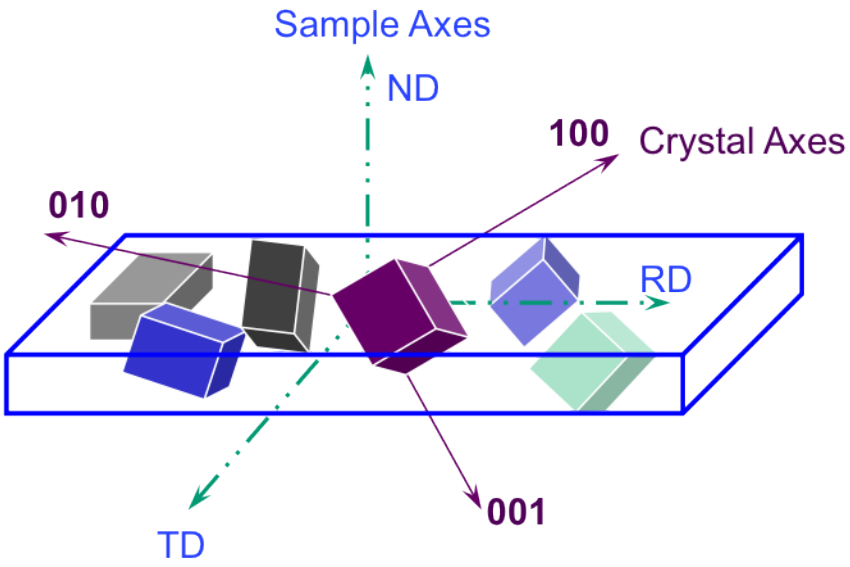

Figure 2.2: Representation of Euler angles [24].

rolling direction (RD) and transverse direction (TD)) to the crystal reference frame ((100), (010) and (001)). The sample and the crystal reference frames are shown in Figure 2.2. This convention is also called the Bunge Euler angle set. Here, first the sample axes is rotated about ND to get φ_1. Second, the sample axes is rotated about the new RD to get ϕ. And third, the sample axis is rotated about the new ND to get φ_2. Generally, orientation data can be obtained using X-ray diffraction (XRD) and electron backscatter diffraction (EBSD).

2.3.2 Physical vapor deposition (PVD)

Cu-Nb nanolayers were first fabricated using a PVD technique, where the vacuum deposition method was applied to sputter deposit Cu and Nb films on a silicon substrate [25]. The films are strongly textured with closed packed {111} plane of Cu parallel to closed packed {110} plane of Nb. Cu has a face-centered cubic crystal structure and Nb has a body-centered cubic structure. The interface created during PVD exhibits classical Kurdjumov-Sachs (K-S) orientation relationship, i.e ⟨110⟩ {111} Cu // ⟨111⟩

{110} Nb interface planes [13, 14, 18, 23, 25]. Due to the large miscibility gap between Cu and Nb, as shown in the Figure 2.3, and the lack of solid solubility, the mixture of Cu and Nb at the atomic scale is difficult [26]. As a result, Cu-Nb with sharp and clear interfaces are created. These interfaces also have a low energy and high stability [23].

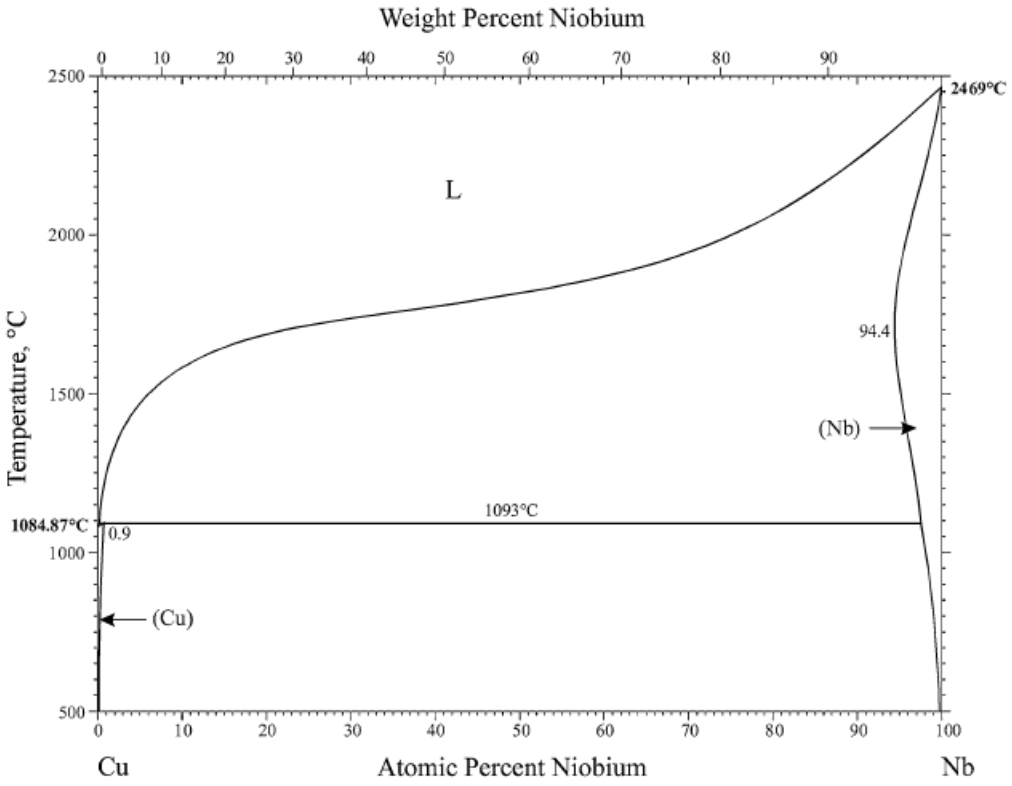

Figure 2.3: Cu-Nb phase diagram [26].

However, it was soon realized that the engineering applications using PVD samples were limited due to their extremely slow fabrication rate i.e. days to fabricate sample thicknesses of less than 1 mm [13]. Additionally, it is a relatively expensive technique. Production of bulk samples was not feasible. Thus, the focus shifted to synthesize Cu-Nb bulk samples using the ARB technique [27].

2.3.3 Accumulative roll bonding

ARB is a severe plastic deformation process, in which copper (99.99%) and niobium (99.94%) of equal thickness are stacked together and repeatedly rolled, cut, stacked and re-rolled until the desirable layer thicknesses for Cu and Nb are achieved, as shown in Figs. 2.4 and 2.5 [13].

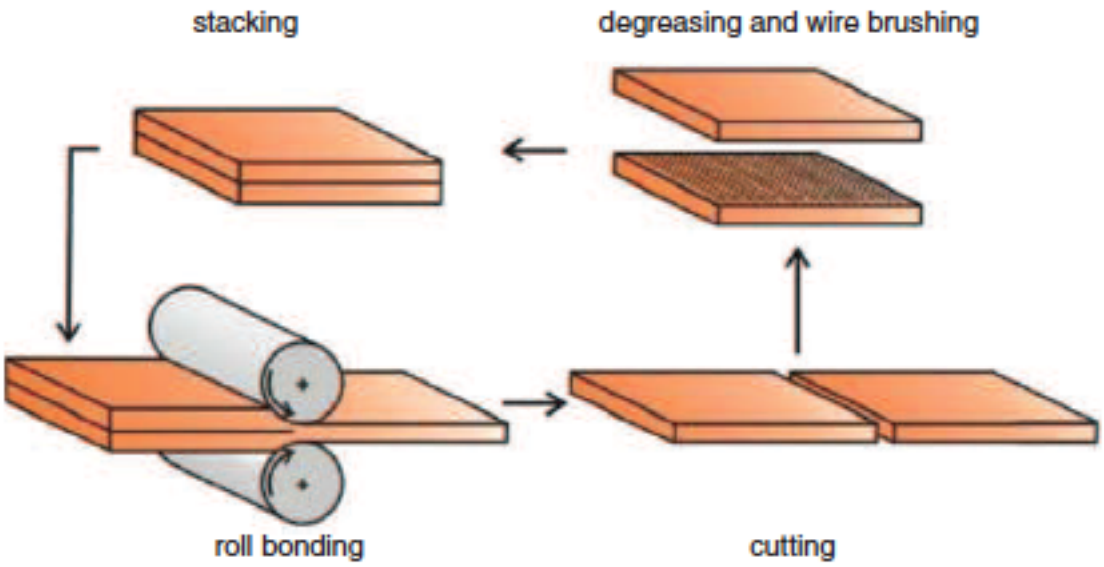

Figure 2.4: Schematics of ARB rolling process [28].

The list of layer thickness with their respective rolling reduction percentage and strain is shown in Table 2.2 [18]. In this study, Cu-Nb was rolled down to about 18 nm after applying 11.7 rolling strain. The Cu-Nb sample has 50/50 volume fraction of Cu and Nb.

In contrast to PVD, ARB fabricated Cu-Nb has a different interface relationship. Here {112} plane of Cu is parallel to {112} of Nb. Cu and Nb crystals are oriented with respect to each other within $<5^{\circ}$ of the Kurdjumov-Sachs (K-S) relation [13, 14, 25]:

$\langle 111 \rangle$ fcc // $\langle 110 \rangle$ bcc

$\langle 110 \rangle$ fcc // $\langle 111 \rangle$ bcc

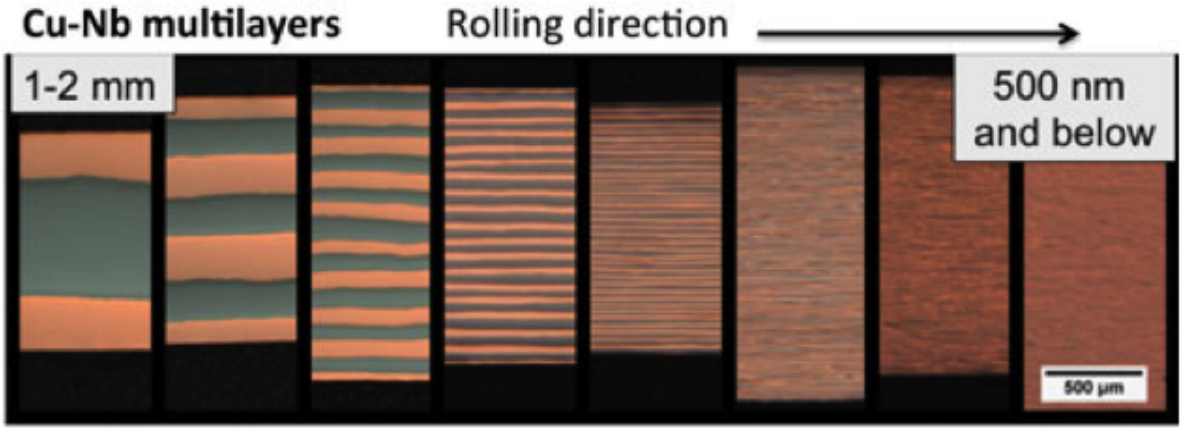

Figure 2.5: An example showing how during ARB process layer thickness become finer to about nm length scale [13].

2.3.4 Texture development after rolling

Texture is the alignment or orientation of crystals in a specific direction within a polycrystal. In other words, it is the anisotropy of the material where the crystallographic orientations are preferred in a certain direction.

2.3.4.1 Rolling texture in copper

3D Euler space is shown in Figure 2.6. Line diagram shows fibers typically found in rolled FCC and BCC metals. Rolling textures typically found in FCC material or Cu, in this case, is "α" and "β" fibers. At a low degrees of deformation, the α fiber is dominant and goes from Goss $\{110\}$ $\langle 001\rangle$ to Brass $\{110\}$ $\langle 112\rangle$ orientation. At high deformation β fiber is dominant that extends from Copper $\{112\}$ $\langle 111\rangle$ to S $\{123\}$ $\langle 634\rangle$ to Brass $\{110\}$ $\langle 112\rangle$ to Dillamore 'D' (Taylor) $\{4\ 4\ 11\}$ $\langle 11\ 11\ 8\rangle$ orientations [30]. The list of all possible FCC rolling texture components, their variations and corresponding indices and Euler angles (in the form of Bunge Euler angles) are show in Table 2.3 [31]. It has been highlighted that no individual component can clearly represent the texture of the

Layer thickness, h (nm)	Rolling reduction, η (%)	Strain, ϵ
20,00,000	0	0
97,000	95	3.03
45,000	97.75	3.79
20,600	98.9	4.58
7800	99.6	5.55
3500	99.8	6.34
1500	99.9	7.19
714	99.96	7.94
197	99.99	9.23
135	99.992	9.60
50	99.9975	10.60
31	99.9985	11.07
20	99.999	11.51
10	99.9995	12.21

Table 2.2: Layer thickness (h), rolling reduction (η) and strain (ϵ) estimation after ARB [18]

.

material. Therefore, it is more appropriate to represent rolling texture as fibers instead of individual components.

2.3.4.2 Rolling texture in niobium

A typical rolling texture components found in BCC or Nb are "α" and "γ" components. Alpha fiber components extend from Goss $\{110\}$ $\langle 001\rangle$ to Brass $\{110\}$ $\langle 112\rangle$ orientation

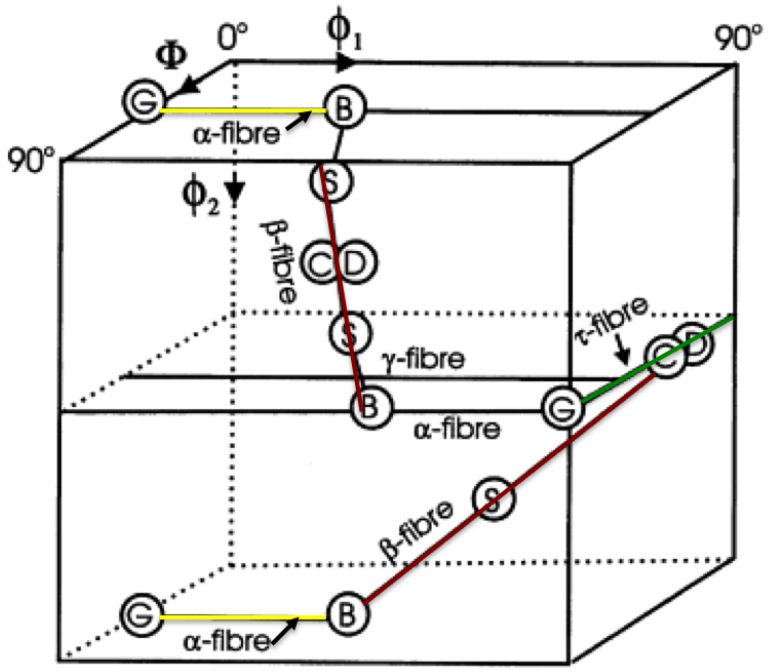

Figure 2.6: Schematics of 3D Euler or orientation space showing the α, β and γ fibers [29].

as shown in Figure 2.6. Similarly, gamma fiber extends from Copper to Goss to Brass to D orientation.

2.3.5 Orientation relationship/ Atomic arrangement of Cu-Nb interface

As shown in Table 2.3 and Table 2.4, there are 15 and 6 texture components possible for Cu and Nb respectively. Out of these, the copper component of Cu ($\{112\}\langle111\rangle$) joins with the I component of Nb $\{112\}\langle110\rangle$ in the interface [13]. This particular interface was shown to have the lowest interface formation energy and highest plastic stability among all possible rolling texture [13], according to the MD simulations. Another possible interface relationship is the Brass component of Cu parallel to the I-component of Nb, as reported by Beyerlein et al. [13] but at a very small frequency. Because of the

	Indices	Euler angles ϕ_1, φ, ϕ_2 (Bunge notation)
Copper/1st var.	$\{112\}\ \langle 11\overline{1}\rangle$	90, 35, 45
Copper/2nd Var.	$\{112\}\ \langle 11\overline{1}\rangle$	40, 65, 26
Brass/1st var.	$\{110\}\ \langle\overline{1}12\rangle$	35, 45, 0
Brass/2nd var.	$\{110\}\ \langle\overline{1}12\rangle$	55, 90, 45
Brass/3rd var.	$\{110\}\ \langle\overline{1}12\rangle$	35, 45, 90
S3	$\{123\}\ \langle 63\overline{4}\rangle$	59, 37, 27
S/1st var.	$\{312\}\ \langle 021\rangle$	32, 58, 18
S/2nd var.	$\{312\}\ \langle 021\rangle$	48, 75, 34
S/3rd var.	$\{312\}\ \langle 021\rangle$	64, 37, 63
Goss/1st var.	$\{110\}\ \langle 001\rangle$	0, 45, 0
Goss/ 2nd var.	$\{110\}\ \langle 001\rangle$	90, 90, 45
Goss/3rd var.	$\{110\}\ \langle 001\rangle$	0, 45, 90
Cube	$\{100\}\ \langle 001\rangle$	0, 0, 0
Dillamore 1st Var.	$\{4\ 4\ 11\}\ \langle 11\ 11\ \overline{8}\rangle$	90, 27, 45
Dillamore 2nd Var.	$\{4\ 4\ 11\}\ \langle 11\ 11\ \overline{8}\rangle$	42, 71, 20

Table 2.3: All possible FCC rolling texture components with their Euler angles [31].

high stability, interfaces formed after rolling them up to layer thickness of 18 nm are sharp and clear. ARB texture is highly stable even after rolling reductions of 99.999% strain [12, 18]. Schematics and TEM images of ARB rolled interfaces are shown in Figs. 2.7a and b respectively [13, 14].

{hkl}	⟨uvw⟩	Euler angles
001	110	45, 0, 0
211	011	51, 66, 63
111	011	60, 55, 45
111	112	90, 55, 45
11,11,8	4,4,11	90, 63, 45
110	110	0, 90, 45

Table 2.4: All possible BCC rolling texture components with their Euler angles. First three components {001}, {112} and {111} make α fiber and the rest make γ fiber.

2.4 High-pressure torsion

HPT is a form of severe plastic deformation where samples are subjected to both compression and torsional strain at the same time, as shown in Fig. 2.8. Depending on the number of turns provided by the anvil and radial location of the sample, the amount of strain applied varies. In this study, a sample from a 4 mm radius location was FIB cross sectioned, which corresponded to 50° turn and a 10.8 torsional strain [15]. This region had plenty of folds and swirls to explore. Sample thickness changed with increasing the number of turns, so it is denoted as a function of number of turns. At this location, the sample thickness was about 350 μm. The equation used for calculation is:

$$\text{Shear strain } (\mathrm{d}\gamma) = \frac{2\pi r \; d(N)}{T(N)} \tag{2.1}$$

where, r is the radius of the sample, d(N) is the number of turns applied by anvil, and T(N) is the change in thickness of sample depending on radial distance and the

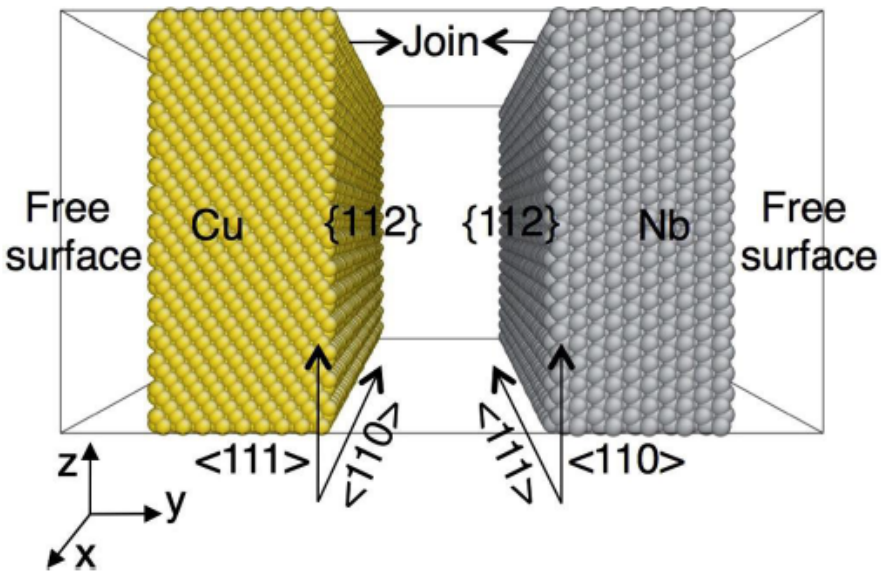

(a)

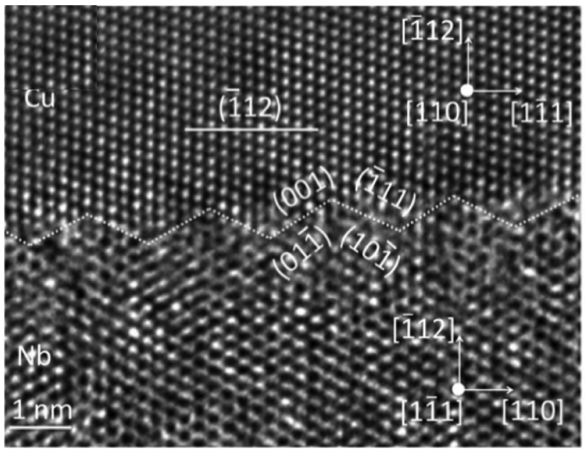

(b)

Figure 2.7: a) Schematics [14] and b) High-resolution transmission electron microscopy of {112}Cu//{112}Nb interface relationship [12].

number of turns.

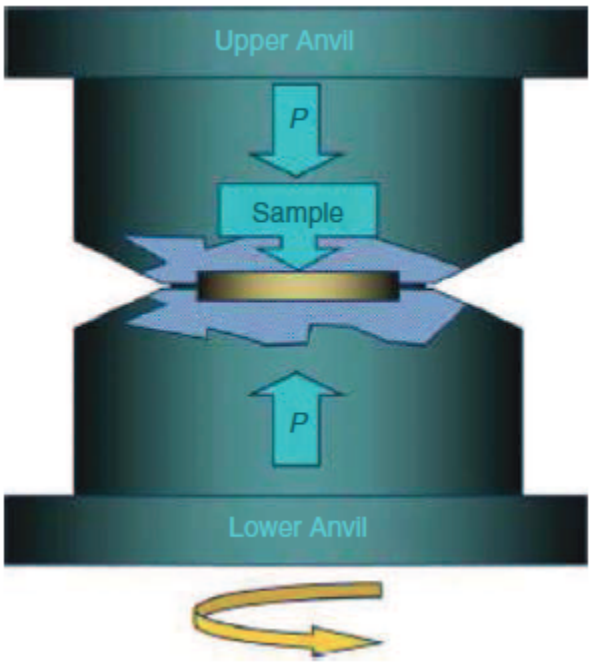

Figure 2.8: Schematics of a high-pressure torsion setup [28].

2.5 Hypothesis

Based on the stable lamellae deformation observed down to 18 nm by ARB, we hypothesize that there will be regular deformation i.e. no loss of the regularity of layers or orientation gradients under shear deformation imposed by HPT.

2.6 Characterization tools and techniques

2.6.1 Focused ion beam (FIB)

TEM samples were prepared using a conventional sample preparation technique called the FIB lift-out method. FIB stands for focused ion beam where the operating voltage of the machine is between 5 KV and 30 KV and current ranges from 1 nA to 65 pA. The steps

involved in sample preparation are the deposition of platinum over the selected region of interest (ROI) followed by ion milling ROI and attaching OmniProbe to the specimens to lift out the final thinning section. The lift out part is welded on half fold mesh TEM grids.

2.6.2 Transmission electron microscopy

TEM is a powerful microscope in which a beam of electrons, generally under a high accelerating voltage of around 200 KeV, is transmitted through a very thin sample and the image recorded in a charged couple device (CCD) sensor. The interaction between high energy electron and features in the sample leads to the acquisition of features that are as small as dislocations and even atoms in some cases. TEM operates on the principle on light microscopy except in this case electrons instead of light are used leading to smaller wavelength and resolution of finest details.

2.6.3 ASTAR^{TM}

ASTAR^{TM} is an orientation mapping technique installed in the Tecnai F20 TEM, located in the microscopy facility in the MSE department at CMU. The fundamental principles of this technique are very similar to EBSD, where for each scan point a diffraction pattern is collected and compared to a set of templates for that given material. In order to find out how good the match is between experimental and simulated diffraction patterns, a measurement index similar to confidence index is used. The higher the index value the better the match. Moreover, the software outputs .ang file which can be imported to TSL software to perform additional characterization as with any other TSL file.

An example of a typical Cu and Nb diffraction pattern is shown in Figure 2.9. Templates for Cu and Nb were calculated based on their lattice parameters and space

groups. For Cu the lattice parameters are a=b=c=0.3615 nm and the space group is Fm3m. Similarly for Nb, lattice parameters and space group are a=b=c=0.33 nm and Im3m respectively. Both Cu and Nb had 1326 templates. Each diffraction pattern was cross-correlated with these templates to get the highest correlation index value. The optimized camera length for orientation mapping was found to be 7.1 cm. A charge coupled device (CCD) camera was used for collection of the diffraction pattern. For more information on ASTAR^{TM} technique, the reader is directed to the Rauch et al. paper [32].

Using this technique a resolution of $\sim$ 1 nm could be achieved. By decreasing the spot size (1 being the largest spot size and 11 being the smallest in the Tecnai F20), the resolution could be improved further at the expense of beam intensity. This decrease in intensity may result in an unreliable indexing. Thus a spot size of 7 to 9 is preferred [33].

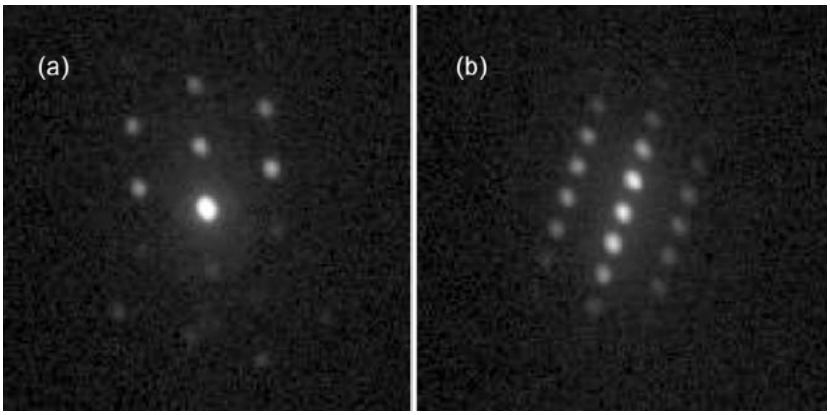

Figure 2.9: Diffraction pattern of a) Cu and b) Nb [23].

Some of the main crystallographic features that have been studied in this paper are inverse pole figure (IPF), kernel average disorientation (KAM), image quality (IQ) and confidence image (CI) maps.

2.6.3.1 Why ASTAR™?

The average layer thicknesses of Cu and Nb nanolaminates is 18 nm. It is obvious that the resolution of conventional orientation mapping, Electron Backscatter Diffraction (EBSD) Microscopy, is not sufficient to map the crystallographic features at this length-scale. EBSD has a spatial resolution on the order of 50 nm and angular resolution $\sim 0.5°$. TEM provides much better spatial resolution i.e. in the order of 1 nm with angular resolution $\sim 1°$ with a decrease in interaction volume. However, conventional TEM provides limited statistical information for reliable measurement of texture [23]. XRD, on the other hand, cannot provide sufficient spatial information as it gives more bulk information. Thus in order to characterize these special arrangements of high density interfaces and to perform the spatial texture study on them, ASTAR™ was adopted.

2.7 Microstructural representation

2.7.1 Inverse pole figure (IPF)

Crystallographic orientation is generally represented either in the form of a pole figure (PF) or inverse pole figure (IPF). Pole figure is the stereographic projection of the directions of crystallographic plane normals or "poles" in the sample reference frame. On the other hand, IPF is a stereographic projection of a sample direction plotted with respect to the crystal frame. Therefore, each point in the IPF triangle or each color in the IPF color map represents a specific sample direction.

2.7.2 Kernel average misorientation (KAM)

Kernel Average Misorientation (KAM) is one of the common microstructural metrics used to calculate local misorientation and defect concentration [34] in polycrystals. When a material is subjected to external load (plastic deformation), it responds by straining in ways that are heterogeneous at several length scales. At the grain scale one such response is the development of local misorientation or orientation gradients or dispersion in the change in orientation (i.e. texture development) of the grain at a local level. Misorientation development within the grain can be attributed to the increase in dislocation density [35, 36, 37] which are generated to accommodate local incompatibilities in crystallographic parameters. It has been shown that higher misorientation corresponds to higher defect accumulation in polycrystals and thus higher dislocation density [38, 39].

KAM for each point is calculated as the average misorientation angle between that point and its specified number of nearest neighbor or pixels (in 2D) and voxels (in 3D) [38, 40].

$$\text{KAM} = \langle\, \theta\, (\mathrm{g}_{\mathrm{point}},\, \mathrm{g}_{\mathrm{neighbor}}) \mid \theta < \psi \,\rangle$$

where, θ is the angle between the point and its neighbor. ψ is the threshold misorientation angle below which the values were excluded. KAM, in our case, was calculated up to the second nearest neighbors and any contributions to the KAM that exceeded a threshold value (ψ) of 5° were excluded assuming they correspond to a grain boundary. KAM is also used to analyze local strain [41], surface distortion [34], and to measure the stored energy [42].

2.7.3 Confidence index (CI)

Confidence Index (CI) value is an indication of how accurate the indexing of the diffraction pattern is and ranges from 0-1, 0 being the lowest and 1 being the highest.

2.7.4 Image quality (IQ)

Image Quality (IQ) is a measure of the sharpness of the diffraction patterns where higher IQ values imply better pattern quality [37].

2.8 Results and Discussions

After 10.8 torsional strain, fold or bend lamellae were found to be locally distributed. Examples of the folds observed using the TEM are shown in Figure 2.10.

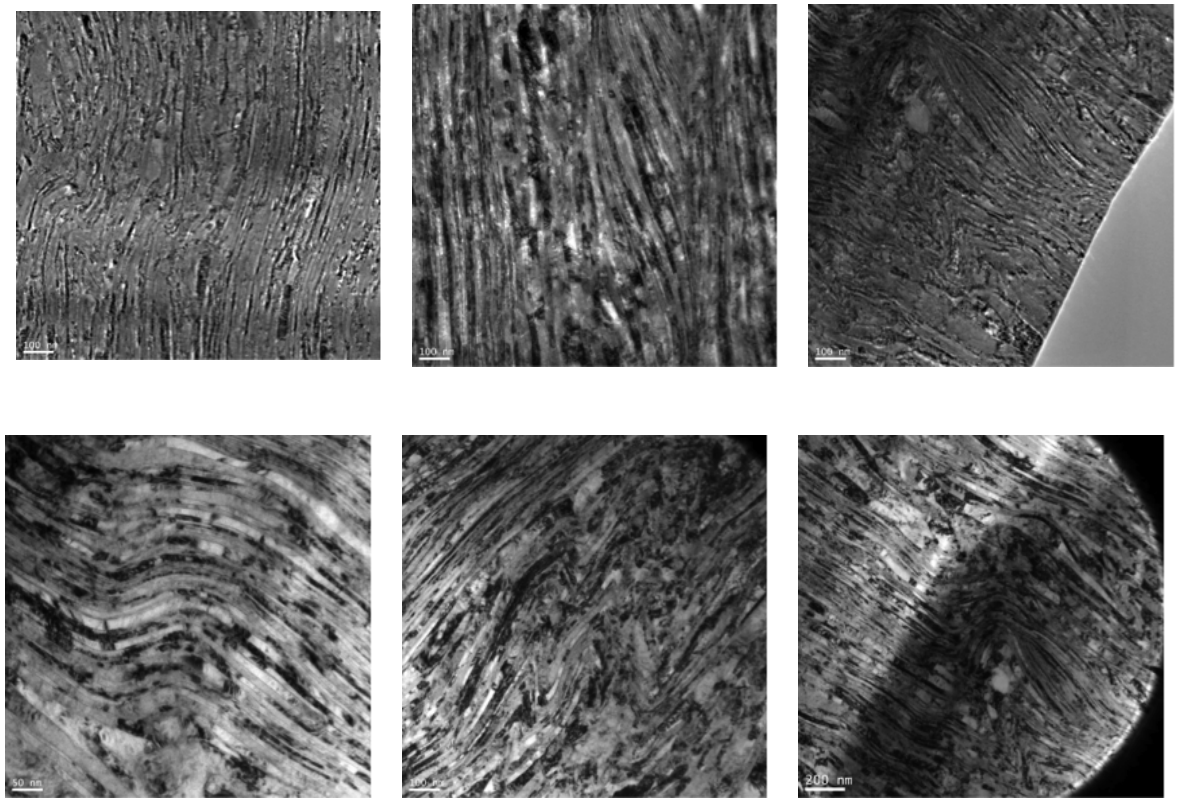

Figure 2.10: TEM images of different layers and folds.

In previous work, when analyzing macro-texture using X-Ray Diffraction (XRD), it was observed that the ARB texture destabilized to be shear texture unlike either Cu or Nb after 10.8 HPT [15]. Neither did the K-S orientation relationship sustain. The

texture in the ODFs was very weak compared to ARB. However, this was looking into the bulk Cu-Nb or macro-texture. The resolution of XRD is not sufficient to locally resolve the folds information which were locally distributed. Thus, ASTAR^{TM} was required to characterize it spatially. Using TEM, different types of folds were observed and hence categorized into:

1. Wavy lamellae
2. Bend/incipient folds
3. Fully developed folds

2.8.1 Wavy lamellae

The wavy lamellae are neither straight nor bend folds. IPF, KAM, CI, IQ, and phase maps are drawn for two wavy lamellae maps (named as wavy lamellae 1 and 2) and analyzed.

2.8.1.1 Wavy lamellae 1

ASTAR^{TM} analysis on wavy lamellae 1, as shown in Figure 2.11 is presented as follows:

- The IPF map, in Figure 2.11a, reveal that the layers are randomly oriented and orientation gradients are observed in each layer. In some layers, small misorientations can be observed with slight changes in color whereas in the other layers, large misorientations are observed indicating the formation of new grains.
- The layer thickness of both Copper and Niobium is not uniform post-HPT. Some layers are sandwiched between the other two neighboring layers and some layers

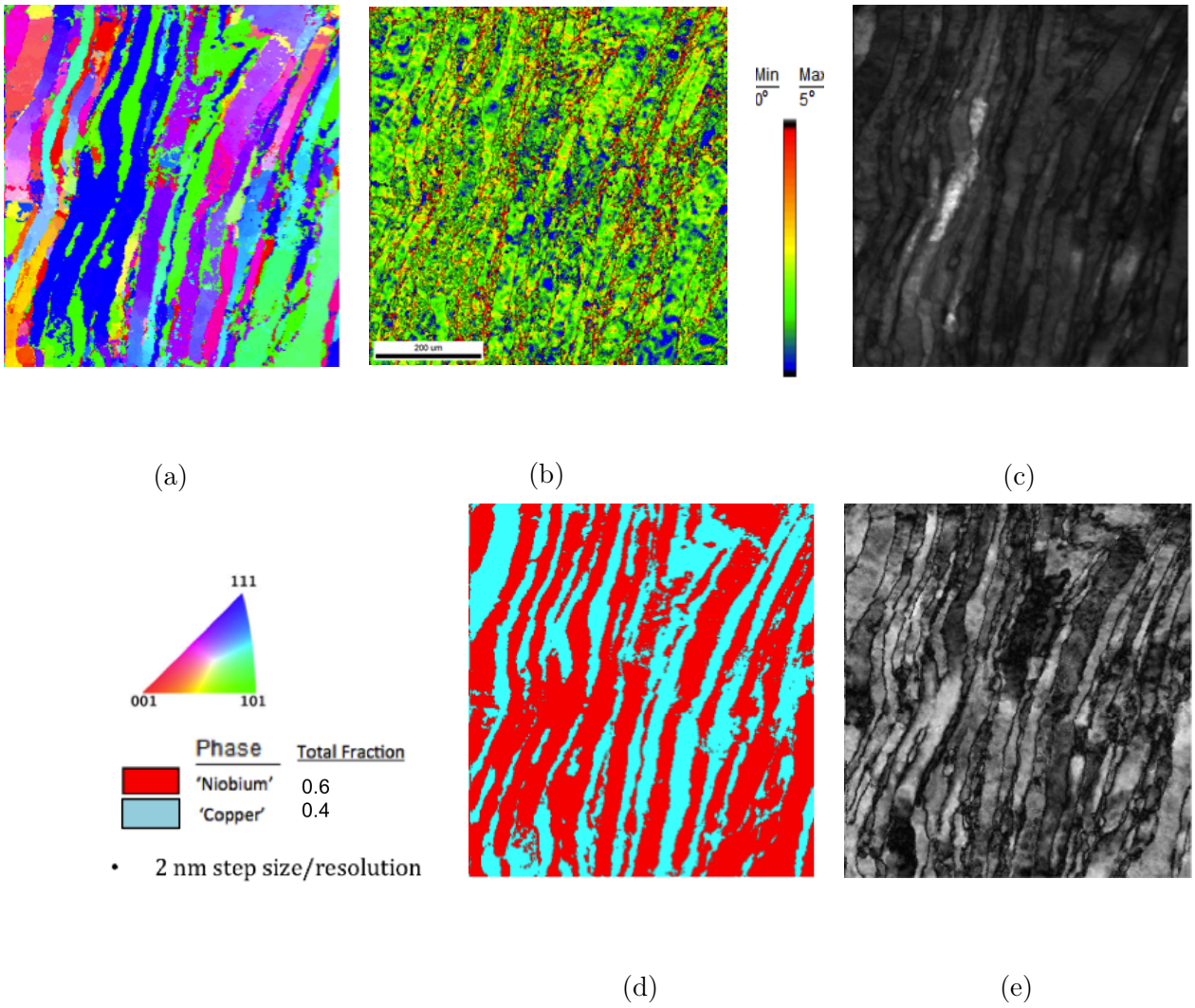

Figure 2.11: ASTAR^{TM} images of wavy lamellae 1 showing a) IPF b) KAM c) virtual bright field/IQ images d) phase and e) reliability/CI maps. The length-scales for all the other maps are same as shown in KAM map.

have coarsened. Even within the same layer, the thickness was found to be inconsistent. Note that a 2 nm step size was used, so any feature below this length-scale cannot be resolved.

- Interfaces are not very sharp or clear. This could be due to overlap of boundaries or intermixing of phase. Intermixing of phases is suggested by the area fraction of copper (0.61) and niobium (0.39) which should ideally have been 50/50. However,

one should keep in mind that at the interfaces, patterns are overlapped which makes it difficult for the software to index the phases properly. The development of nonuniform and large strain gradient layers could have resulted in unclear boundaries.

- Area fraction of Niobium is greater than of Copper. This could be because Cu is softer (hardness 369 MPa) than Niobium (1320 MPa) and may have deformed more.

- KAM map, in Figure 2.11b, shows that the thinner the layer, the higher the KAM values are, as indicated by the red color from the KAM color code. Mostly, high KAM values are observed near the interfaces. Generally, a high KAM value signifies high dislocation content. However, at this layer thickness, the dislocation source to obstacle distance is small enough to prevent dislocations from piling against the interface. Therefore, accumulation of dislocations is not a valid argument. This leads us to question whether there is a possibility of elastic bending or forest dislocation accumulation at the interface. This topic is discussed in more detail later in the chapter 3.

A	$\{1\bar{1}1\}\ \langle 110\rangle$	C	$\{001\}\ \langle 110\rangle$
$\overline{A}$	$\{\bar{1}1\bar{1}\}\ \langle\bar{1}\bar{1}0\rangle$	D_1	$\{1\bar{2}1\}\ \langle 111\rangle$
A_1*	$\{\bar{1}\bar{1}1\}\ \langle 112\rangle$	D_2	$\{\bar{1}\bar{1}2\}\ \langle 111\rangle$
A_2*	$\{11\bar{1}\}\ \langle 112\rangle$	E	$\{0\bar{1}1\}\ \langle 111\rangle$
B	$\{1\bar{1}2\}\ \langle 110\rangle$	$\overline{E}$	$\{01\bar{1}\}\ \langle\bar{1}\bar{1}\bar{1}\rangle$
$\overline{B}$	$\{\bar{1}1\bar{2}\}\ \langle\bar{1}\bar{1}0\rangle$	F*	$\{110\}\ \langle 001\rangle$
$\overline{J}$	$\{1\bar{1}0\}\ \langle\bar{1}\bar{1}2\rangle$	J	$\{0\bar{1}1\}\ \langle\bar{2}11\rangle$

Table 2.5: Notation and Miller indices for different ideal orientations.

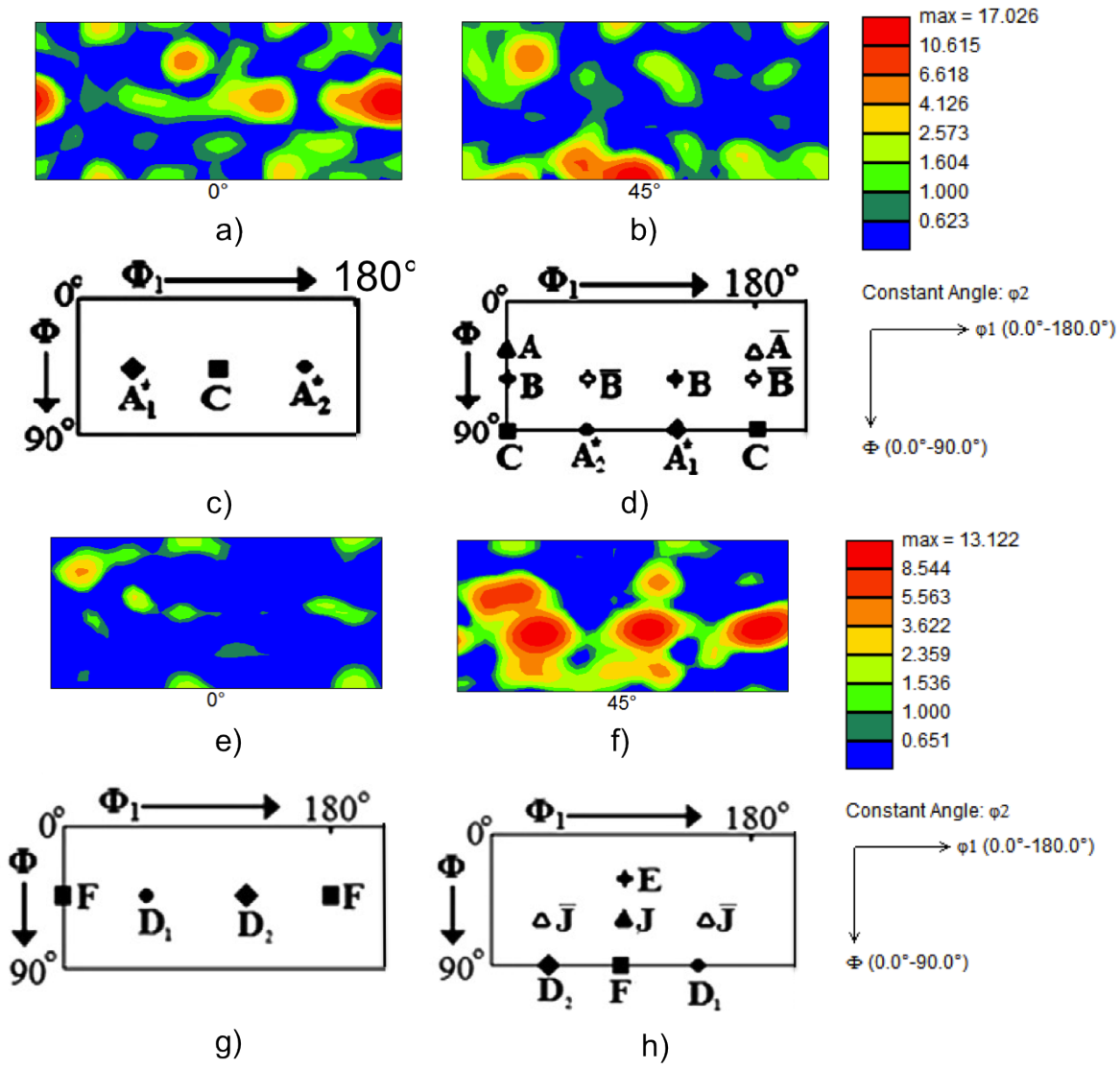

Figure 2.12: Evolution of texture for wavy lamellae 1 after HPT. a) $\varphi_2 = 0°$, b) $\varphi_2 = 45°$ sections of the Cu phase orientation distribution function (ODF) after HPT, compared against ideal simple shear components c) $\varphi_2 = 0°$ and d) $\varphi_2 = 45°$. Similarly, e) and f) are HPT Nb ODFs compared with ideal shear components of Nb at g) $\varphi_2 = 0°$ and h) $\varphi_2 = 45°$ respectively.

ODF of wavy lamellae 1:

In addition to the initial assessment of texture, shape and size, misorientation and area fraction of nanolayers, a further study is done using an orientation distribution

function (ODF). An ODF is a 3-dimensional representation of material texture where two Euler angles (φ_1, ϕ) are kept constant and slices are taken in the third direction i.e. φ_2. An ODF is preferred over other texture representative plots such as pole figure because it gives complete 3-D texture information without losing any information.

Shear components of wavy lamellae 1 were compared to ideal shear orientations for copper and niobium for $\varphi_1 = 0^o$ and 45^o slices, as shown in Figure 2.12. The corresponding plane and direction for each of the ideal components is shown in Table 2.5. A_2* $\{11\bar{1}\}$ $\langle 112\rangle$ and C $\{001\}$ $\langle 110\rangle$ of Cu have the highest intensity as indicated by the MRD value of 17 and ∼4 respectively. Here, texture strength or the degree of preferred lattice orientation is measured in units of MRD. MRD refers to multiples of random distribution, which suggest how strong the texture is. 17 MRD means that the texture is 17 times stronger than if it were to be random. Both of these components have shifted spatially.

Nb has the highest intensity of $\overline{J}$ $\{1\bar{1}0\}$ $\langle\overline{1}\overline{1}2\rangle$ and J $\{0\bar{1}1\}$ $\langle\bar{2}\ 1\ 1\rangle$ components, as shown in Figure 2.12 h. D_1 or D_2 components are not seen. Faint E components and possibly F components are also observed. This indicates that the ARB texture is destabilized and there are some components of shear texture found at this strain but not all.

2.8.1.2 Wavy lamellae 2

ASTAR^{TM} analysis, in Figure 2.13 of wavy lamellae 2 showed similar observations as wavy lamellae 1. The orientation distribution was heterogeneous. The KAM map revealed high KAM mostly near the interface. Unequal volume fractions of Cu and Nb were observed, i.e. Cu = 0.6 and Nb = 0.4. Cu was coarser and had a higher area fraction.

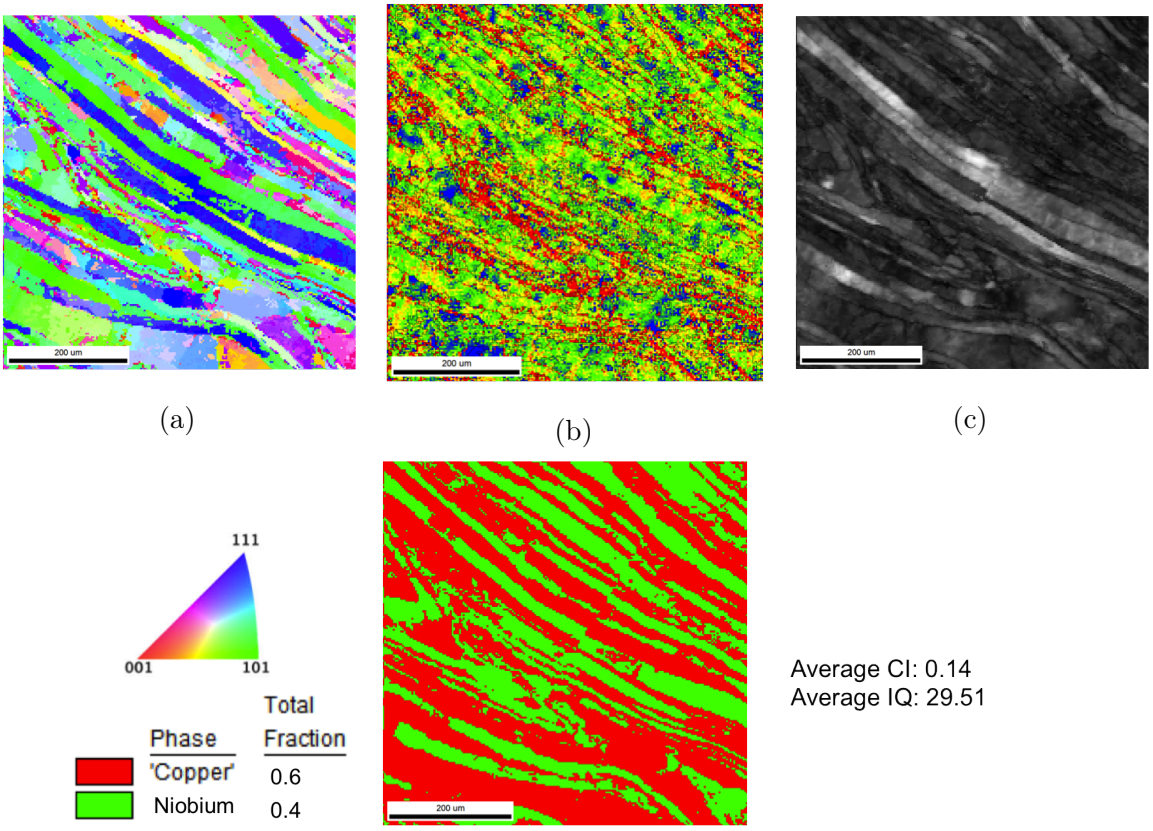

Figure 2.13: ASTAR^{TM} images of wavy lamellae 2 showing a)IPF b) KAM c) virtual bright field/IQ images d) phase.

ODF of wavy lamellae 2:

Similar to wavy lamellae 1, A_2* and C components are present in ODF of Cu as shown in Figure 2.14a and b. Additionally, A1* component is also present. All the components have shifted from their ideal location. Nb has a strong intensity of the $\overline{J}$ and J components. A faint D_2 component is seen (in both Figure 2.14e and Figure 2.14f) but no E, F and D_1 components were observed.

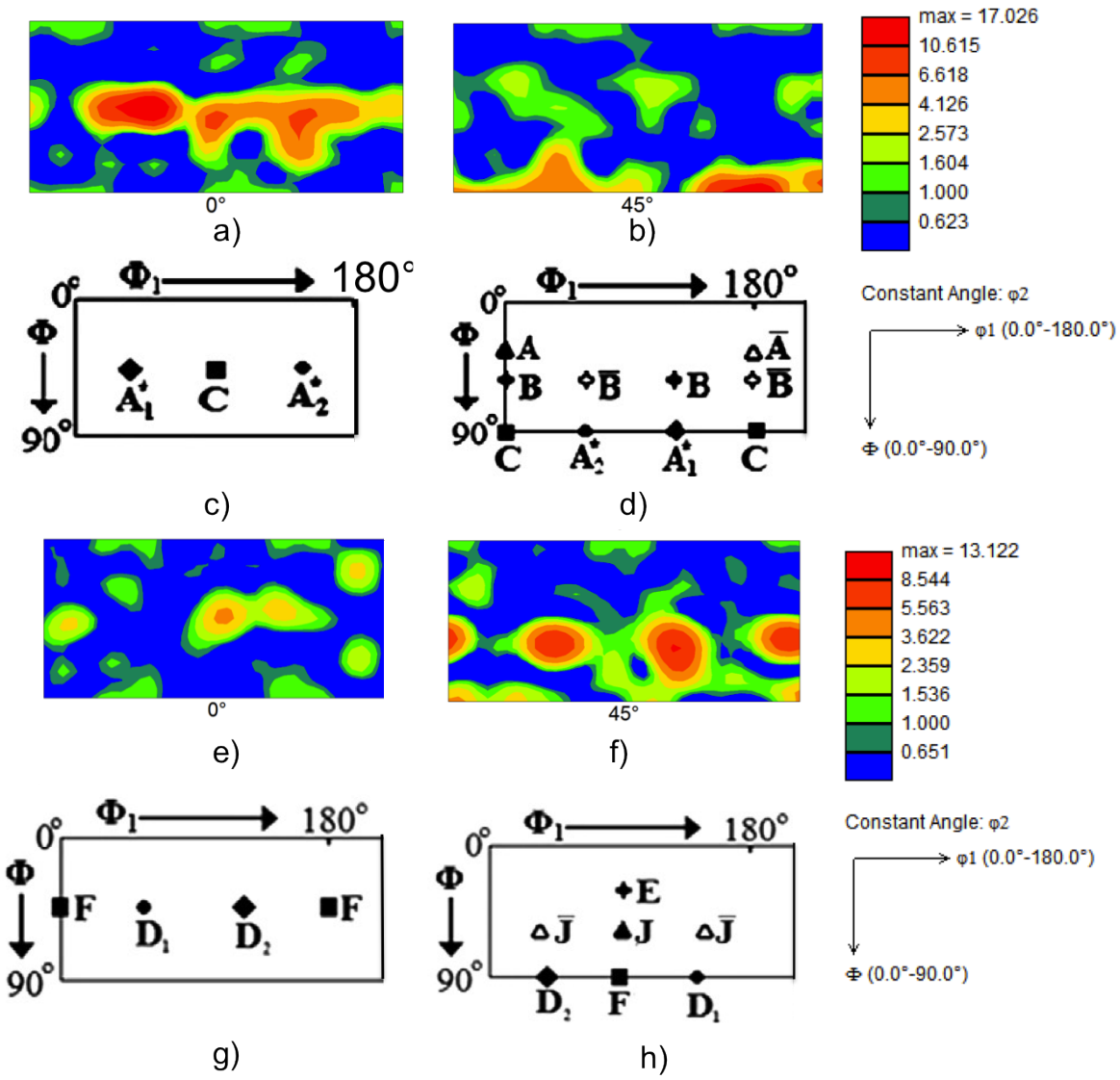

Figure 2.14: Evolution of texture of wavy lamellae 2 after HPT. a) $\varphi_2 = 0°$, b) $\varphi_2 = 45°$ sections of the Cu phase orientation distribution function (ODF) after HPT, compared against ideal simple shear components c) $\varphi_2 = 0°$ and d) $\varphi_2 = 45°$. Similarly, e) and f) are HPT Nb ODFs compared with ideal shear components g) and h) at at 0° and 45° respectively.

2.8.2 Bends/incipient folds

This section investigates bend folds. The fold structure here resemble shear folds. They look slightly more bent than the wavy folds but were not as bent as fully developed

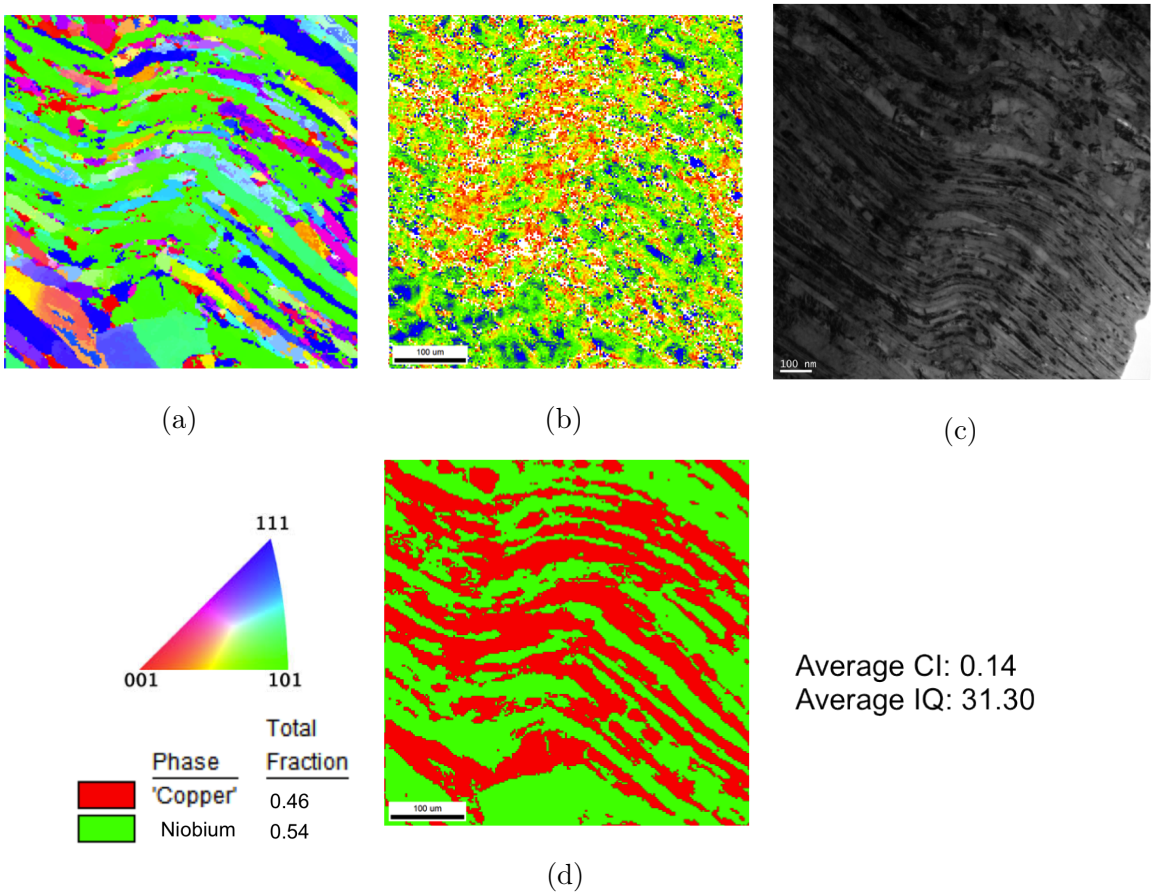

Figure 2.15: ASTAR^{TM} images of bend folds showing a) IPF b) KAM c) TEM image and d) phase.

folds. The IPF map revealed that most of the crystals are oriented in the ⟨101⟩ direction, as shown by the green color that corresponds to ⟨101⟩ direction in the IPF color map, which is also shown in Figure 2.15. Large misorientation gradients are observed in each layer. Unlike wavy lamellae, this category of lamellae has high KAM developed in the layers as well as near the interfaces.

ODF of bend folds:

- Texture for copper is strong and is comparable to that of wavy lamellae. MRD values are comparable in both types of folds. The shear components of Cu in this

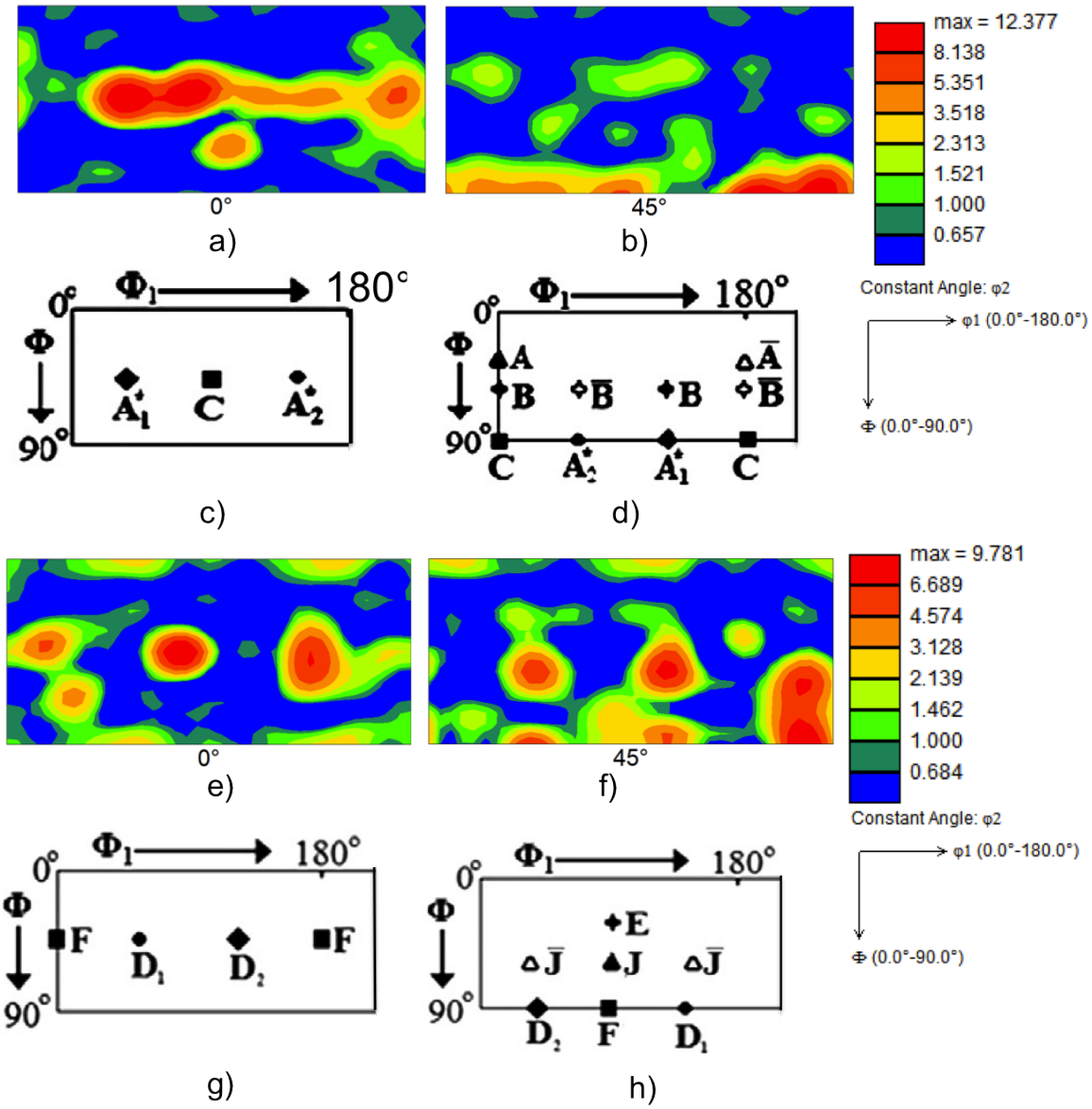

Figure 2.16: Evolution of texture after HPT. a) $\varphi_2 = 0°$, b) $\varphi_2 = 45°$ sections of the Cu phase orientation distribution function (ODF) after HPT, compared against ideal simple shear components c) $\varphi_2 = 0°$ and d) $\varphi_2 = 45°$. Similarly, e) and f) are HPT Nb ODFs compared with ideal shear components g) and h) at at 0° and 45° respectively.

case looks more like a band. Stronger A1*, C and A2* components are observed for both $\varphi_2 = 0°$ and 45° shown in Figure 2.16a, b c and d. Some of the B components appeared in Figure 2.16b but are very faint.

- For Nb, besides having J and $\overline{J}$ components, there is a strong intensity of F, D_1 and D_2 components as shown in Figure 2.16e. It is worth noticing that these components are still at a small offset from their ideal locations.

- To sum up, as the layers were bent to a higher degree, more components appeared. This suggests that with an increase in applied strain, there is an apparent increase in localized shear strain.

2.8.3 Fully developed folds

In this section, fully developed folds are presented. As shown in Figure 2.17, these type of folds are much more bent than the previous two types. They look like “z" and “s" shaped folds. Due to the complex nature of this fold, it was divided into three different sections as shown in Figure 2.18. Sections 1) and 2) are long and elongated interfaces that are the part of the same fold but have kinked after HPT. They have relatively small orientation gradients in them. The aspect ratio of layers is high and each layer appears to be very thin. They are highly textured in the {111} and {110} directions. On the other hand, section 3 and other peripheral layers are divided into multiple different layers and thus have a smaller aspect ratio. They also have high gradients in them making the layers less textured. Layer thickness in section 3 is coarser than in sections 1) and 2). Volume fraction of both copper and niobium seem to be 50/50, therefore, no intermixing is suggested.

ODF of fully developed folds:

- In section 1) and 2), layers are highly textured as indicated by the MRD value of ∼35. This is a very high value compared to the earlier scans, which was in the ragne of 13. Section 1 has a very strong intensity (MRD = 41) of A_1* and C components and faint B components for copper. For Nb, the line of J components are seen with faint D_2 and F components. Again, the components are either shifted

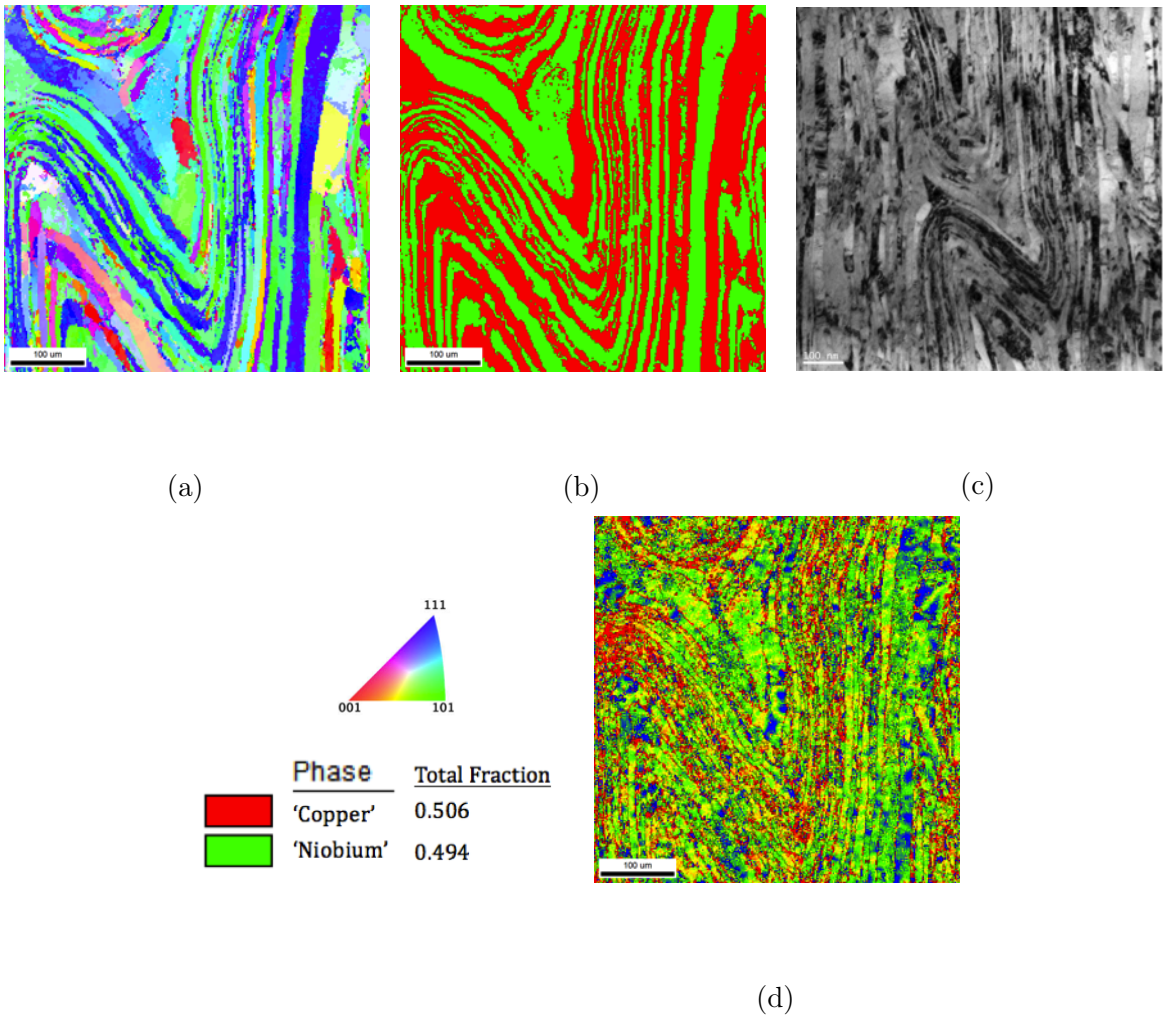

Figure 2.17: a) IPF b) Phase and d) KAM map of fully developed folds. c) TEM image of the same section.

horizontally or vertically from their ideal locations. Similarly, section 2 has very strong A_1*, C and A_2* components of Cu and very strong J and $\overline{J}$ components for Niobium. All other components are faint.

Section 3, that have a mixture of many orientations, suggesting development of many shear components after HPT. It is difficult to determine which exact components are present. This section may suffer from the harmonic analysis because there are so few orientations, i.e. false peaks appear. Therefore, discrete plots are better albeit messier.

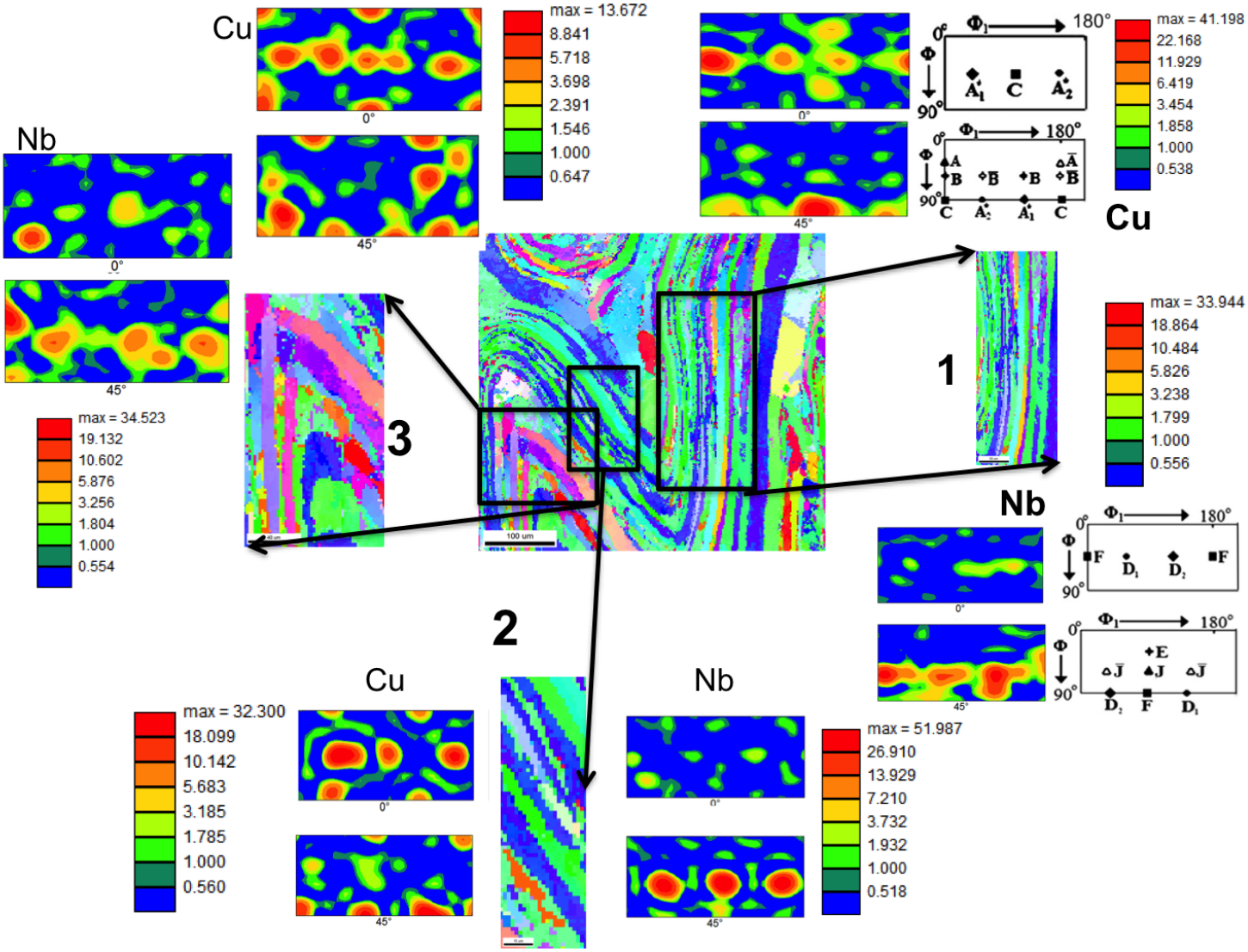

Figure 2.18: IPF map of a fully developed fold divided into parts 1) and 2) which seem more elongated and textured with thinner layer spacing and 3) which has more random and equiaxed grains.

In overall, as shown in the ODF of the entire scan in Figure 2.19, A_1*, C and A_2* components of Cu have the strongest intensity with a fiberlike texture. And for Nb, J, $\overline{J}$, D_1 and D_2 have the strong intensity with faint F component.

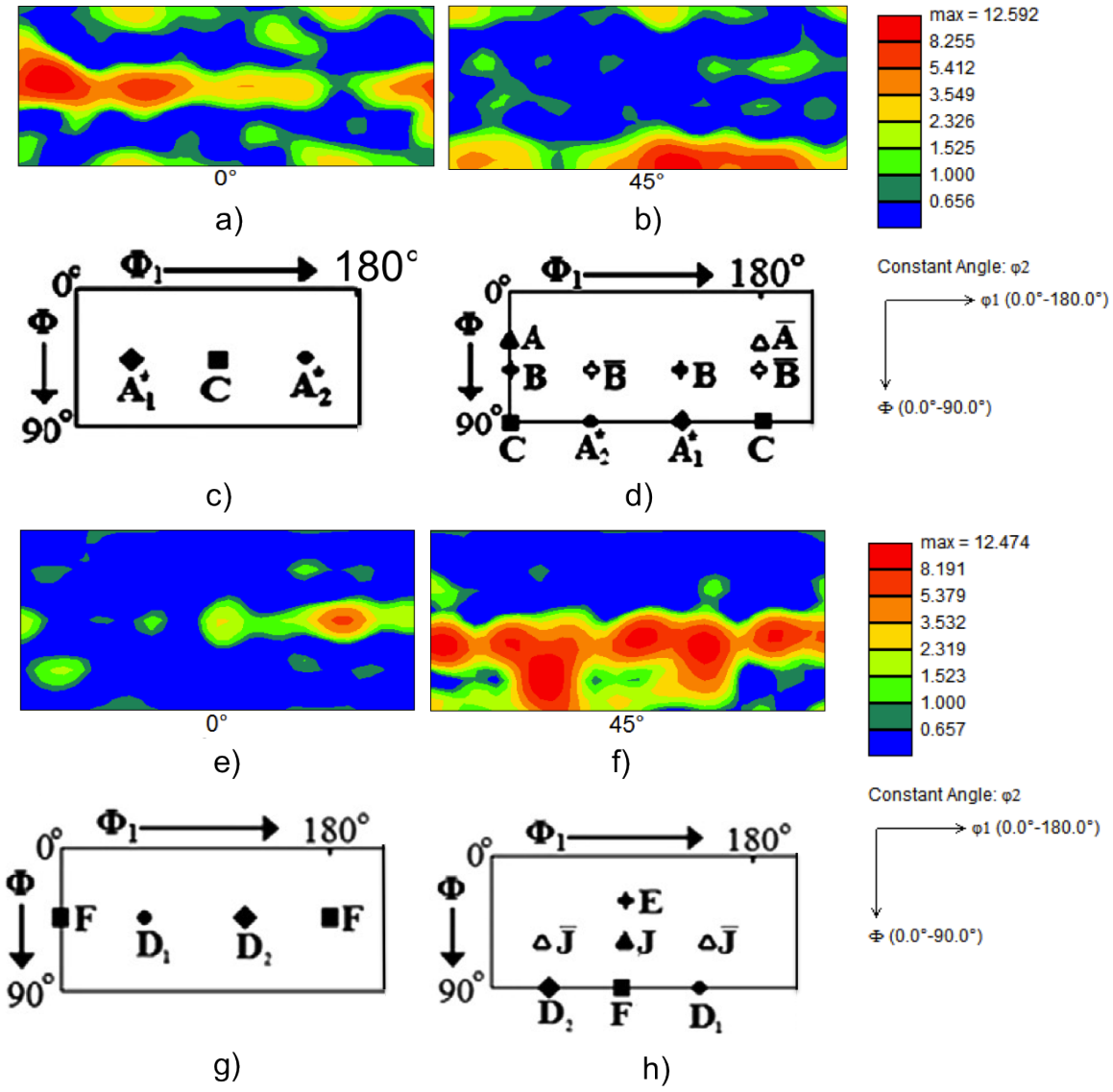

Figure 2.19: ODF for entire scan for fully developed fold.

2.9 Hypothesis revisited

Although ARB Cu-Nb has a stable interface structure up to an individual layer thickness of 18 nm, with the application of shear deformation by HPT, shear folds and layer fragmentations were observed. {112} Cu ∥ {112} Nb orientation relationship no longer holds true.

2.10 Conclusion

Results from XRD from the previous work showed that the texture developed during ARB was largely destabilized at a strain of 10.8 strain for both copper and niobium. The intensity developed was weaker than ARB. However, using XRD there were no signs of shear texture after HPT. In this work, using ASTAR^{TM}, local features as small as 2 nm were resolved for texture and phase mapping. ARB texture was found to be destabilized to form shear texture.

Some of the key findings of the folds analysis are as follows:

1. For all three different kinds of folds (wavy, bend and fully developed lamellae) strong A_1*, A_2* and C components were found except in wavy lamellae 1 case where there was no A_1*. Similarly, for Nb in all three cases, J and $\overline{J}$ orientation had the strongest intensity. Depending on the type of the folds, other faint intensity components such as E, D_2, D_1 and F appear inconsistently.

   Overall, there is enough evidence to show that these folds are the results of shear deformation. It is interesting to note that although {111}Cu‖{110}Nb are the closed packed planes, during ARB {112}Cu‖{112}Nb had the lowest formation energy hence the orientation relationship. However, after HPT, {111}Cu and {110}Nb components dominated instead of {112}, which is more similar to the orientation relationships observed in PVD composites.

2. Copper layers had some missing shear components such as B. Similarly, Niobium had components such as E, D_1 and D_2 missing or at a very low intensity.

3. Depending on the amount of strain (corresponding to the type of the folds), some components appeared or disappeared. This suggests that there must be a strain

dependence of the shear components.

4. It was observed that the thinner the lamellae, the higher the misorientation. The thinner regions appear more intact than the outside regions which have more grain fragmentation and a smaller aspect ratio.

5. The fraction of each phase was not 50/50 after 10.8 strain. Niobium, in general, has a larger volume fraction, which could be because it is harder than copper and remained intact during the deformation. Unequal volume fraction also signifies that some regions are sufficiently inter-mixed or interfaces are overlapped such that ASTAR^{TM} could not index them as a separate and distinct Cu or Nb phase.

2.11 Future work

Some of the future works that are recommended in connection with the ASTAR^{TM} work are presented below:

1. Investigation on coarsening behavior of different phases (either Cu or Nb)

   As shown in Figure 2.20 coarsening of Nb phase has been observed. The area fraction of Cu was 0.37 and Nb was 0.63. However, in some other cases coarsening of Cu was also observed. In order to investigate more into what causes this, further study is required to analyze the coarsening behavior.

2. It is worth investigating the orientation relationships across the Cu-Nb interface after HPT. Our results suggest that it changed from that observed in the ARB material [25].

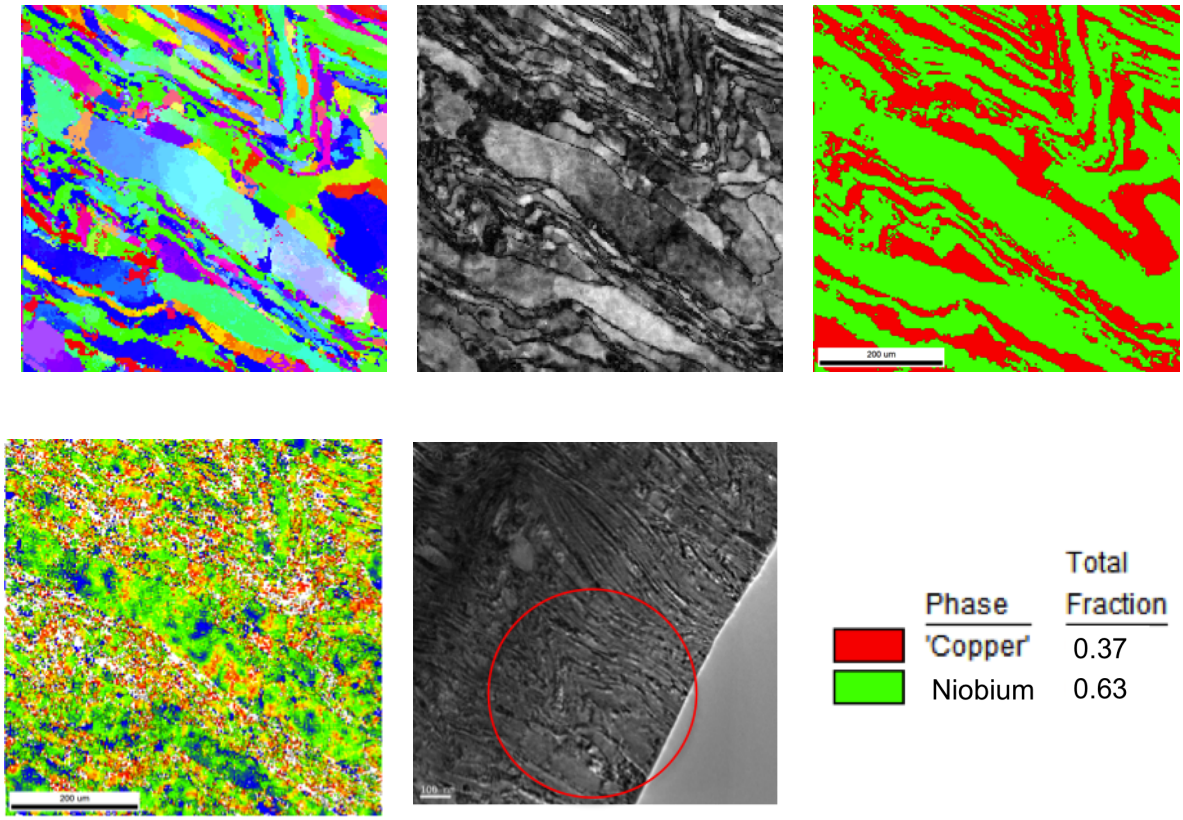

Figure 2.20: ASTAR^{TM} maps of a scan showing coarsening of phases, in this case, Niobium. Note: Phase 1 is Niobium.

3. Possibility of elastic bending

KAM results for most of the maps suggest that thinner the layers, higher the misorientation. However, at such a small layer thickness, dislocation accumulation is less likely. The layers could possibly be experiencing elastic bending. Therefore, the next step will be to investigate KAM distribution before HPT in these laminates.

With application of High resolution TEM, dislocation density will be computed in each layer to investigate whether there is an accumulation of dislocations or just 1-2 dislocations in each individual layer.

4. Study of the 4.2 and 6.5 strain regions can be done to have a deeper understanding of initiation of folds as the current study only focuses on the material at the highest strain of 10.8 strain.

Chapter 3

Strength of Nanoscale Metallic Multilayers

3.1 Importance of the subject

Nanoscale metallic multilayers have attracted strong interest for a considerable period of time. This interest continues to this day with a steady stream of original papers describing both experiments and computer simulations, with the occasional theoretical paper. The original motivation was to explore the well-known strengthening effects of decreasing the grain size, commonly known as the Hall-Petch effect, and, for example, ascertain whether there was any limit to strength. Other models of the strength such as confined layer slip have been actively considered [2, 43, 44, 45, 46, 47, 48, 49]. The implicit hope was that the toughness would increase along with strength but it quickly became apparent that ductility in nanostructured materials is generally rather small. Allied with this academic interest came a strong interest in severe plastic deformation as a technologically-oriented means of refining microstructure. An important subset of this area has been the development of multilayer, nanolaminate metals, which are typically made by either electrodeposition, physical vapor deposition or severe plastic

deformation. In the latter case, this is accomplished either via wire drawing or, more recently, via accumulated roll bonding [10, 15, 25, 27, 50]. The first two techniques have been extensively used to make nanotwinned metals, most notably copper and silver. Heterophase and homophase multilayers have been treated as separate problems, despite the similarity in microstructures. This chapter explores similarities and differences between the two types of multilayers with respect to models of strength.

3.2 Introduction

Nanostructured materials can be categorized into i) heterophase multilayers such as Cu-Nb with alternating layers of two or more different materials and ii) homophase materials such as nanotwinned Ag or Cu. As with any class of materials, strength in nanoscale metallic multilayers is governed by the ability of its interfaces to obstruct dislocation motion. These materials exhibit strength that is substantially higher than in bulk nanometer layer thicknesses [19]. Despite extensive research into strengthening (both in terms of experimental measurements and computer simulations), it is not clear which mechanisms of strengthening apply at the nanoscale regime. In this study, we focus on metallic systems, since this class of materials provides ample data, and compare two of the more popular and competing theories for size effects, namely CLS and H-P [51, 52]. As a way of unifying the understanding of strength in multilayers, it is argued that treating dislocations stored in interfaces as an obstacle forest provides a new approach with a Hall-Petch-like layer dependence that can rationalize many observations and offers a testable hypothesis for ongoing experimental investigations.

3.3 Strength model at different nanoscale layer thicknessess

The strength of a nanolaminate depends on the type of interface and on its layer thickness. In a coherent interface, since the slip plane and direction are continuous across the interface, it is easier for dislocation transmission to occur [9]. This leads to a smaller resolved shear stress and thus a softer material. In an incoherent interface, due to discontinuous slip plane and direction at the interface, it is much harder for dislocation transmission to occur. Thus, high resolved shear stress is required to slip in this or in semi-coherent interfaces making the material harder. Besides the type of interface, strength of a metallic nanolaminates is highly dependent on the layer thickness of the interface.

Layer thickness dependent strength models can be divided into three major phenomena as shown in Figure 3.1.

Hall-Petch model

At interlayer thicknesses of over 100 nm, the strengthening mechanisms follow the classical Hall-Petch model. Embury et al. first pointed out that Hall-Petch strengthening in single-phase metals is also applicable to two-phase bilayer materials [46]. In this mechanism, dislocations pile up against the interface, resisting the generation or movement of dislocations. The smaller the laminates, the larger the density of interfaces that hinder the dislocation movement leading to an increase in yield strength and making the material stronger. Therefore, the yield strength is inversely proportional to the layer

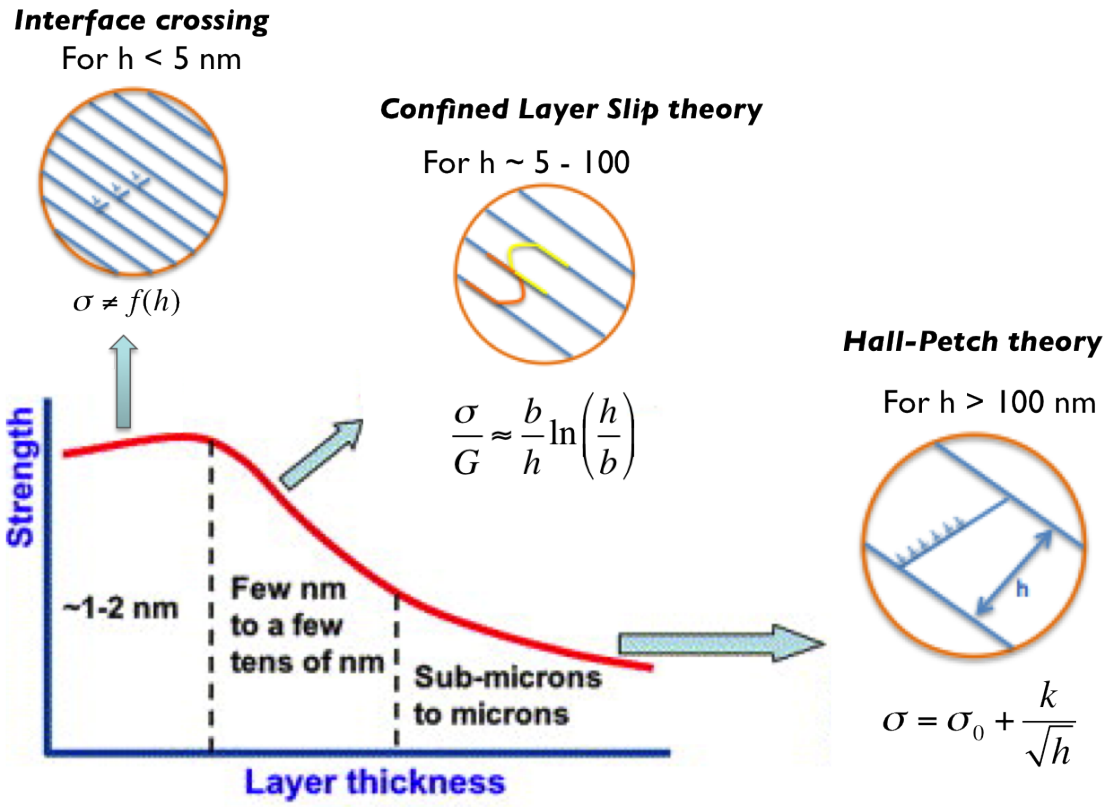

Figure 3.1: layer thickness dependent strengthening mechanisms in metallic nanolayer [49].

thickness (h) by the following relationship:

$$\sigma_{\mathrm{y}} = \sigma_{\mathrm{o}} + \frac{k}{\sqrt{h}} \tag{3.1}$$

where σ_{o} and k are Hall-Petch constants.

Dislocations piling up against the interface lead to a non-uniform distribution of slip resulting in uneven changes in thickness. This behavior is shown in Figure 3.1 for the coarsest scale.

Confined Layer Slip model

The Hall-Petch model has proven to accurately predict strength in terms of dislocation

pile-up. However, below a certain layer thickness i.e. ten to a few tens of nanometers, "the dislocation source to obstacle distance is small enough to prevent dislocations from piling up on a glide plane against an obstacle" [53]. Instead of forming dislocation pile-ups and storage, as required in standard work hardening theory, individual dislocations are forced to bow out within their layer of origin. Slip within the layer is governed by glide of individual dislocations inside each layer and the dislocations move at the Orowan bowing stress. This model is referred to as confined layer slip. CLS is one of the most discussed theories behind strength in nanostructured materials.

As the confined layer slip exceeds the interface barrier to slip transmission, it results in strain localization at the interface limiting the uniform deformability, as shown in Figure 3.1. The strength of the multilayer at this thickness is determined by:

- Critical stress (τ^*) needed to push the glide dislocation along the interface.
- The stress (τ_{Orowan}) required to propagate the single dislocation loop [53].

According to the CLS model, with only one dislocation looping in the layer, the strength of the nanolayers continues to increase with decreasing h. As shown in Figure 3.1, strength gradually increases until about 10 nm, after which it saturates. This lower limit of 10 nm layer thickness can, in principle, vary from 5 to 10 nm based on the experiments and literature reviewed.

Interface crossing model

When the value for h reaches less than 10-5 nm, confined layer slip stress exceeds the barrier to slip transmission, resulting in the transmission from confined layer slip to interface cutting by single dislocation [1]. This cut plane at the interface results in a shear offset as shown in Figure 3.1 and Figure 3.2. Anderson et al. reported that from

10 nm to about 4 nm, mismatched dislocations seemed to disappear which could be why softening is observed. At this length scale, layer thickness becomes smaller than the dislocation size [54]. This accompanying loss of strength is also sometimes referred as the inverse Hall-Petch behavior.

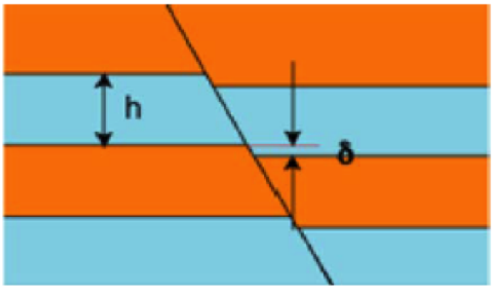

Figure 3.2: Schematics of shear offset at the interface [1].

3.4 Comparison with nanotwin materials

Nanotwinned materials in comparison to nano-crystalline materials have high strength and improved ductility. They also exhibit high electrical and thermal conductivity. The strengthening mechanisms of nanotwinned materials follow similar trends to that of nanocrystalline materials. Below a certain twin thickness, strength starts decreasing and the material starts softening. Zhu et al., from their experimental and simulation results, reported that this critical twin thickness is 15 nm [55]. However, other researchers such as You et al. have shown that the strength increases all the way down to few nm and there is no turn-over at ∼15 nm [56]. This behavior was reported on electro-polished nanotwinned Cu. Typical microstructures of nanotwinned Ag film are shown in Figure 3.3.

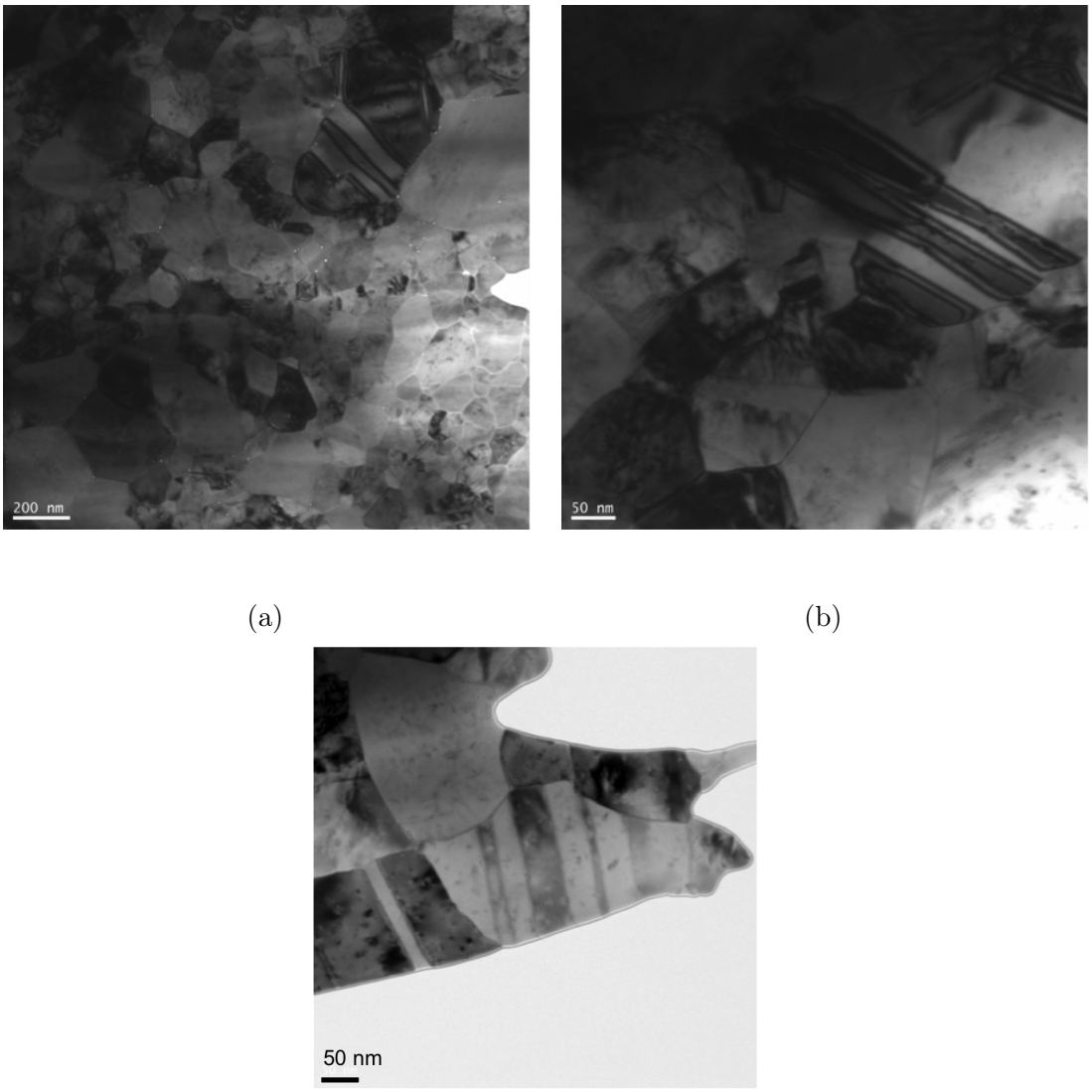

Figure 3.3: TEM images of nanotwinned silver film.

3.5 CLS history/problem formulation

Confined layer slip theory is one of the most discussed and widely applied theories to model strength in nanostructured materials. The concept of CLS originated in 1988 with Nix's analysis of the strength of a thin metallic films [44], although in this particular paper, a misfit dislocation model was used to account for the variation in strength,

which was itself based on an analysis by Freund [43]. Shown below in Eq. 3.2 is Eq. 36 from Nix's 1989 paper, which shows the same dependence of strength on $h^{-1}\ln(h)$ as in the CLS approach.

$$\sigma = \frac{sin\phi}{cos\phi\ cos\lambda} \cdot \frac{b}{2\pi(1-\upsilon)h}\left[\frac{\mu_f\mu_s}{(\mu_f+\mu_s)}\ln\left(\frac{\beta_s h}{b}\right) + \frac{\mu_f\mu_o}{\mu_f+\mu_o}\ln\left(\frac{\beta_o t}{b}\right)\right] \tag{3.2}$$

where, ϕ is the angle between the slip plane normal and applied force (refer to Fig. 4.39), λ is the angle between applied force and slip direction, sin ϕ/cosϕ cosλ was 3.464, μ_{f}, μ_{s} and μ_{o} are the shear moduli of film, substrate and oxide respectively. h and t are film and oxide thickness. ν and b are Poisson's ratio and Burgers vectors respectively. $\beta_{\mathrm{o}} = 17.5$ and $\beta_{\mathrm{s}} = 2.6$ are numerical constants.

It is also notable, that fitting to experimental data from polycrystalline thin films, aluminum in particular, needed a Hall-Petch term to be added because of a grain size that also scaled with the film thickness.

The CLS approach was developed over the years [45, 46, 47] and was later applied by Misra in 1999 to Cu-Ni and Cu-Cr nanolaminates [48]. Equation 3.3, was introduced by Misra in 1999 and relates the flow strength (σ) to the layer thickness (h), shear modulus (G=48 GPa), Poisson's ratio (ν=0.3) and Burgers vector (b=0.25). Equation 3.3 is referred to as the regular CLS in this thesis

$$\sigma = \frac{Gb(1+\upsilon)}{\pi h(1-\upsilon)}\ln\left(\frac{\sqrt{2}h}{b}\right) \tag{3.3}$$

A more widely used form of the equation (after omitting constants such as ν and π) is

$$\frac{\sigma}{G} \approx \frac{b}{h} \ln\left(\frac{h}{b}\right). \tag{3.4}$$

Here, stress is normalized by the shear modulus and thickness h is normalized by the Burgers vector. It should be noted that in the literature, stress has also been normalized with an average hardness of Cu and Nb using the rule-of-mixtures but in this study, stress is normalized with G as the original equation itself contained the shear modulus. Note that Eq. 3.4 is referred to as simplified CLS in this thesis.

However, as Fig. 4 in Misra et al. [49] showed, the observed layer thickness dependence of the flow stress for Cu-Nb is weaker than predicted by equation 3.4. They found that the CLS approach was insufficient and therefore two additional terms were added, as shown in Eq. 3.5 to refine the model. One of these was a fixed contribution from dislocations in the interface and one was an elastic back-stress correction, which was only significant at a very small thicknesses. The contribution from interface dislocations was, however, substantial.

$$\sigma = M \frac{\mu b}{8\pi h} \left(\frac{4-v}{1-v}\right) \left[\ln \frac{\alpha h}{b}\right] - \frac{f}{h} + \frac{c}{\lambda} \tag{3.5}$$

where c= μ b/ (1-ν)

Furthermore, Misra et al. in the same year [57] posited that the small degree of work hardening observed in Cu-Nb composites could be ascribed to the accumulation of dislocations in the interfaces. Nyilas et al. [58] analyzed line peak shapes for Cu-Nb and concluded that there is a significant dislocation content that was assumed to be

confined to the interfaces. All of this points to a need for a theory that can accurately predict the strength behavior in nanolaminates.

3.6 Hypothesis

It is hypothesized that modified H-P provides a better fit than CLS theory for nanolaminates down to about 10 nm. This will be verified by fitting different strength theories and material information to predict material behavior at this length scale.

3.7 Hall-Petch approach

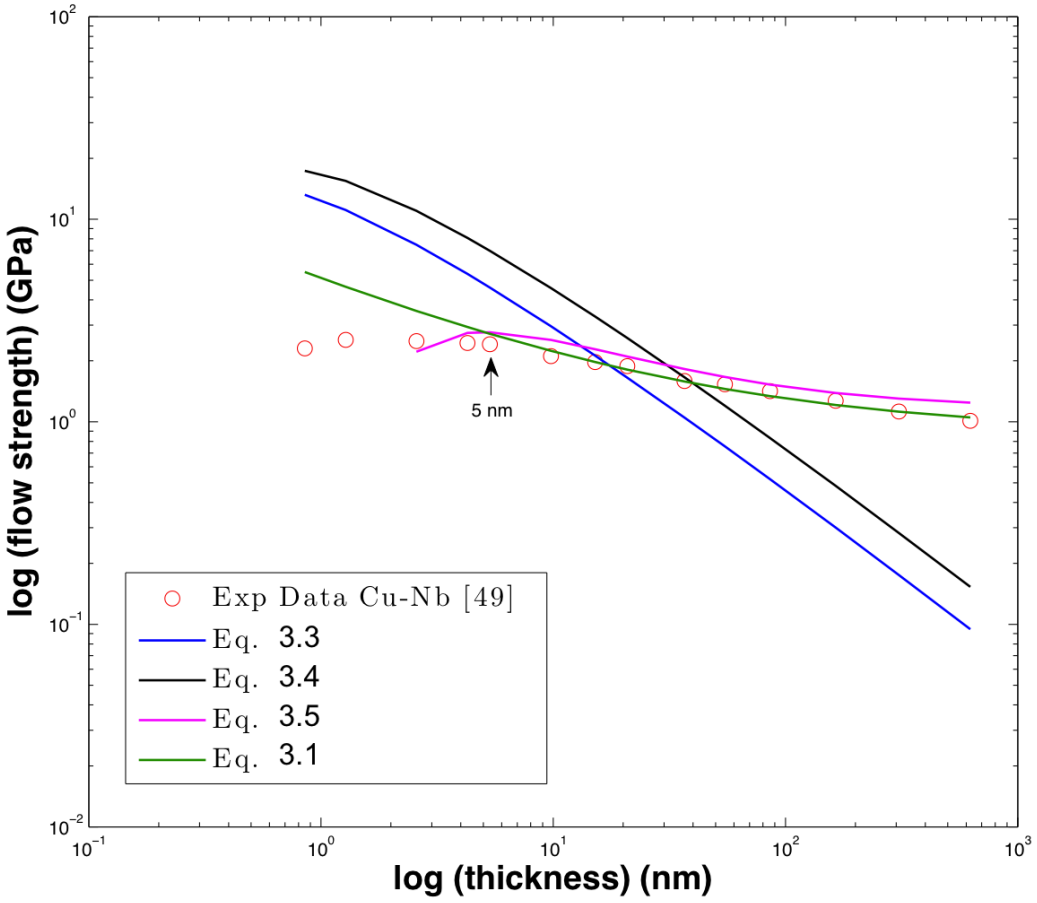

Figure 3.4: Experimental values compared with modified H-P and different versions of the CLS theory [48, 49] for layer thicknesses of 5.33 to 625 nm. The curves for Eqs. 3.3, 3.4, 3.5, 3.1 correspond to regular CLS [48], simplified CLS, modified CLS [49] and the fitted Hall-Petch equations.

As shown in Figure 3.4 and 3.5, the CLS equation with no other terms added intersects the experimental values around 30 nm such that it underpredicts at large h and overpredicts at small h. Different choices of constants in the CLS theory shift the stress levels up or down, but do not change the basic thickness dependence. With the addition of the

	σ_o (GPa)	k (GPa $nm^{1/2}$)
Nanocrystalline (nc) copper [59]	0.097	3.27
nc-copper [60]	0.02	4.43
Cu-Nb (this work, [49])	0.88	4.25
nc-Ag [61]	0.12	1.4
nc-Ag [62]	0.09	1.15

Table 3.1: Hall-Petch coefficients (σ_o, k) comparison for different materials.

two constant terms that Misra formulated, the approaches gets close to the experimental value but is not in perfect agreement with experimental values. Note that there is a slight discrepancy observed between the experimental points and the modified CLS model, although the parameter values used for the modified CLS, as shown in Equation 3 in Figure 1, were extracted from Misra et al. [49].

However, we find that Hall-Petch equation, with coefficients (σ_o, k) only slightly different from those previously reported for nanocrystalline copper [59, 60], provides a much better fit for heterogeneous nanolaminates down to layer thicknesses of about 5 nm. As shown in Figs. 3.4 and 3.5, below 5 nm the experimental data start to deviate. Hall-Petch coefficients were chosen so as to minimize the root mean square (RMS) error between the analytical results and the experimental data. A comparison between H-P coefficient values for regular nanocrystalline (nc) copper and Cu-Nb nanolaminates and different nc-Ag data sets is shown in Table 3.1 [59, 60, 61, 62]. For the heterogeneous nanolaminates considered here, the elastic properties of copper were used in the CLS equations because it is the softer or more compliant material. Therefore, we conclude that it is possible to match the experimental data with the H-P approach but not CLS (except when significantly modified [49]).

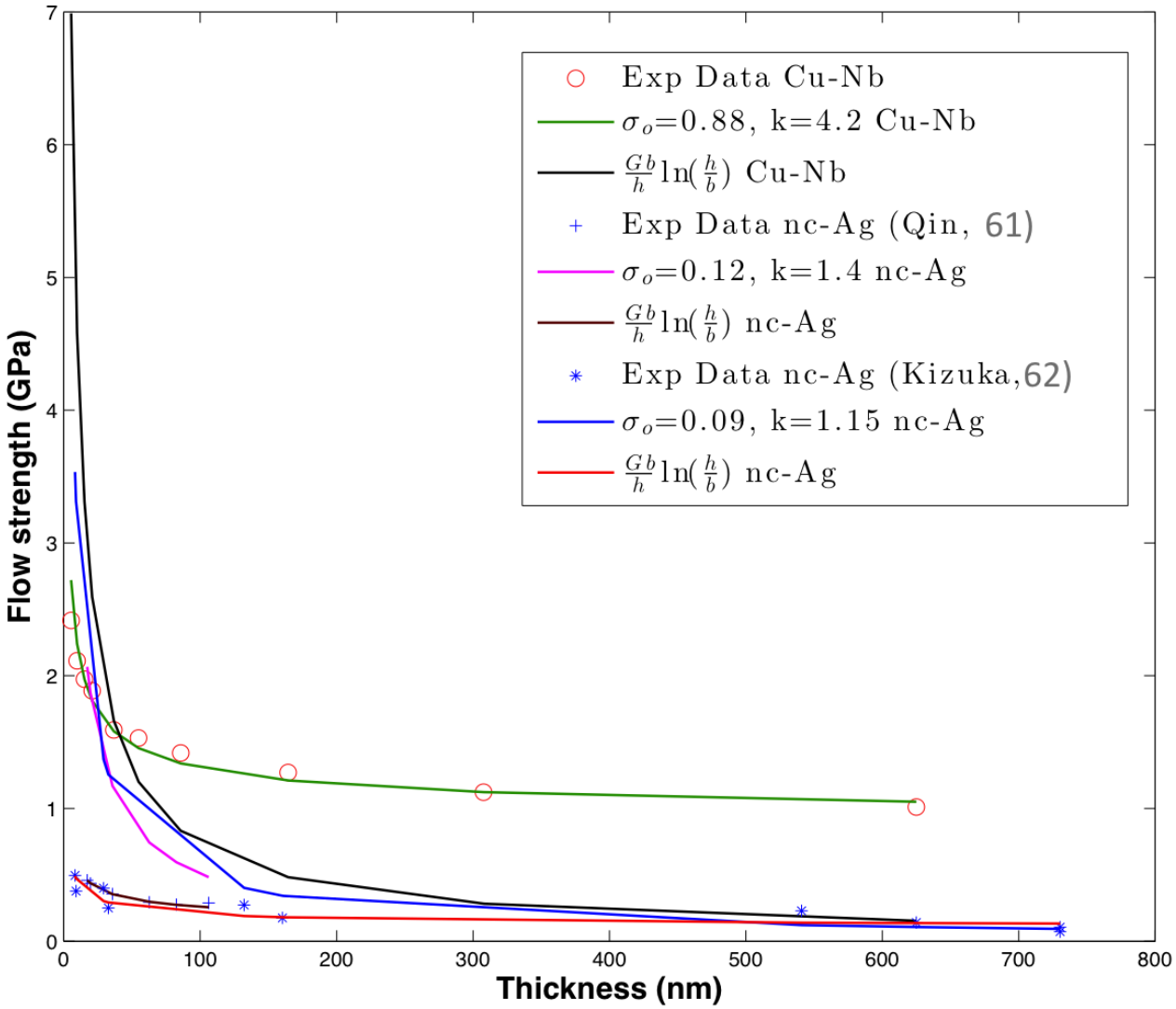

Figure 3.5: Cu-Nb and nc-Ag flow strength comparison with different theories.

The strength of nc Ag follows a similar trend but at substantially lower strength values, as shown in Fig. 3.5. Although one representative homophase case has been selected for clarity in plotting, nanocrystalline copper shows similar strengths to the nanocrystalline Ag after normalizing by the shear modulus. Likewise, many other heterophase composites exhibits comparable behavior to that of the Cu-Nb, as shown in

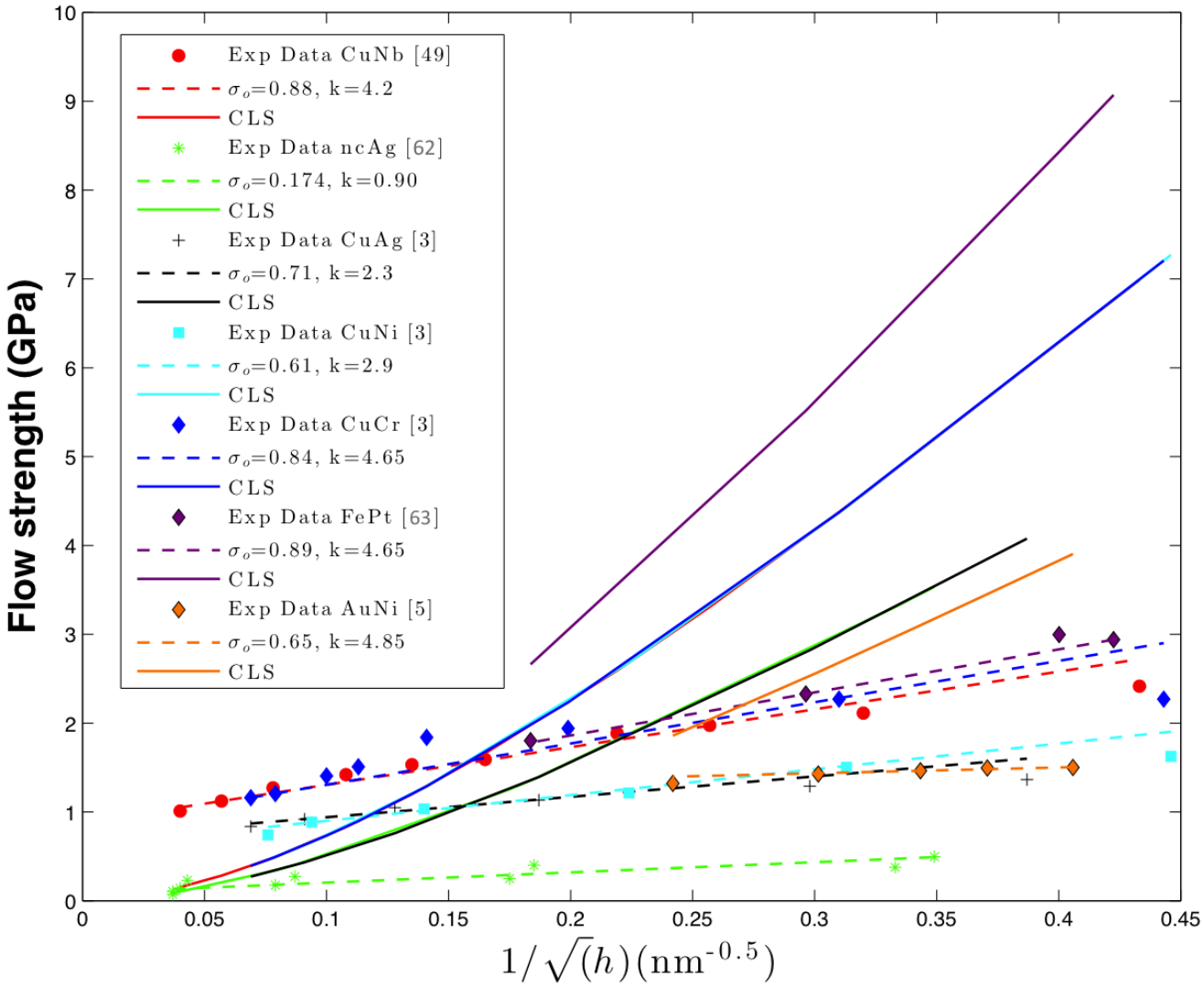

Figure 3.6: Modified H-P and CLS theory comparison for other nanocomposites. H-P coefficients for each nanocomposite were chosen so as to minimize the RMS error between analytical and experimental data. Same color in the graph represents same material.

Fig. 3.6. Heterophase composite data is extracted from Misra et al., Arzt 1998, and Schweitz et al. papers. [3, 5, 63] Overall, it appears that the H-P relationship with modified coefficients fit the data better than the CLS.

3.8 Dislocations in interfaces

As noted above, Misra et al. [49] considered strength models, they also found that the CLS approach was insufficient and two additional terms were required. One pertained to a fixed contribution from the dislocations lying in the interface and another corrected for the elastic backstress, which was only significant at very small thicknesses. The former contribution may at first be attributed to the intrinsic misfit dislocation density that exists in heterophase nanolaminates to accommodate the lattice misfit [64]. However the strengthening effects from the interface dislocations were substantial for layer thicknesses below about 20 nm. Furthermore, Misra et al. in the same year [57] posited that the small degree of work hardening observed in Cu-Nb composites could be attributed to the accumulation of extrinsic dislocations within the interfaces. In support, Nyilas et al. analyzed diffraction patterns and the shape of the diffraction peaks for Cu-Nb and concluded that the significant dislocation content detected was confined to the interfaces [58]. Molecular dynamics (MD) studies have demonstrated that interfaces, which may initially contain a misfit network, have the ability to nucleate, store, and recover dislocations [65, 66, 67], which thereafter renders them significantly altered from their initially pristine form. All these considerations point to the accumulation of extrinsic dislocation content within the interfaces when the nanolayered composites are strained.

The storage of dislocations in the interface can contribute to nanolayer composite strengthening. This basic notion has been discussed in the context of grain boundaries. In Hirth's review article [68] on the influence of grain boundaries in mechanical properties, he noted that grain boundaries act as sinks, sources, barriers, and storage sites for lattice dislocations. In particular, lattice dislocations are likely to decrease their net

energy in the grain boundaries by spreading out or redistributing into a combination of smaller Burgers vectors. This lower energy state effectively traps the dislocation in the boundary by introducing an energy barrier to re-emission. More recently Blum & Zeng [69, 70] developed a strength model for nanocrystalline metals (grain sizes below 1 μm) based on forest hardening in the grain boundaries rather than in the grain interiors. In their model, hardening was controlled by thermally activated storage and recovery in the grain boundaries. They postulated that for grain sizes below about 1 μm, tangling and storage of dislocations within the grains is not feasible. The storage rate of dislocations in the boundaries was straightforwardly related to the mean free path, just as in conventional work hardening theories. The recovery rate was assumed to be limited by a climb-mediated annihilation of edge dipoles deposited in the boundaries. A similar phenomenon has been considered in nanotwinned materials, such as Cu and Ag. MD simulations have shown that dislocations tend to nucleate where grain boundaries and twin boundaries meet and interactions of dislocations and twin boundaries can leave the twin boundary with some amount of dislocation storage [71, 72]. Based on this insight, a recent crystal plasticity model demonstrated that the very fine twin thicknesses can limit dislocation nucleation and motion, creating larger obstacles to plasticity as the twin thickness reduces [73].

Here, we consider a strengthening model based on the stored dislocation density in the interface. The interfacial dislocation density ρ_{int} evolves much like a crystalline dislocation density for a bulk material, with the exception that most of the density accumulates in the interface and not within the nanolayers. The time evolution of the interface density is determined by a balance of the rate of dislocation formation, trapping, and recovery in the interface. The recovery mechanisms are conceptually understood by considering that confinement in a plane means that dislocations of opposite sign (but

same Burgers vector) cannot avoid meeting and annihilation provided that they are spaced less than a critical distance.

Eventually, after some amount of straining, the interface density reaches a saturation value ρ_{int}. Hardness testing typically requires an appreciable amount of strain in the vicinity of the indent that can often exceed 10% [74], which would be sufficient to reasonably expect a saturated state. More so, the small amount of work hardening observed in bimetal nanolaminates, e.g., Cu-Nb, and nanotwinned metals, e.g., Cu, hints at a situation where extrinsic interface dislocations has rapidly reached a saturation density. The saturation value would depend on temperature, strain rate and interface character, but would otherwise, within the nanoscale regime ($h < 100\,nm$), be insensitive to the layer thickness h. To proceed, we consider that each interface holds a fixed density of dislocations, ρ_{int}, here measured as line length per unit area. The total dislocation density in the material is the interface density divided by the layer thickness, $\rho_{\text{total}} = \rho_{\text{int}}/h$. Applying the Taylor hardening equation, the strength of a nano layered material as a function of h is obtained:

$$\tau = \alpha G b \sqrt{\frac{\rho_{\text{int}}}{h}} \tag{3.6}$$

Equation 3.6 leads to the main result; if one assumes a saturated dislocation density that has accumulated in each interface independent of the layer thickness h, then the strength of the nanolayered composite varies as $h^{-1/2}$.

Equation 3.6 can be used to explain the difference in strength between the nanotwinned materials and the heterophase nanolaminates. Compared to the twin boundaries in nanotwinned metals, the bimetal interfaces characteristically contain appreciable

dislocation content after deformation. For example, an increment in hardness of 6 GPa translates to a dislocation density in the interfaces of about 10^7 m^{-1}, which is equivalent to an interface dislocation spacing of about 50 nm. For layer thicknesses h much below this spacing, it is interesting to speculate on whether the stress fields of extrinsic interface dislocations interact strongly enough to result in dipole alignment across layers.

Toward some insight on this last thought, we turn our attention to the model published by Blum & Zeng [69, 70] in which they postulated that the deformation kinetics in nanocrystalline metals could be controlled by storage and recovery in the grain boundaries. They fitted their model to experimental data for nanocrystalline Cu and Ni. The most interesting parameter in their model is the separation distance between dipole elements, below which spontaneous recombination occurs. This critical distance was determined to be 5 and 15 times the Burgers vector magnitude for Cu and Ni, respectively, which is a large multiple but not unreasonable [75]. The final equation that they obtained shows that the stress depends on the square root of the grain size and that the strain rate varies as the eighth power of the stress.

3.9 In-situ TEM compression and tensile test

As shown in the modeling work earlier in Figure 3.4, 3.5 and 3.6, modified H-P provides a better fit for nanocyrstalline and nano-laminates experimental data than the CLS theory. However, there was no experimental evidence to back up this theory. Therefore, an in-situ TEM test was carried out to image dislocations and to see whether they accumulate and migrate towards Cu-Nb interface as posited in the theoretical analysis. For this, both in-situ tensile and compression tests were carried out to observe the dislocation movement during straining.

In-situ TEM compression and tensile test were carried out by Dr. Lakshmi Narayan Ramasubramanian at Xi'an Jiaotong University in China.

The set up for in-situ tensile and compression test are shown in Figure 3.7 a and b. For the in-situ tensile experiment, the force is applied from the top in section 1 in the image in Figure 3.7 a) hitting the two blocks on each side. It then stretches them to create a tensile stress in the sample. This is the first time a Cu-Nb nanolaminate specimen has been pulled with a tensile force with an in-situ system in a TEM. Before this study, the majority of in-situ Cu-Nb studies were conducted doing compression tests [76]. Due to the nature of the experimental setup, tensile samples were more clean, with less vibration and gave better results. As shown in Figure 3.7a), the force transmits through section 1, 2 and 3 before it reaches the gage section. Therefore, the sample goes through 3 steps of damping, resulting in less vibration. Whereas in compression test shown in Figure 3.7b), the force is applied directly to the sample resulting in a lot of noise associated with the compression samples making it difficult to observe dislocation motion. The sample preparation technique used for both, tensile and

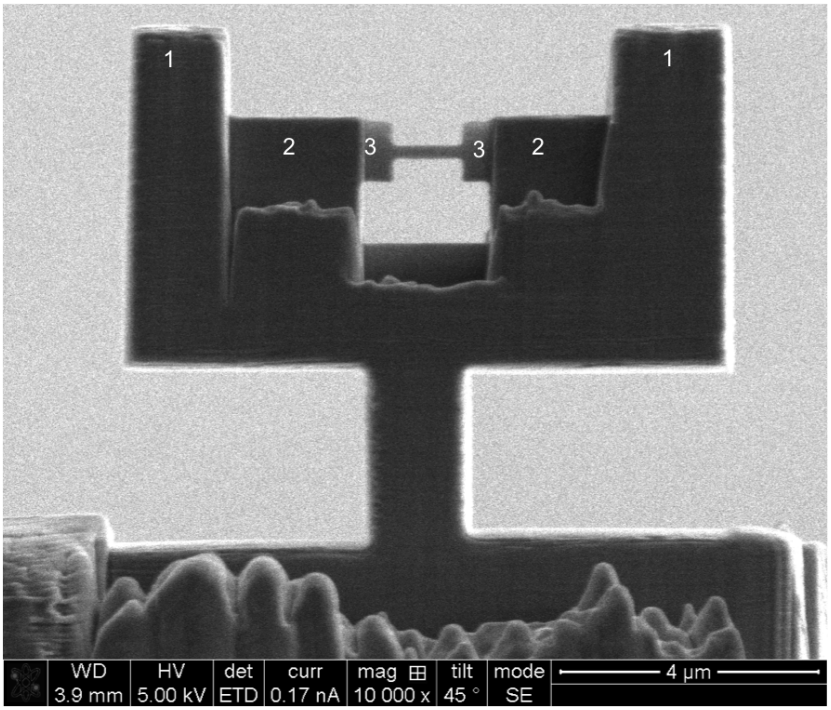

(a)

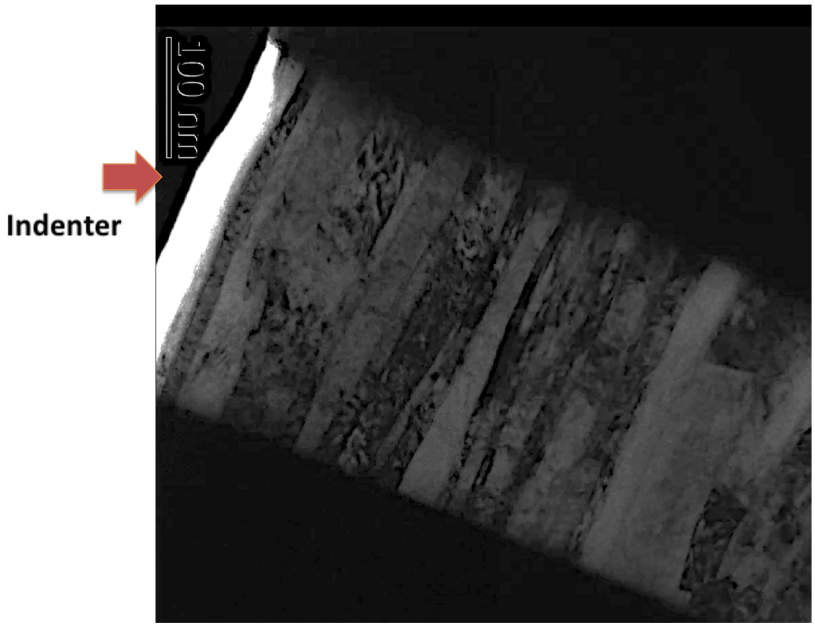

(b)

Figure 3.7: TEM images of a) tensile and b) compression test setup of Cu-Nb.

compression, samples was FIB lifting method, which is described in the earlier section. It is a very arduous process and only a few samples lead to a successful experiment which are presented in this thesis.

High resolution TEM (HR-TEM) work could not be done because that limits the field of view and number of layers that could be monitored. The aim was to look into the sample (or gage region) as a whole and analyze the dislocation movement. Therefore either bright field TEM or the scanning TEM (STEM) was done for 10 nm, 20 nm and 140 nm layer thickness samples.

As shown in Figure 3.8, different types of dislocation activity can be seen during tensile loading, as denoted by dislocations with different color arrows. The red arrows show dislocations that form a loop and glide within the interface from the beginning of the tensile loading till the end. The blue arrow shows a dislocation that appeared momentarily (in t=27s) and disappeared. Yellow arrows show two tangled dislocations that mostly stay in the same place throughout the deformation.

After careful observation of the dislocations with red arrows, we noticed that there were two sets of these types of dislocations that glided in the layer. They would come close (t=27s) and get further away (t=72s) at different frames. The one that is closer to the center of the gage section seems to have migrated towards the Cu-Nb interface as shown in the last two images i.e. t= 68 and 72s. This behavior was also evident in other videos. For example, the tensile test result in a different sample, as shown in Figure 3.9, showed similar behavior, where the dislocation is migrating towards the interface with the application of tensile stress.

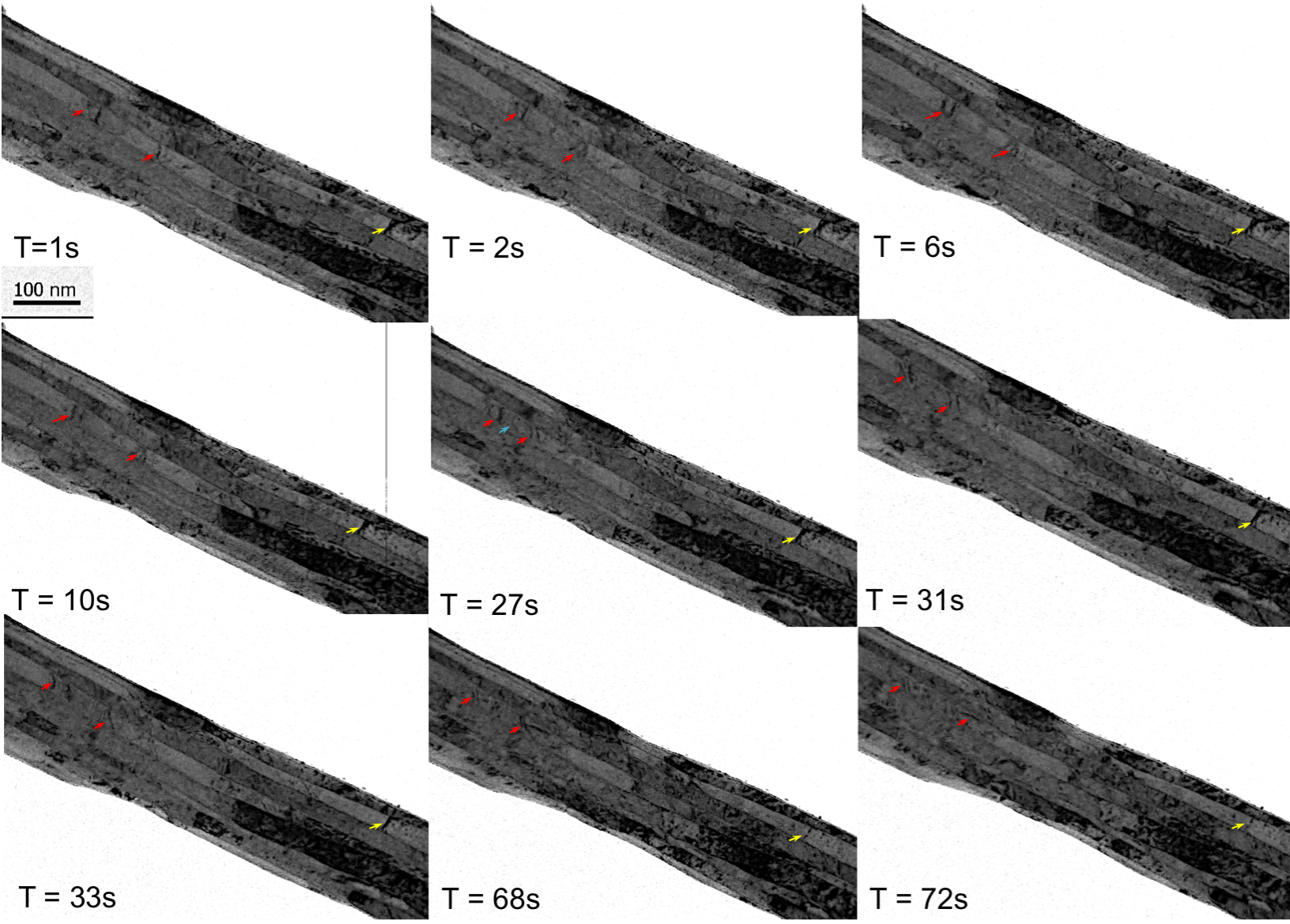

Figure 3.8: A sequence of bright field TEM images, at different time-step T, during in-situ tensile loading showing dislocation activities in a 20 nm sample.

In a different example, in in-situ compression loading, it is presented that, similar to tensile testing, the dislocations (shown by red arrows) are gliding in the layer during compression. After compression testing, the average layer thickness of the highlighted layer changed from 40 to 36 nm. It should also be noted that layers at which dislocations are observed in Figure 3.8, 3.9 and 3.10 are all Cu layers. Cu layers can generally be distinguished by the lighter color with fewer dislocations in them. Copper is also the

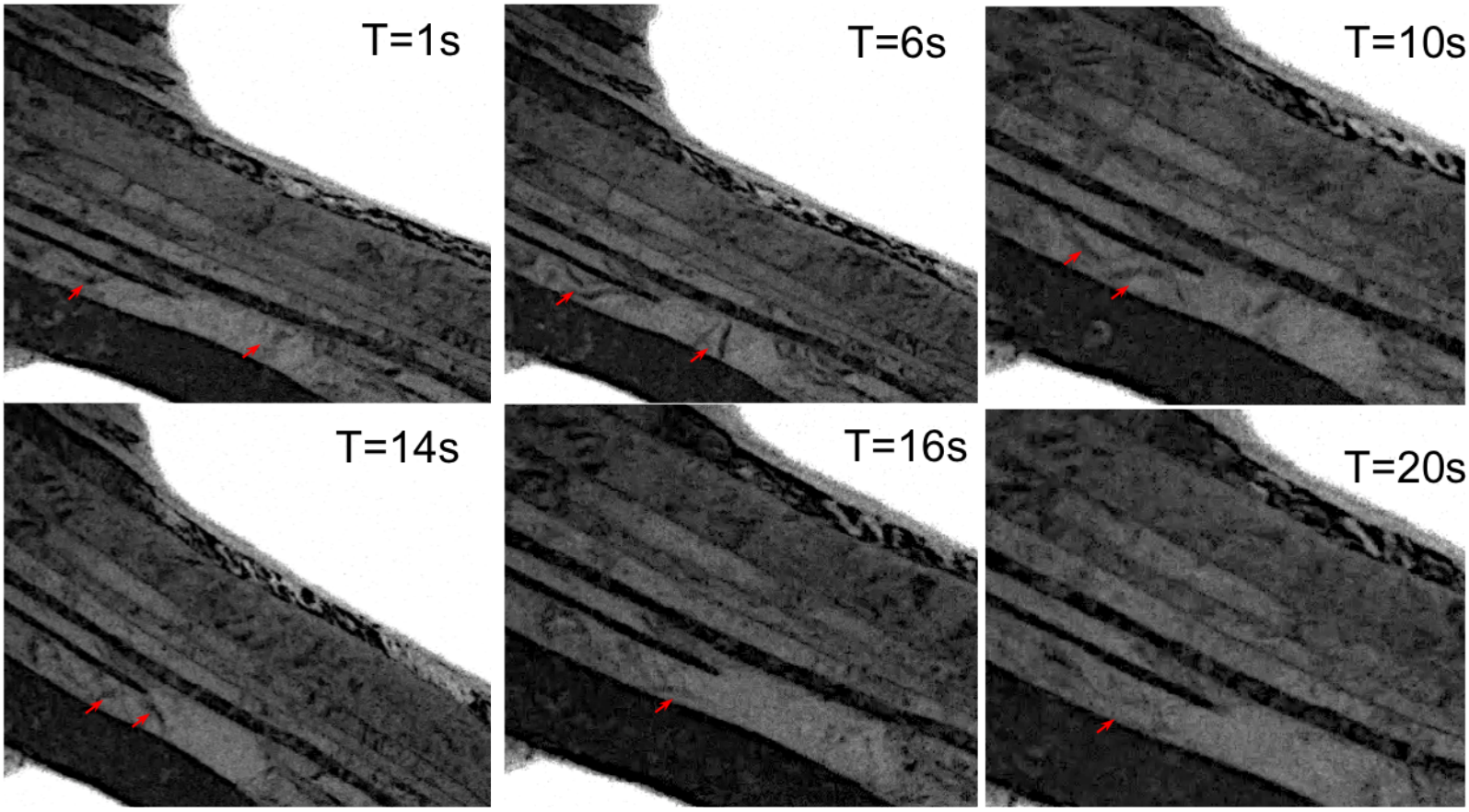

Figure 3.9: A sequence of bright field TEM images, at different time-step T, during in-situ tensile loading showing dislocation migrating at the interface in a 20 nm sample.

softer material of the two.

All this indicates that the strength behavior is controlled by the dislocations in the individual layer as well as in the interface. In this study, we observe both confined layer slip and dislocation storage in the interface. The future study of this work would, therefore, be to create a model that could capture both of these behaviors.

Some of the other observations that were made based on the in-situ videos are as follows:

- Dislocations seem to be both stored in and nucleated from the interface.

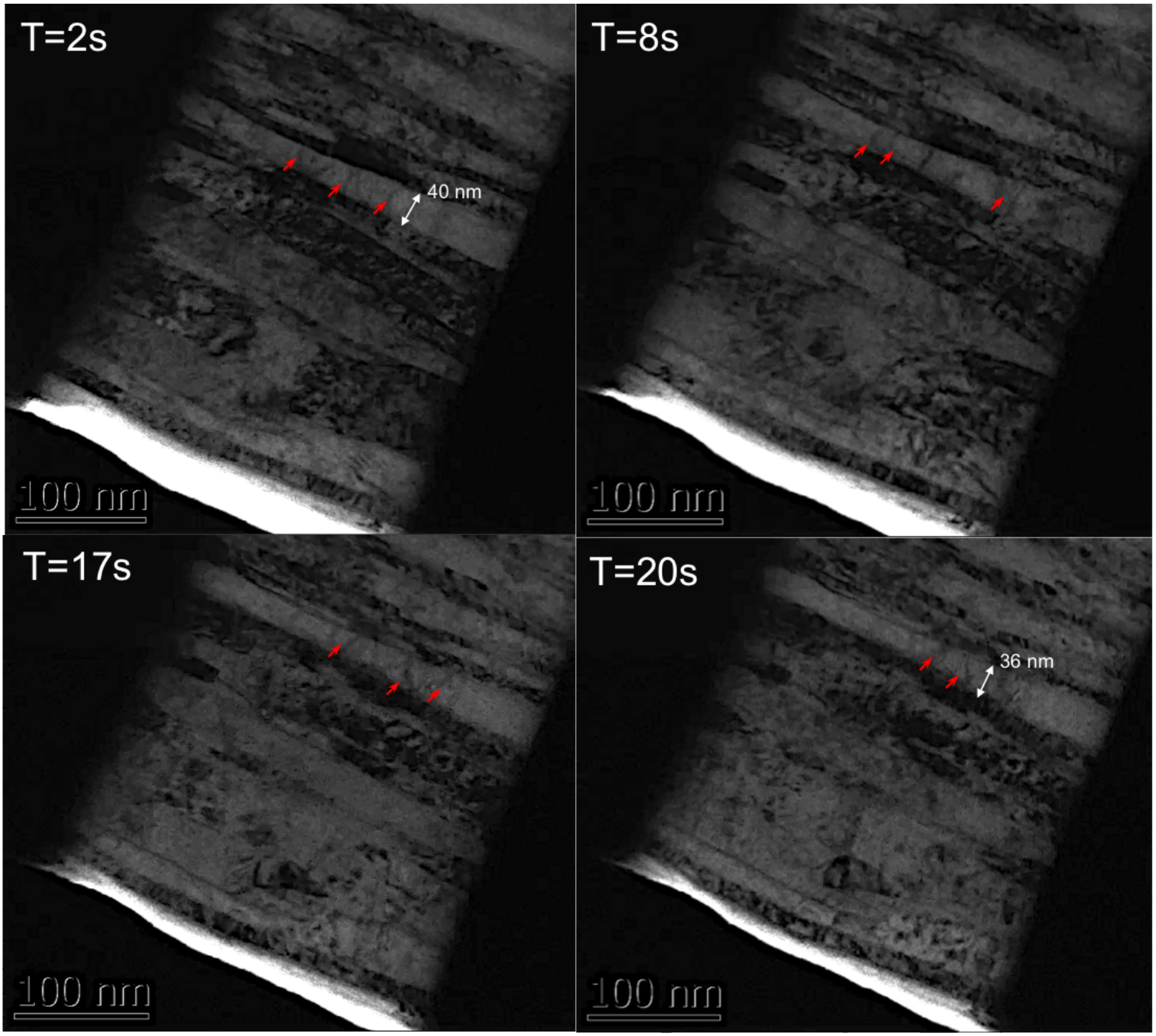

Figure 3.10: A sequence of bright field TEM images, at different time-step T, during in-situ compression showing dislocation migrating at the interface in a 20 nm sample and changes in layer thickness with strain.

- If there are dislocations with opposite Burgers vectors, often they could annihilate and cancel out.
- Slip transmission was observed several times. Dislocations seem to cross the interface.
- Dislocations move very slowly at the beginning at low strain. With an increase in strain, the dislocation density clearly increases and they start to move in all directions at a very high speed. They move in a fraction of a second, making it very hard to resolve their movement with the current camera.

As can be seen in the TEM images, the layer thicknesses of Cu and Nb are not always 50/50. Either of them could be coarser than the other one. There could be a situation where a very thin layer i.e. less than 5 nm is sitting next to a 5-50 nm layer. In this case, the 5 nm layer would be experiencing interface crossing behavior whereas the 5-50 nm would be confining the dislocations in the layer or in the interface. It would be very interesting to see what happens when a dislocation crosses the interface and gets to the thicker region. Would the dislocation remain in that layer or would it continue to move on? How would the strength behavior of the material change? These are some of the questions that need to be addressed in the future.

Similarly, in the future, the sample could be heated first to reduce the surface damage that might have been introduced during the sample preparation and to relieve stress. [77].

It is also important to note that the failures in all the tensile samples were due to the shear localization, as shown in Figure 3.11. Also, this is the same sample whose dislocation behavior was studied in Figure 3.8. As shown in t=72s, a slight notch in the

same can also be seen.

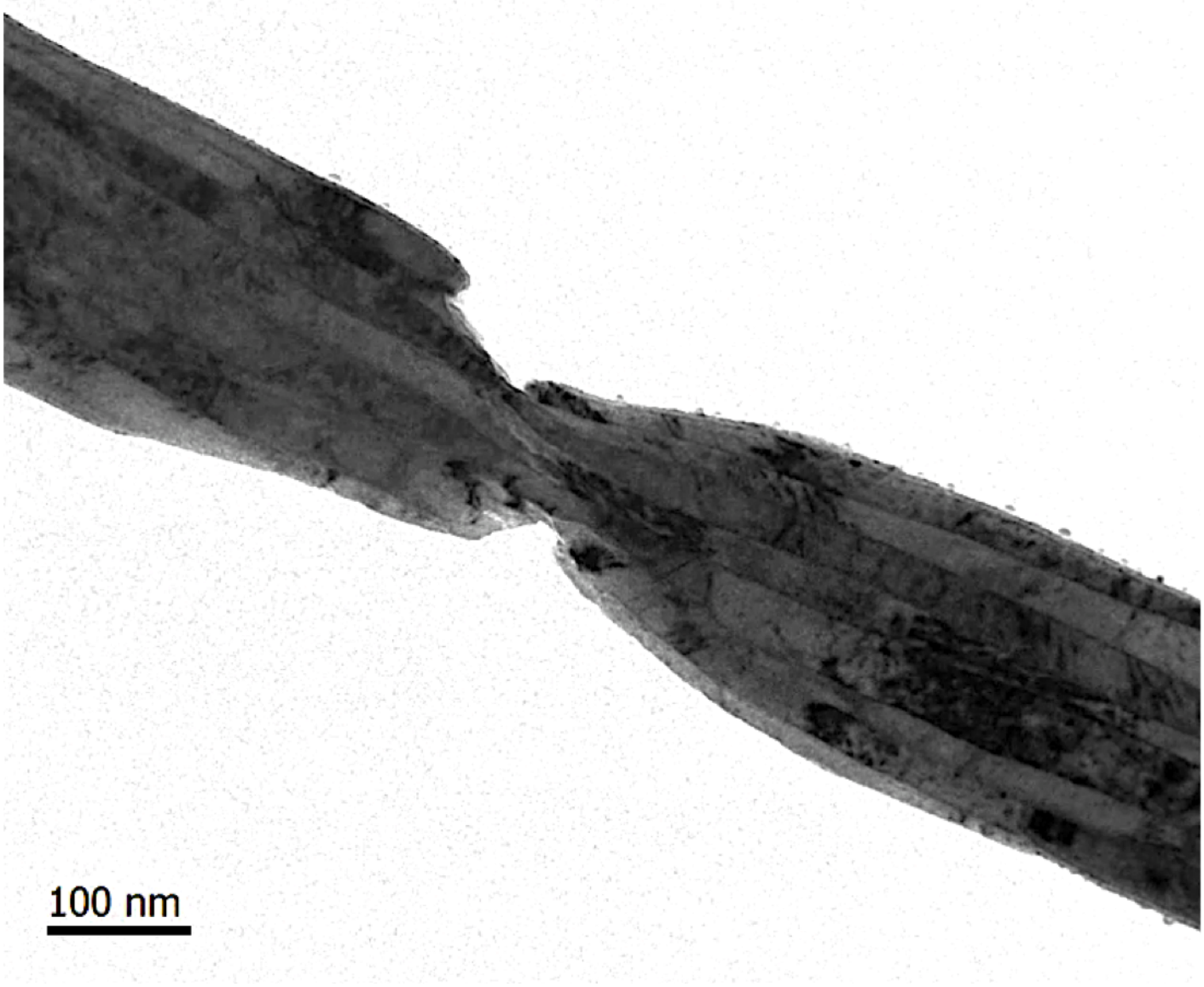

Figure 3.11: TEM image of a failed region showing a notch in 20 nm Cu-Nb.

3.10 Summary & Discussion

In this chapter, nanostructured material strength and the role of dislocations in modeling the strength behavior is discussed in detail. Both experimental and theoretical studies

were performed in this work. The layer thickness of interest was in the range of 5 - 100 nm, where neither the dislocation pileups against the interface nor the interface crossing behavior is expected. Instead, the popular theory is that 1 or 2 dislocation bow to form a loop and glide in the layer. This phenomenon controls the strength behavior. From the data fitting study, it was observed that the popular CLS theory either over- or under-predicted the flow stress behavior. Therefore, additional terms were added to refine the model and to fit the experimental data. It was found out that the modified Hall-Petch equation, with slightly modified coefficients, provided a better fit down to about 5 nm. In addition, it was proposed that the interfaces contain an appreciable dislocation density that controls the strength of the nano layered composite.

Experimental in-situ TEM studies of 20 nm Cu-Nb were performed to capture dislocation movement during tension and compression. It was observed that dislocations glided in the layer as well as moved in and out of the interface. The interface was found to act as a site of dislocation nucleation and storage. In summary, both the looping and interface dislocation phenomena were seen.

3.11 Future Work

It is recommended to focus on the interface and image the total number of dislocations, as both CLS and interface dislocation phenomena was observed for 20 nm layer thickness with TEM studies. A model that could capture both the dislocation phenomena (looping in the layer and storage in the interface) is advised.

To obtain a clean strain free Cu-Nb for TEM experimentation, it is recommended to heat the sample before performing tensile or compression testing. This could aid in imag-

ing dislocations clearly and help discern dislocations with image contours. As discussed in the earlier section, the condition where there is a coarser layer thickness next to the smaller layer thickness was of interest. Such an experiment is advised where interface crossing could be happening in smaller layer thickness but gliding and storage in the coarser layer. The combined effect of the two types of layers would be interesting in itself.

FIB sample preparation for 140 nm Cu-Nb sample did not go as expected. Therefore studying dislocation behavior in 140 nm is recommended. The results from 10 nm also need to be analyzed in more detail. TEM tensile videos for 10 nm, as they were performed in STEM mode, did not have enough contrast to image the dislocations.

Chapter 4

Design, fabrication and characterization of Inconel 718 heat exchanger

4.1 Introduction

4.1.1 Additive manufacturing

Additive manufacturing (AM), also referred to as 3D printing, is a layer-by-layer technique of "producing three-dimensional (3D) objects directly from a digital model" [78, 79]. Although the concept of 3D printing has been around for several decades, metal 3D printing started in 1982. AM is used in automotive, aerospace, electronics, medical device and other industries with a variety of materials such as thermoplastic, metals, composites, glass and even food. It also has become increasingly popular in the 3D printing of complex biological structures using biomaterials [80]. AM is a very effective technique that can produce complex, lighter weight parts at a cheaper price and with a shorter lead time. This technique has a potential to revolutionize the manufacturing

industry and save billions of dollars. General Electric (GE), one of the world's largest suppliers of jet engines and a lead players in metal AM, is using 3D printed nozzles that are "25 % lighter and as much as 5 times durable than the existing model, which is welded from 20 different parts". GE also reports that it "may additively manufacture up to half of the parts in its energy turbines and aircraft engines in 10 years". Similarly, Boeing has "has additively manufactured more than 200 different parts for 10 aircraft platforms. Boeing has also used roughly 20,000 additively manufactured parts in military and commercial aircraft, including 32 different components for its 787 Dreamliner planes" [80].

In this work, AM technique is adopted to design, fabricate and characterize microchannel heat exchangers. It is a collaborative work with Prof. Vinod Narayanan and Dr. Erfan Rasouli from University of California, Davis.

4.1.2 Heat exchanger (HX)

AM is used to design and fabricate complex, microchannel heat exchanger (μHTPHX) for fossil fired supercritical CO_2 (sCO_2) using Inconel 718 superalloy. As shown in Figure 4.1, hot combustion gasses at relatively low pressure (1-10 bar) transfer heat to sCO_2 at around 300 bar in this μHTPHX, thereby resulting in large pressure differentials within the heat exchanger. This stringent requirement of high temperature and pressure differential necessitates the use of a superalloy. Inconel 718 (IN 718) superalloy is used for its mechanical and structural stability at high temperature range i.e. from -2^o to 1300^o F [81].

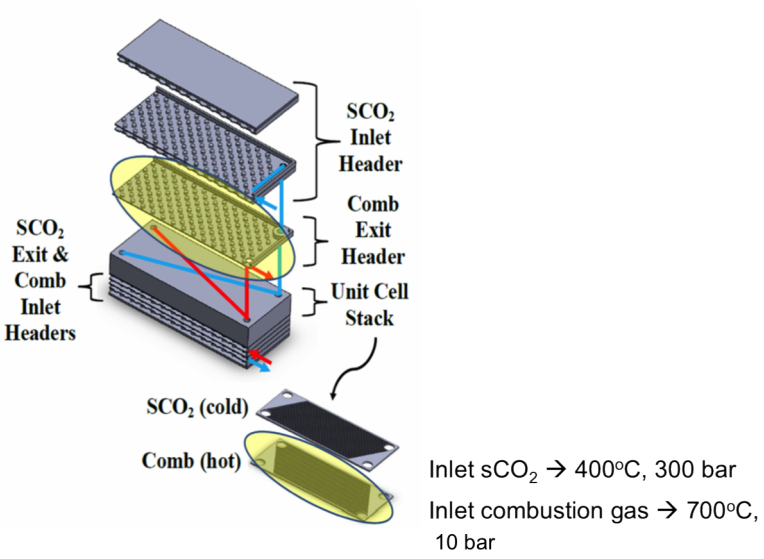

Figure 4.1: Exploded view of traditional HTHPX design with same number of fins on both hot and cold fluid side. Operating conditions at hot and cold sides are also shown.

4.2 Inconel 718 superalloy

IN 718 is a nickel-chromium based superalloy with 50-55 % nickel, 17-21 % chromium, 4.57-5.5 % niobium, 2.80-3.30 % molybdenum and remaining percentage of other components such as titanium, aluminum, cobalt, carbon, manganese, silicon, phosphorus, sulfur, boron and copper. It is a high-strength (tensile strength exceeding 1.4 GPa), corrosion and oxidation resistant, superalloy that can operate at temperatures of -423° F to 1300° F. The term "Superalloys" refers to a high performance alloy that exhibits properties such as excellent mechanical strength, resistance to creep deformation and rupture, good surface stability, and resistance to corrosion [81, 82]. IN 718 is also referred to as an age hardening or precipitate hardening alloy which means that if the metal is heat treated properly Ti, Al and Nb form strengthening precipitates with Ni. Three of the main intermetallic precipitates that form in IN 718 are:

i γ' having a composition Ni_3Al, Ni_3Ti and $Ni_3(Ti, Al)$ and a body-centered tetragonal (BCT) structure

ii γ" having a composition Ni_3Nb and a FCC structure, and

iii δ with same composition Ni_3Nb but orthorhombic crystal structure.

These precipitates act as an obstacle and hinder the movement of dislocations resulting in high strength. They also form a coherent interface with the austenitic (γ) matrix which does not let the precipitate coarsen. This formation of coherent γ' precipitate and the discrete carbides at the grain boundary inhibits or obstructs the movement (sliding) of dislocations (or damage accumulation) during high-temperature creep [83].

Besides precipitates, Laves phase forms which is a brittle intermetallic phase that is hexagonally close packed and has a $MgZn_2$ lattice. It is a Nb rich phase represented as $(Ni,Fe,Cr)_2(Nb,Mo,Ti)$. Due to its brittle nature, Laves phase particles act as a site of crack initiation and deteriorate materials' mechanical properties. [84, 85, 86]

Sufficient Cr content in this metal provides superior corrosion-resistance. Chromium forms a passive oxide layer on the surface of the metal making it corrosion resistant. Too high Cr content, however, decreases the strength of material. Therefore, proper balance should be maintained.

This combination of high strength with superior mechanical properties at elevated temperature makes IN 718 a suitable material for nuclear reactors, rocket engines and motors, gas turbine engines, heat exchangers, and other aerospace and extreme environment applications [85, 87, 88, 89, 90]. It also makes it particularly useful in welding as it provides high resistance to post-weld cracking. Age-hardening alloys can also be easily fabricated, even into complex parts.

4.3 Background

Traditionally, heat exchangers are manufactured by micromachining features into thin sheets of metal and diffusion bonding them together. However, there are some serious limitations to this technique:

- Durability - Point of contact for diffusion bond is weaker facilitating cracks and voids. Discrete micro-voids are observed at diffusion bonded joints from where generally fatigue crack growth occurs. [91]
- Diffusion bonding requires an identical number of channels on both layers in order for the force to be transferred from the top to the bottom layer [92]. This means that the design flexibility is limited thus resulting in limited control over pressure drop and the change in heat transfer coefficients which in turn limits the effectiveness of the heat exchanger. Pressure drop is an undesirable property for the heat exchanger as it increases the power that is required to overcome the flow resistance caused due to pressure drop. A sudden drop in internal pressure could also lead to erosion or failure.

In order to solve these ongoing issues with traditional manufacturing and, to experiment with new, complex design, smallest feature size, additive manufacturing is proposed. AM overcomes the limitations of having high pin density on the hot gas channels side thereby allowing for high heat transfer rates with significantly lower pressure drop. With monolithic design, significant reduction in volume is expected therefore reducing the amount of material required and the cost. Using a 3D printing technique a reliable, versatile and highly effective (>90 %) [93] low pressure drop design HX is expected to be fabricated.

4.4 Objective

Besides 3D printing the heat exchanger, the objective of this work is to study various microstructural fathers (such as grain size, shape, hardness, strength, and defects) and mechanical properties (hardness and yield strength) of additively manufactured Inconel 718. Since AM is a fairly new technique, the microstructural characteristics of additively manufactured parts with respect to design, process, build height are still not fully understood. Due to the high thermal gradient and rapid heating and cooling of AM material, the microstructures produced are complex and different from wrought or cast IN 718. Therefore, it was crucial to perform this study in order to have a holistic understanding of the technique in order to be able to tailor the strength related properties. The specific AM technique used in this work is direct metal laser sintering (DMLS) technique. Although the name DMLS suggests sintering, which means that the powder particles are compacted below its liquefaction point, there is no sintering of powder in EOS. There is simply melting the powder using a focused laser beam. Details on DMLS technique is studied in detail in chapter 4.5.2 below. Various microscopy and mechanical testing tools were used for characterization of 3D printed Inconel 718.

4.5 AM fabrication method

4.5.1 Types of metal AM techniques

There are various types of metal AM techniques, such as powder bed fusion (PBF), direct energy deposition (DED), binder jetting, sheet lamination, etc. PBF uses a spread layer of fine powders to build parts layer by layer. EOS uses a laser beam, and Arcam (now acquired by General Electric) uses an electron beam for melting the powder. Similarly,

in DED, there is a laser versus electron beam melting either wire or powder fed [94]. The binder jet process uses a liquid binding agent to join the powder together, cure, sinter and infiltrate it with another material [95]. Carnegie Mellon University (CMU) owns three types of metal printing machines: EOS, Arcam, and ExOne (a binder jetting machine).

The AM machine used in this work was manufactured by EOS (Electro Optical Systems), a German based laser AM manufacturer that uses laser PBF, sometimes also referred to as direct metal laser sintering (DMLS) or often referred to as a selective laser melting (SLM) technique. The DMLS technique was developed at the University of Texas at Austin.

4.5.2 Direct metal laser sintering (DMLS)

The schematic of a DMLS machine is shown in Figure 4.2a. The EOS M290 that CMU owns is shown in Figure 4.2b with build plate and laser melting of the powder particles shown in 4.2c. The recoater arm from the right spreads the powder to the left side of the compartment on the build platform (although, in the schematics it shows the opposite). An up to 400 W fiber laser beam was used for high quality and precision. The build platform moves down, and the powder dispenser platform moves up after every successful layer spread and melting. The excess powder is collected in the hopper in the left, which is not shown in the diagram. The build platform is generally heated to a low temperature i.e. $\approx 80^{o}$ C. The subsequent spreading and melting of powder is done until the part is fully built.

The steps of creating a computer aided design (CAD) to printing is shown in Figure 4.3. First a CAD design was created (step 1), using SolidWorks^{TM} in this case, converted

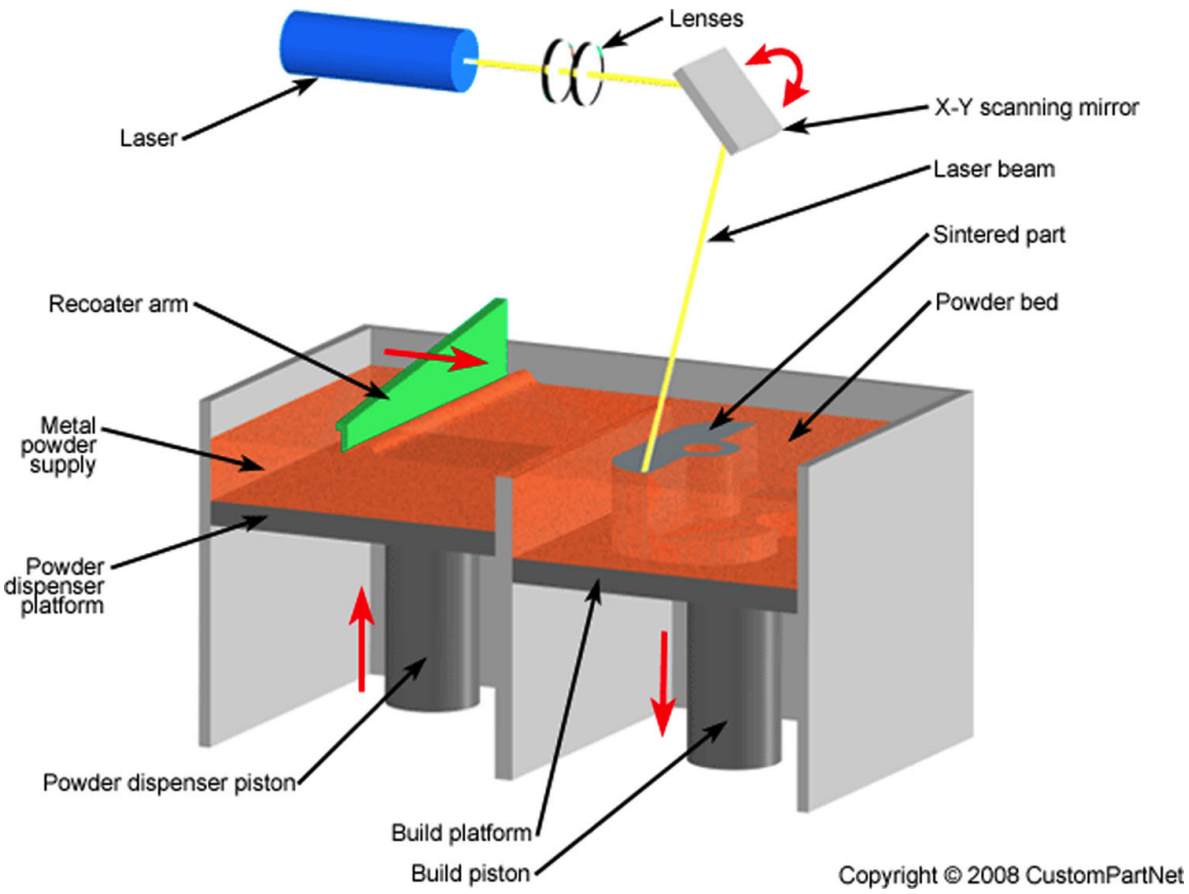

(a)

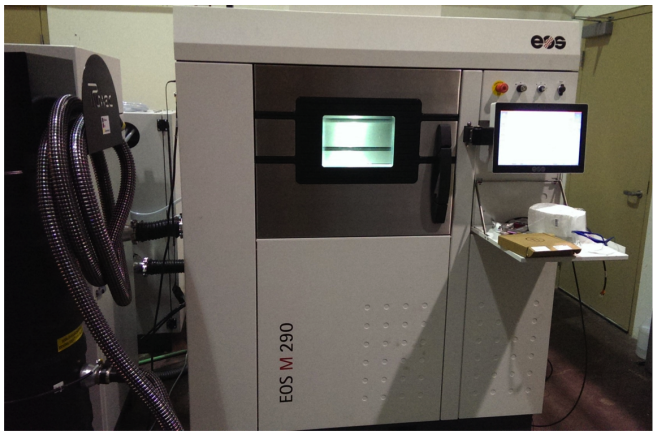

(b)

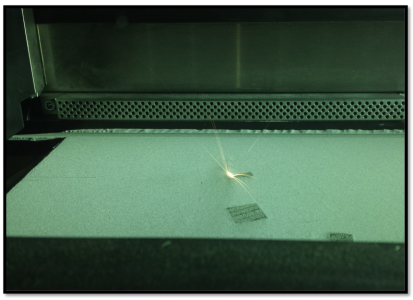

(c)

Figure 4.2: a) Schematics of SLM technique [94] b) EOS at CMU c) build plate showing laser melting of powder.

to .stl and uploaded to a software called Magics^{TM} (step 2). Magics^{TM} is a software that adds support to the part as shown by the structure in yellow. It also checks the contiguity of the part (or any issues) and alerts if there are any dissembled or misaligned joints. After Magics, the file is transported to EOSprint software (step 3) where the part is sliced according to the defined layer thickness. Here, process conditions such as power and velocity of the laser beam, pre and post contour beam settings, layer thickness, exposure and other parameters are also defined. The file is then uploaded to the EOS machine (step 4) and the parts are printed to get the final product as shown in Figure 4.3 in step 5.

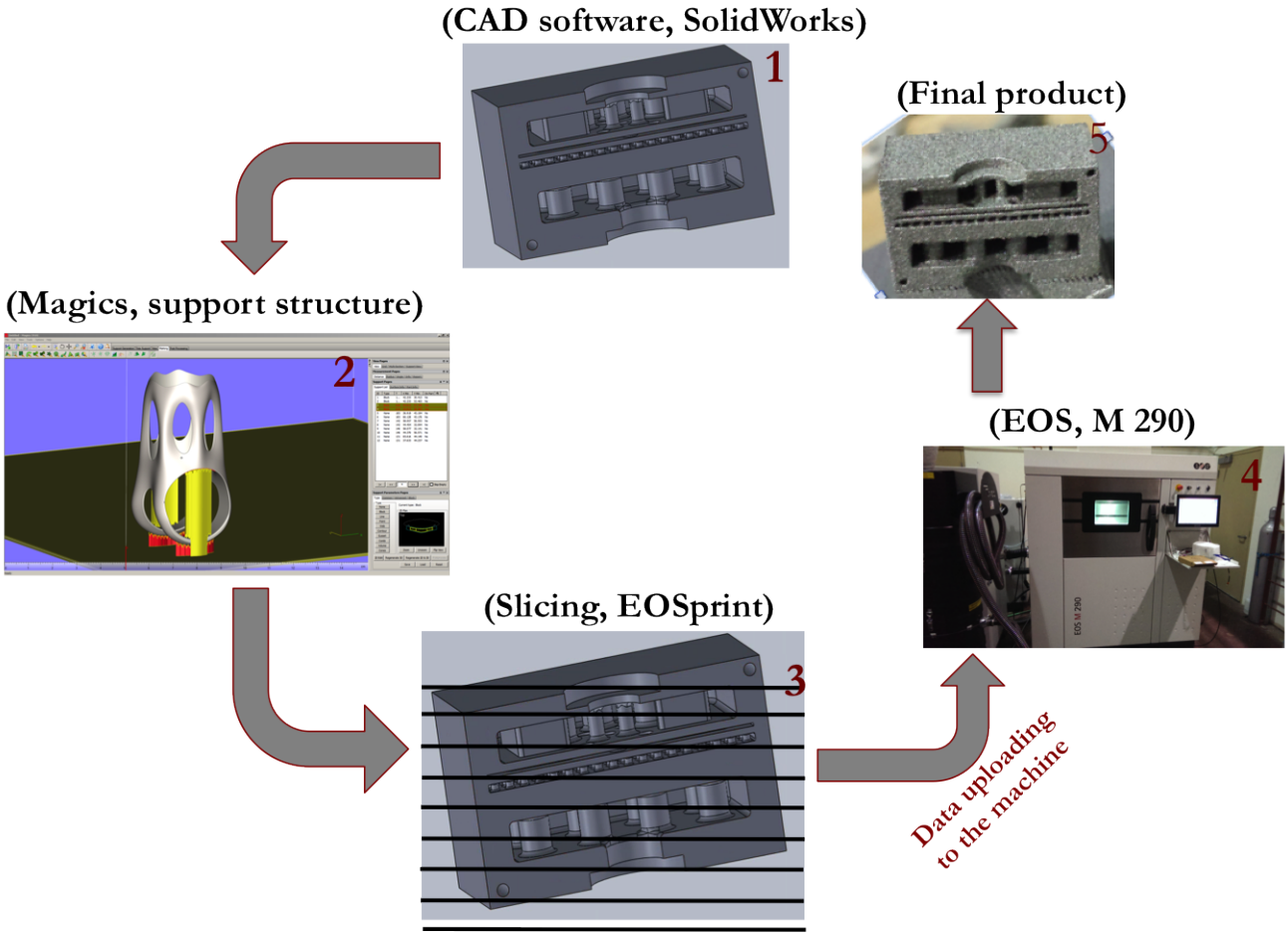

Figure 4.3: Schematics of various stages of metal printing, from design to fabrication.

4.5.3 Why DMLS?

Gas atomized powder provided and/or approved by EOS was used in the fabrication process. The average powder particle size for Inconel 718 was 40 μm. The powder used in EOS is much finer than Arcam and provides a higher resolution and a better surface finish than the electron beam. The objective of this work was to print features as small as 200 μm diameter, therefore, EOS was chosen over Arcam. Since, infiltration of the part with external material was undesirable, ExOne was not an option. Arcam sinters the surrounding bed of powder before melting, which is why there is difficulty in getting the powder out after printing, as compared to the EOS which has loose powder. Another thing to note is, although this thesis is about fabricating HXs using IN 718, in some cases stainless steel (SS) is used, especially in the design testing phase. For example, the part shown in Figure 4.3, step 5, is made out of SS 316 powder and not IN 718.

4.6 Design Consideration

4.6.1 Effect of build orientation

The orientation at which the parts are built greatly determines the part quality because of residual stress. As shown in Figure 4.4, when the heat exchanger is built vertically up, 1) the narrow gap, that was 200 μm, gets pushed upwards by the bending of the structures underneath 2) smaller parts that were only 200 μm in diameter were not built due to insufficient support structure and 3) insufficient support structure resulted in an unfinished surface. All these design inconsistencies can be avoided by tilting the support structure, as shown in Figure 4.4 b. Tilting also helps in reducing residual stress in this method i.e. each layer shrinks and imposes a shortening in the current top layer.

Tilting, therefore, avoids imposing that shrinkage on an entire layer with small pillars. In this case, a 30° tilt was chosen but, in theory, one can go up to a maximum angle of 45°. Angled support provides parts a self-supporting build with a high quality surface finish.

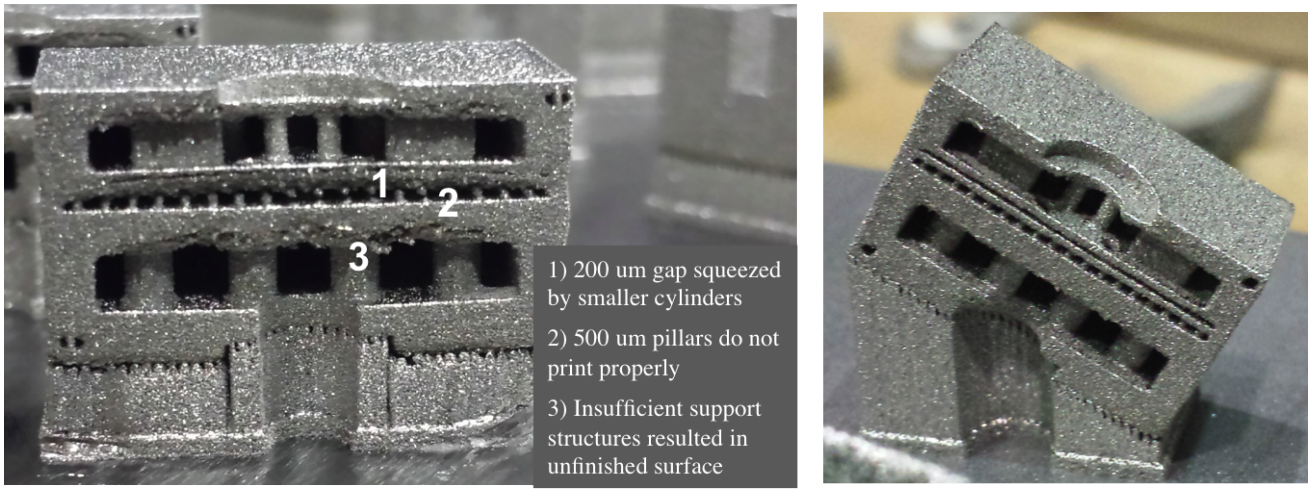

(a) (b)

Figure 4.4: Differences in part quality of a half heat exchanger when having a) vertical support vs. b) 30° tilted support. Tilted ones provide a self-supporting structure. The size of the heat exchanger is 25(l)*10(W)*25(H) mm.

4.6.2 Investigation of small sized features/ Aspect ratio

The resolution of the machine was tested so as to determine the smallest possible feature size in terms of diameter and aspect ratio (height/diameter) that could be fabricated. From the heat transfer simulations, the larger the aspect ratio and the spacing between micropillars, the lower the pressure drop and high heat transfer coefficients [93]. Therefore, pillars with different shapes and aspect ratios were tested. According to the EOS

specification, it is possible to fabricate features that are as small as 40 μm [96], however, the goal is to test the maximum height with respect to that diameter (or aspect ratio) that can be printed.

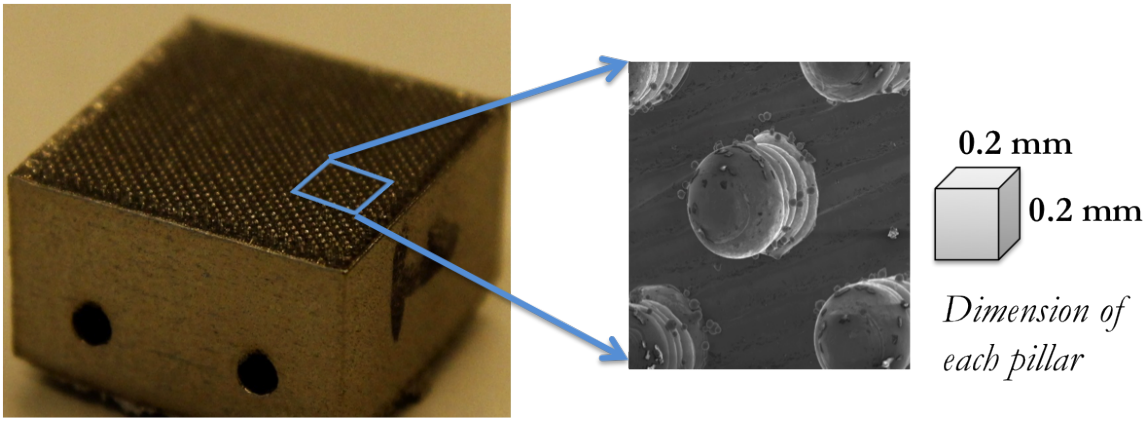

(a)

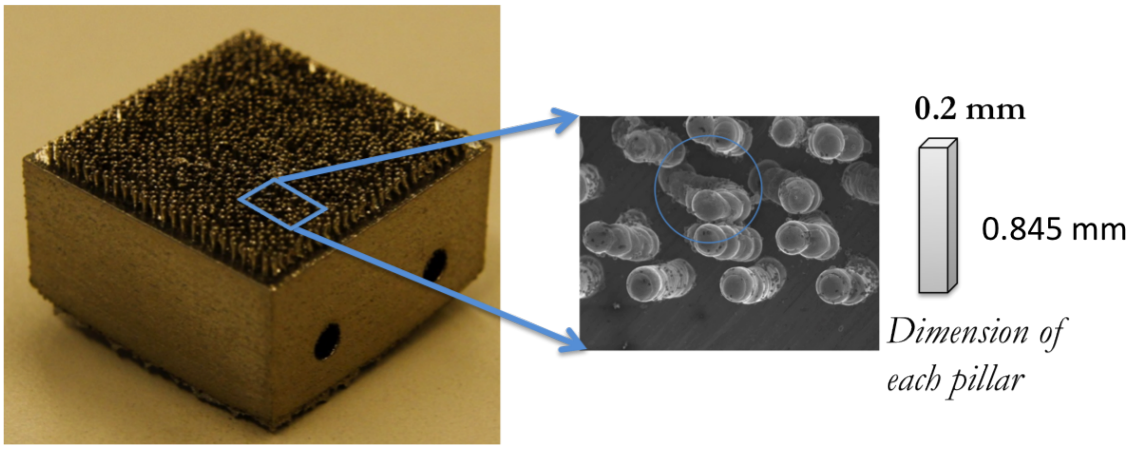

(b)

Figure 4.5: 200 μm diameter pillar with aspect ratio a) 1 and b) 4.2.

As shown in the SEM image (on the right) in Figure 4.5 a), pillars with an aspect ratio of 1 were built properly. The average particle size of IN 718 is 40 μm and it is interesting to note that EOS is capable of melting ~4-5 powder particles into 3D parts.

Each melt pool layer is visible. The SEM images clearly show that the outer surfaces have ridges instead of a smooth surface. This could be an advantage to a manufacturer of a heat exchanger, as this design could provide larger surface area thus higher heat transfer. Therefore, in the future builds this design concept could potentially be utilized. On the other hand, pillars with an aspect ratio of 4.2, as shown in Figure 4.5 b), collapsed (as the one circled in blue) due to the insufficient base. This suggests that there is a height limitation in parts with a smaller base or thin films. Another important thing to note here is that the circular fins are printed although the designs given in were rectangles (as shown in the schematics on the right). This demonstrates that since very few powder particles are melted, the machine is not able to control the shape for a very small feature size.

4.6.3 Process variation

Process variation or 'Process Mapping' is an approach developed by Prof. Jack Beuth's group in mechanical engineering at Carnegie Mellon University to control melt pool geometry with different input process parameters such as power and velocity (PV) of the laser beam. Process mapping of Inconel 625 in laser based powder additive manufacturing is shown in Figure 4.6 [97]. This graph is the work of Colt Montgomery obtained after examining multiple iterations of PV combinations and assessing the effective melt pool area, width, and depth. As shown in Figure 4.6, at a constant high power, low velocity could introduce keyholing porosity, and high velocity could give lack of fusion defects. Similarly, low power could result in incomplete melting, and high power could potentially overmelt the powder into flames [98]. Thus, it is very important to choose the right combination of PV. With smaller features, at a constant high power, an increase in velocity produces smaller melt pool width and thus help product parts with increased precision or tolerances [97].

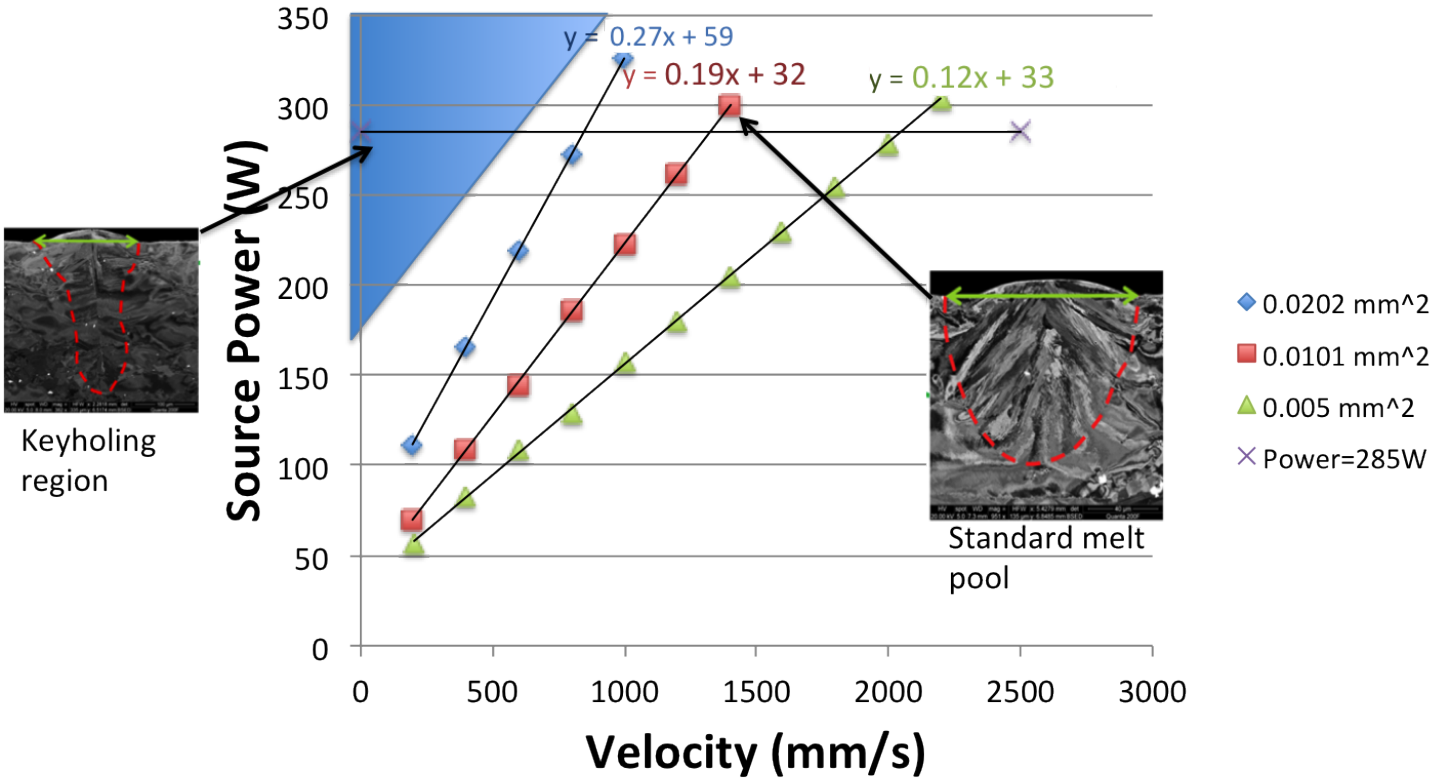

Figure 4.6: Curves of constant cross sectional area IN 625 [97]

.

From a design perspective, micropillars with a larger aspect ratio and larger spacing have proven to give lower pressure drop and high heat transfer coefficients [93]. Thus, three designs micropillars with different aspect ratios and shapes, as shown in Figure 4.7, were tested with different process settings:

1. 200 μm (W) * 200 μm (H), aspect ratio (H/W) = 1, square shape

2. 200 μm (W) * 845 μm (H), aspect ratio = 4.2, square shape

3. 200 μm (W) * 845 μm (H), aspect ratio = 4.2, tear-drop shape

The diagonal spacings between the squares for design a and b are same i.e. 494 μm, while the spacing between tear drops for design c is larger, i.e. 780 μm due to the

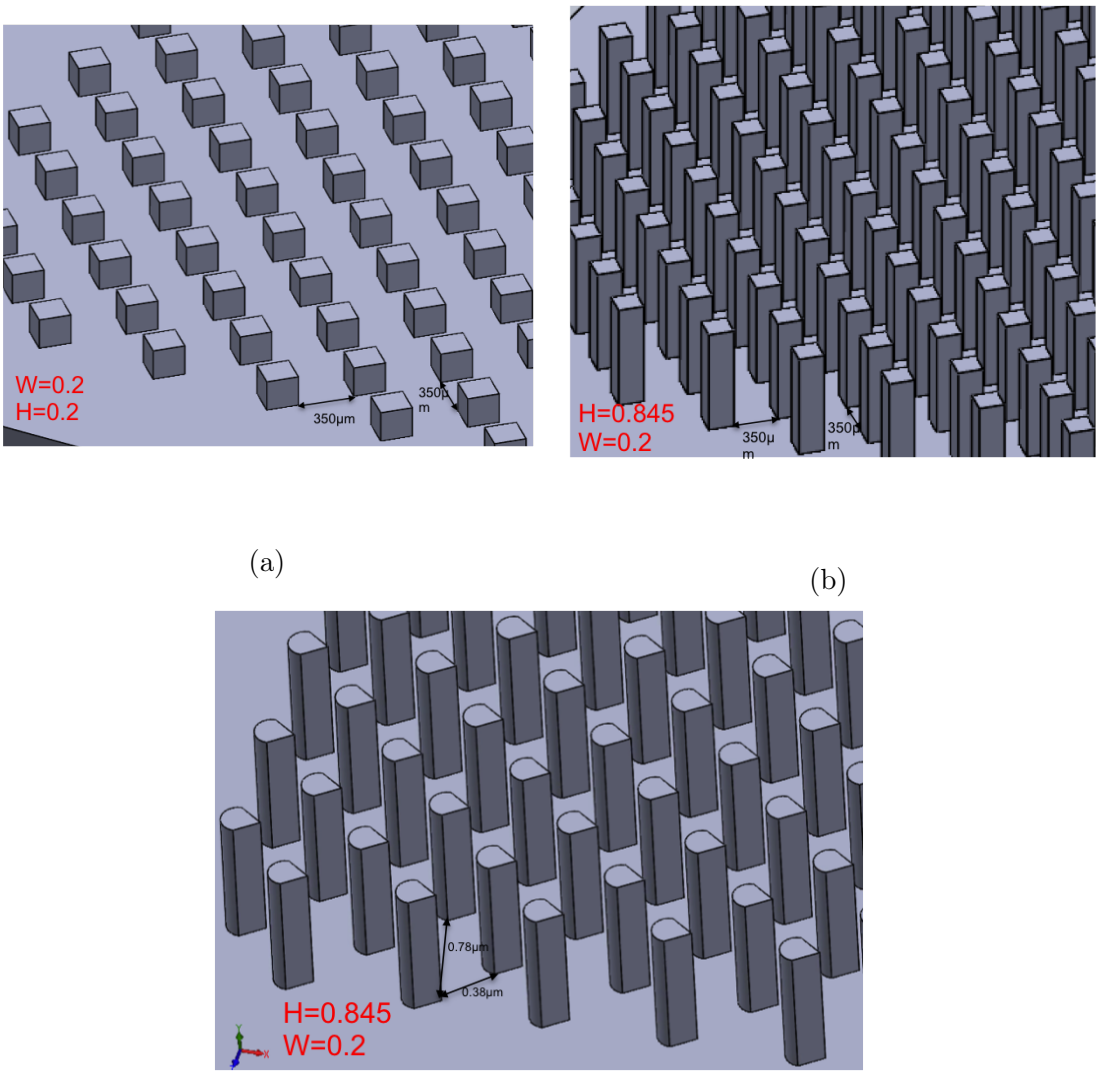

Figure 4.7: Fins with aspect ratio a) 1 b) 4.2 and c) 4.2 but tear drop.

nature of the tear drop shape.

As shown in Figure 4.8, irrespective of the PV combination used, aspect ratio = 1 (200 μm $\times$ 200 μm) fins are built as designed. For all PV combination, the tear drop design seems to have a better finish than the square design. This could be because the spacing for the tear drop design is larger than that of the square design. Changing the

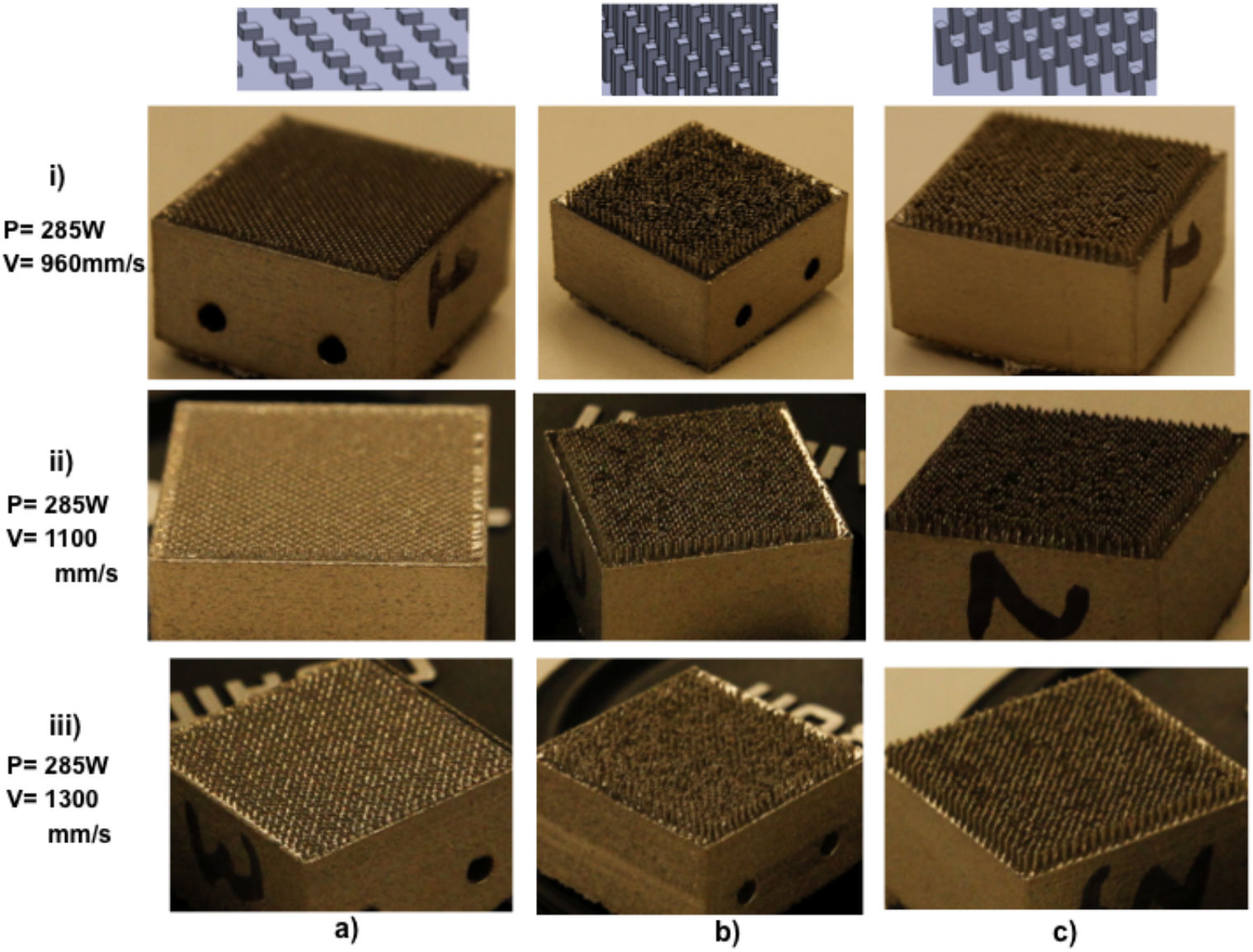

Figure 4.8: HQ picture of 3D printed parts showing three fin types with aspect ratio a) 1 b) 4.2 and c) 4.2 but tear drop shape for three different PV combination used for direct part i), ii), and iii) with PV values for outer skin direct part (or primary exposure) shown in the figure. Post contour settings for set i), ii) and ii) are 300 mm/s, 138 W and 400 mm/s, 138 W and 500 mm/s, 138 W respectively.

PV combinations did not make any visible differences to the smaller feature. They all had regions where channels were falling down or not built as designed. Hence, it was concluded that the aspect ratio= 4.2 is too high to get a good quality finish for 200 μm

diameter parts. Additional fins with aspect ratios of 2 and 3 with varied spacing were designed, however, due to constraint in resources, only the three shown in Figure 4.2 could be printed and verified.

4.6.4 Residual stress

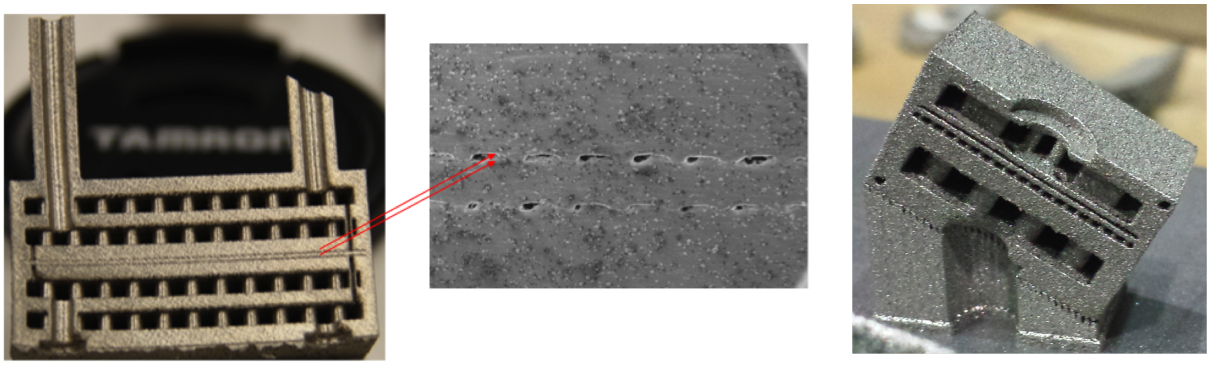

(a) (b)

Figure 4.9: a) IN 718 half section of a heat exchanger with 200 μm pillars that were inserted between the bulk parts b) SS 316 half section of a heat exchanger that shows that 500 μm pillars are fabricated successfully.

Although 200 W $\times$ 200 H μm micropillars were formed in a freely standing surface, it was of interest to see whether or not they remain intact when incorporated in a heat exchanger. As show in Figure 4.9a, the pillars were squeezed between bulk materials above and below. This is because of the high residual stress in Inconel 718. Residual stress is the "stress in a body which is at rest and in equilibrium and at uniform temperature in the absence of external and mass forces. The dynamic temperature distribution and heating/cooling rates along the part - which consists of high thermal gradients and repetitious/rapid local heat transfer rates - are known to cause residual

stress" [99]. Thompson et. al mentioned that materials such as Inconel 718 with higher yield stress and high yield strength at high temperature experience a greater residual stress [99]. This is due to the higher strain mismatch at elevated temperature compared to other softer materials such as SS 316, whose strain mismatch is lower as the temperature increases and thus the yield stress decreases with increase in temperature. Shamsaeia et al. also mentioned that IN 718 has 1.5 times higher residual stress than SS 316 [99]. The presence of residual stress leads to the plastic deformation in material and could also permanently deform the parts [100]. Similarly because of the very high residual stress the parts warped resulting in deformation of some of the micropillars.

Residual stresses are more pronounced in EOS compared to the Arcam because of the low pre-heat in EOS i.e. $\sim 80^{o}$ C. The thermal gradient between "the peak melting temperature and powder-bed temperature" is large [94]. This large change in temperature (from the freezing point) results in high thermal contraction. Residual stress can be minimized in various ways such as changing the hatch type (solid vs. lines) of the support structure, controlling process parameters [101], change in scan strategies/patterns [94], or heat treating parts after the build which helps to relieve stress. But if the dimensional accuracy of the part is changed, then it can not be recovered.

In contrast to 200 μm, 500 μm cross-sectional diameter micropillars were built as designed when fabricated inside a heat exchanger, as shown in Figure 4.9b. This suggests that although an aspect ratio of 1 micro pillar with diameter 200 μm can be fabricated in a free surface, when incorporated in a heat exchanger design at least 500 μm diameter should be chosen.

4.6.5 Powder removal design

Powder removal is one of the most discussed topics in metal 3D printing [102, 103]. In EOS the powder is not sintered unlike Arcam therefore, there will be loose and unsintered powder. Although, with EOS it is not as much of an issue, the intricate design and closed spacing of heat exchanger required an investigation on powder removal.

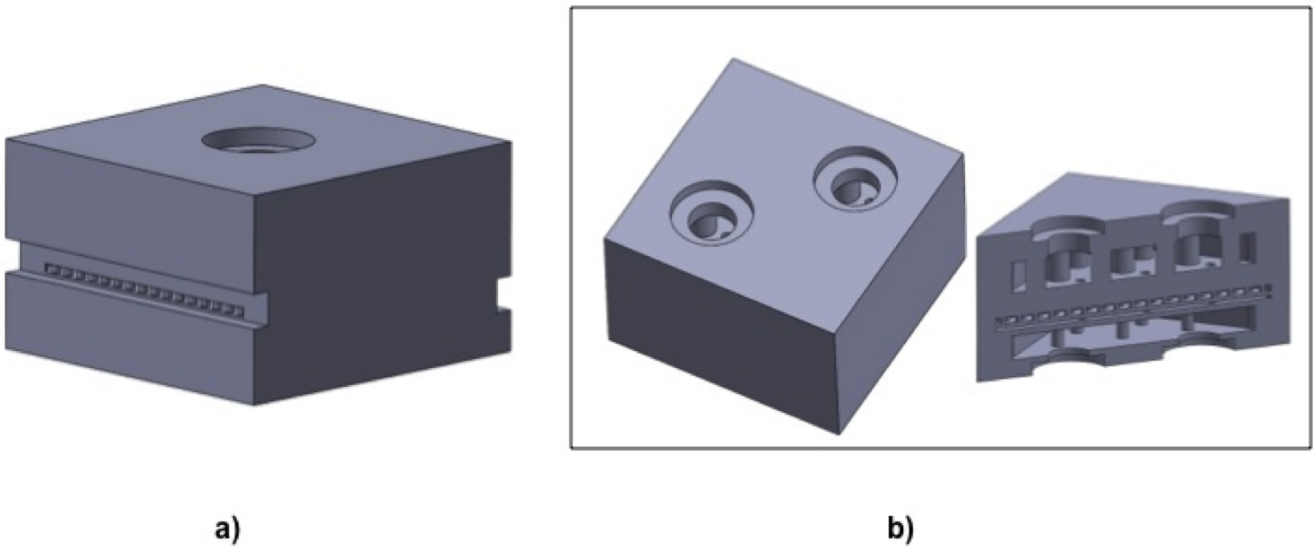

Figure 4.10: Two powder removal designs tested: a) One with the plenum or openings on the side and another b) with two large holes on the top and on the bottom.

As shown in Figure 4.10 two types of heat exchangers were designed: one that had openings on the side (Figure 4.10 a) and another that had two bigger holes on top and on the bottom (Figure 4.10 b). With the first design, post welding of a piece on the sides is required so it is not a desirable design. Both types of HXs were designed and powder removal tested. Parts were submerged inside water and air blown through to remove the powder from all the interior channels. It turned out that both the designs were equally effective for powder removal.

4.7 Hypothesis

First we hypothesize that it is possible to fabricate monolithic microchannel heat exchangers using a laser based 3D printing technique with the nickel-chromium superalloy IN 718. Depending on the design, build height, process condition, microstructural and mechanical properties such as grain size, shape, hardness, porosity, strength are hypothesized to vary.

4.8 Characterization tools

Once the HXs were fabricated, various microstructural and mechanical testing tools were used to perform characterization of printed parts.

4.8.1 Electron backscatter diffraction (EBSD) and sample preparation

Electron backscatter diffraction (EBSD) indexing system or Orientation Imaging Microscopy (OIM) was used to capture grain orientation, size, shape, and texture information. EBSD is a Scanning Electron Microscopy (SEM) based electron diffraction technique used for measuring crystallographic orientations at a spatial resolution of $\sim$50 nm. As shown in Figure 4.11, an EBSD system consists of a polished crystalline sample tilted at 70° from the horizontal. The sample was polished on a mechanical polisher using Silicon Carbide (SiC) grit papers until the sample surface was flat and smooth. 9 and 3 μm oil-based diamond suspension polishing was done using an ApexHercules H grinding disc and a Trident cloth respectively for 5 mins using a load a 6 lbs and base speed of 120-150 rpm. Final polishing was done using a colloidal silica slurry in a mechanical polisher for 2 minutes followed by a Vibromet^{TM} for $\sim$3 hours to obtain a

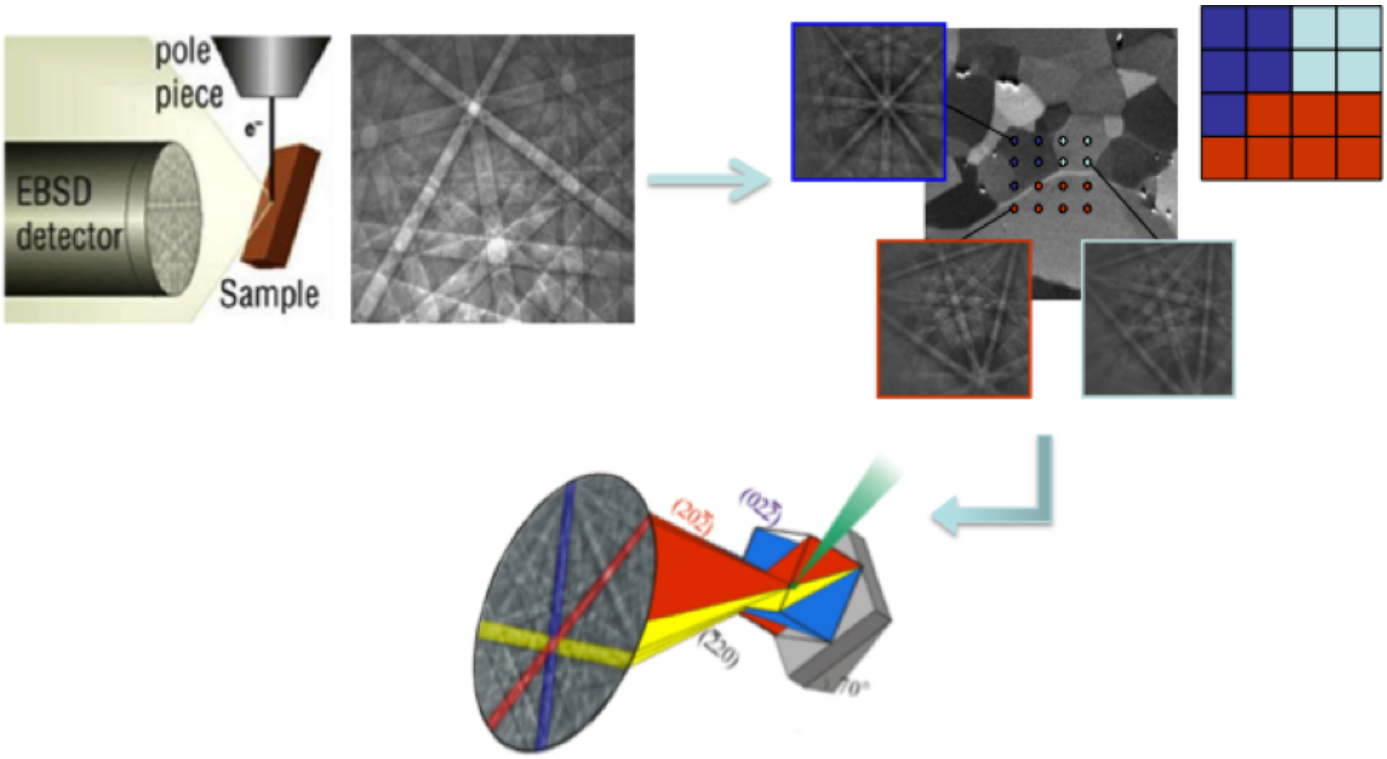

Figure 4.11: Schematic showing EBSD pattern formation and indexing [38, 104].

high quality, scratch free surface finishing for EBSD [105].

As the incident electron beam hits the polished surface (∼20 nm deep), it diffracts from the sample following Bragg's law:

$$n\ \lambda = 2\ d\ sin\theta \tag{4.1}$$

where n is the order of diffraction, λ is the wavelength, d is the spacing of reflecting planes, and θ is the angle of incidence. These diffracted electrons are then captured on a phosphor detector creating an Electron backscatter diffraction pattern (EBSP) as shown in Figure 4.11. Each EBSP consists of several bands known as 'Kikuchi bands', each one of which represents a unique crystallographic plane. The width of the Kikuchi band is related to the interplanar spacing, d, as shown by the Bragg's law. All the Kikuchi bands intersect at a point in a pattern to form a zone axis [106]. The angle between the bands relate to the angle between the planes. Thus, by analyzing these EBSPs, through

a method known as Hough Transform combined with peak identification, which converts bands in an angular space to points in a Cartesian space, crystallographic orientation information at each point is determined [107]. Furthermore, using EBSD, the spatial distribution of the orientation in the microstructure is obtained which can then be used to find orientation spread. EBSPs could be further used to characterize grain, grain boundaries, crystallographic orientation, texture, Schmid factor, grain misorientation, phaseID, strain and various other microstructural parameters [106]. EBSD is a standard tool used for characterization because of less difficulty in sample preparation and its ability to scan a large area compared to TEM.

4.8.2 Hardness testing

HR or Rockwell hardness was measured on 3D printed metal parts. HR is an indentation based testing method that gives a hardness value or property of a material that directly correlates with its tensile strength, and other properties. C in HRC is one of the scales that has a diamond cone indentor and is used to measure the hardness of steel, iron and other high strength materials. The indentor presses into the material until equilibrium is reached. The measurement of the depth of the penetration gives the Rockwell hardness number. Conversion table enables comparison with micro-hardness values.

4.8.3 X-ray computed microtomography

Defects or pores in metals can be detected in many different ways. One of the ways is by cutting and polishing a section of the sample. This, however, only gives the 2-D information and requires destroying the sample. Therefore, in order to capture 3-D information without cutting open the parts, techniques such as ultrasonic inspection or x-ray inspection are used. Ultrasonic inspection is very sensitive to surface roughness or grain noise. [108]. Therefore an x-ray CT technique is used as it works on the principle

of differences in densities between metal parts and pores and is a powerful tool to resolve complex internal features.

X-ray imaging is widely used in the medical industry where based on absorption of x-rays, 3-D parts of the human body are projected on a 2-D surface. Similar to this technique, CT imaging also works on the principle of x-ray absorption but gives a 3-D projection of a part. The word tomography is a greek word, where “tomos" means “slice” and “graphy" means “imaging by sections". In x-ray CT, 2-D images of the object are combined to reconstruct a 3-D image. X-ray CT in this study was performed at Advanced Photon Source (APS) at Argonne National Lab. The APS facility at Argonne is shown in Figure 4.12 a and x-ray CT setup is shown in 4.12 b.

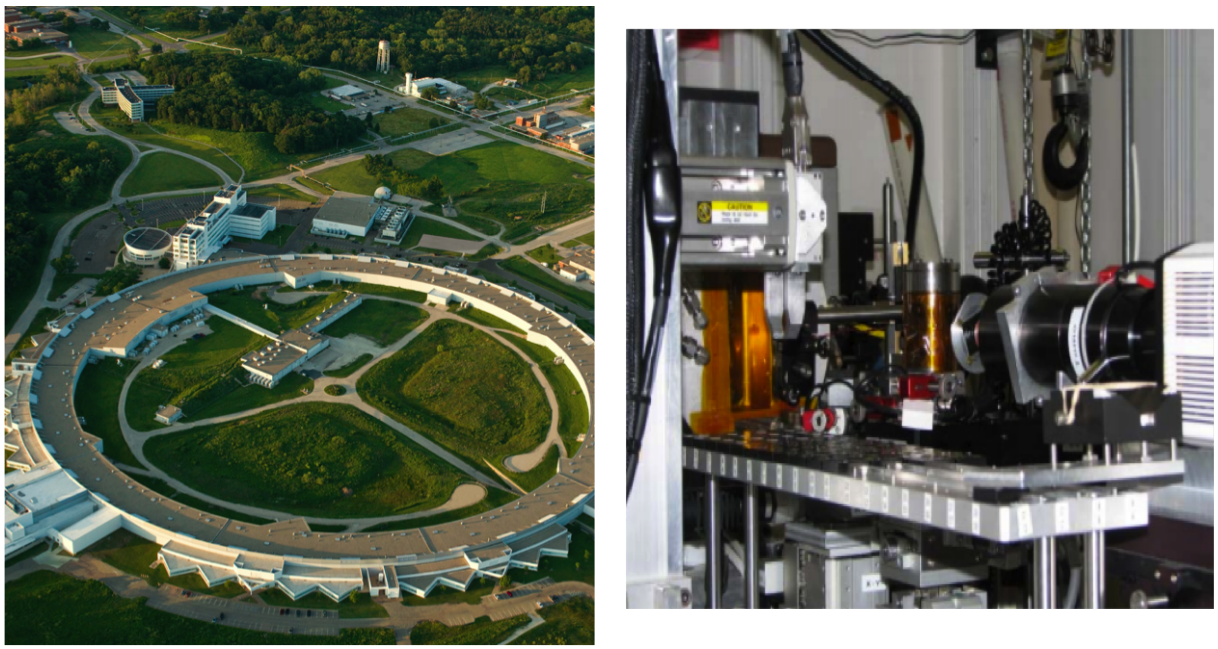

(a) (b)

Figure 4.12: a) Advanced Photon Source, Argonne National Lab [109] b) 2-BM or x-ray computed tomography setup at APS.

The working principle behind this technique is based on Lambert-Beer law where,

$$I = I_o e^{-\mu x} \tag{4.2}$$

I_o = X-ray intensity before reaching the object

μ = absorption coefficient

I = X-ray intensity after passing through the object

x = thickness of the absorbing material

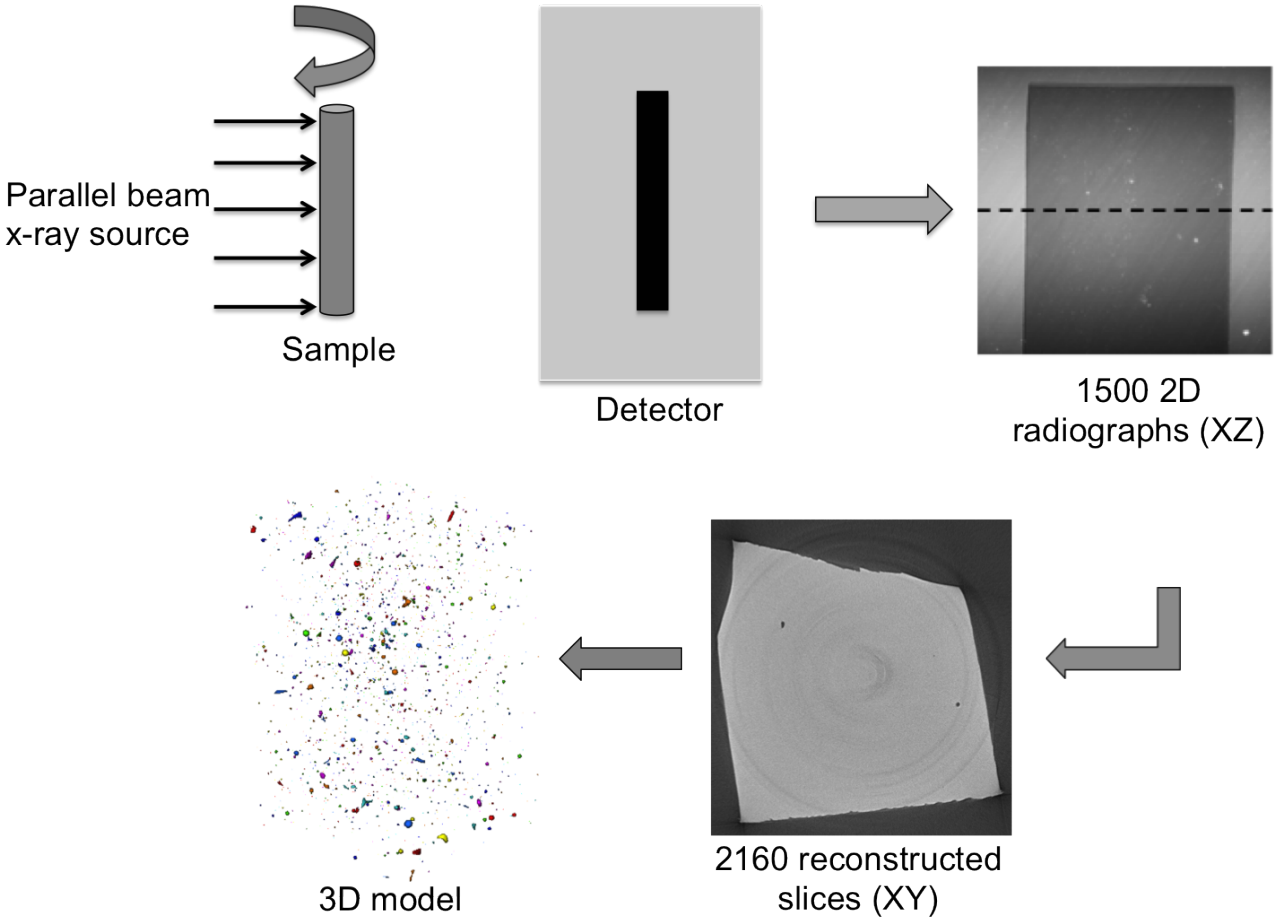

Figure 4.13: X-ray CT setup from capturing the radiographs to reconstructing a 3D model [120].

As can be seen in Figure 4.13, high energy x-rays that have a voltage of 60 KV with

white beam were penetrated through the sample and the image projected onto a detector. A white beam was used to provide sufficient constant and penetration depth. Maximum sample size was 1 mm in diameter. The samples were rotated 180^{o} to capture 1500 2D projections that were later translated into 2160 2D reconstructed slices. Each sample requires about 2 mins to scan with a 50 ms of exposure time. X-ray CT is a very powerful tool that can resolve features as small as 0.65 μm for a 1 mm diameter sample [120].

Each data set was about $\sim$ 30 GB in size and took about 2-3 hrs for reconstruction. Reconstruction was done using a software provided by Argonne National Lab scientists known as TomoPy, where Tomo refers to Tomography and Py refers to a python code used for reconstruction. After reconstruction, the software used for 3-D visualization was Avizo 9. Avizo gives the pore size, shape and diameter information with many other advanced features.

4.8.4 Micropillar compression test

This work is in collaboration with Prof. Javier Llorca and his group at University of Madrid, Spain.

Rockwell hardness gives the macro or bulk material property. In order to get the local stress-strain property micro pillar compression tests were carried out. Micropillars were milled using Focused Ion Beam (FIB) with a diameter of 4.3 μm and height 10 μm. Aspect ratio was 2.3 in order to avoid any buckling while compression [110]. SEM and EBSD scans of the region of interest were taken before and after the milling. Pillars were compressed using a circular diamond flat punch of 10 μm in diameter inside an instrumented nanoindentation system (Hysitron TI950) [110].

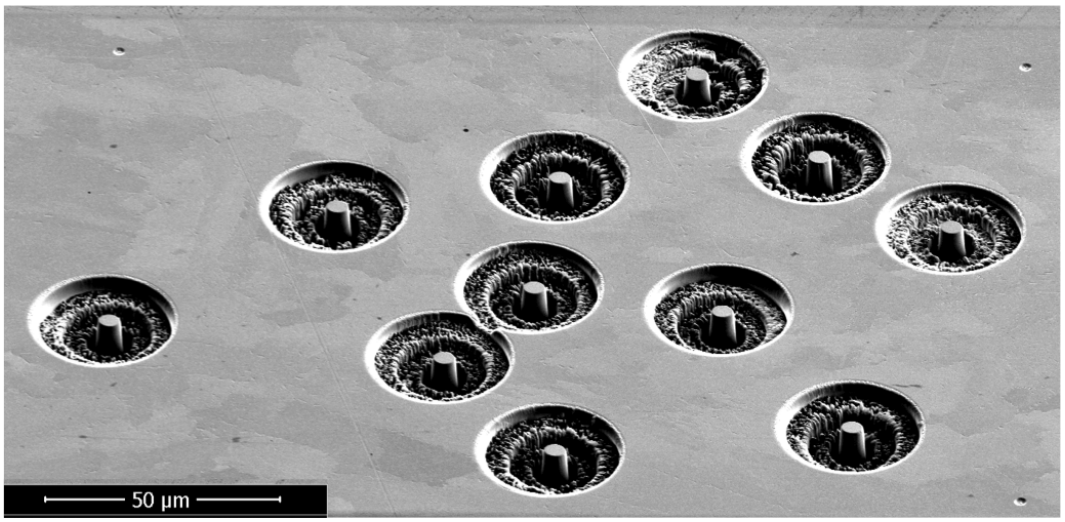

Figure 4.14: SEM image of micropillars located at various parts of the sample.

4.9 Results

4.9.1 As fabricated stainless steel

Initially, heat exchangers were fabricated using stainless steel 316 powder. This was done in order to test the design and to have an idea of what design modifications were needed for fabrication. The layer thickness used for printing was 40 μm.

Characterization of 3D printed stainless parts was done using Electron Backscatter Diffraction (EBSD). As shown in the CAD design in Figure 4.15, EBSD scans were taken from three different build heights, and different designs were considered (bulk vs. small pillars). Grain size, shape, and anisotropy were analyzed.

4.9.1.1 Grain size

As shown in the IPF maps in Figure 4.16 a) and g) that corresponds to scan 1 and scan 3 respectively in Figure 4.15, grains in the bulk of the sample were coarse, highly elongated, and columnar along the build direction. Columnar grains could be due to

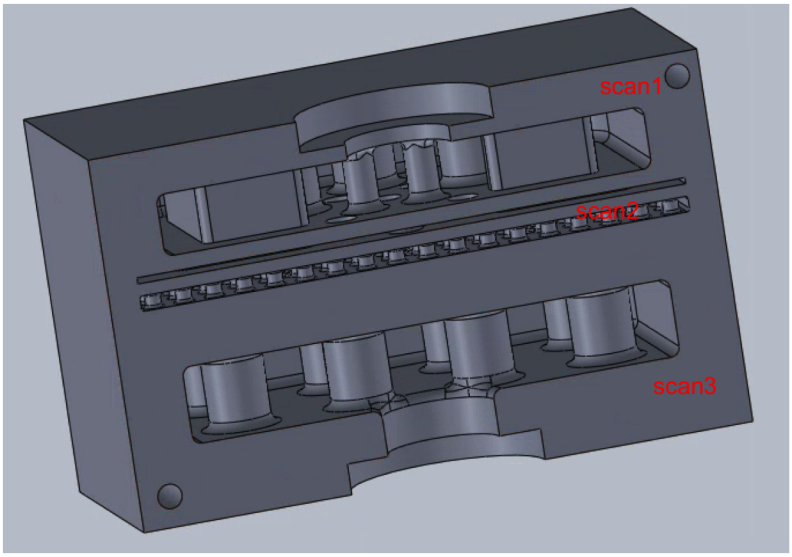

Figure 4.15: SolidWorks^{TM} drawing of a part where EBSD scans were taken at three different build heights.

directional solidification, because the solid metal part surrounding it could act as a heat sink. [111, 112, 113]. However, grains in the smaller pillar (scan 2), that corresponded to Figure 4.16 d), are small and equiaxed. The equiaxed microstructure could be because the smaller pillars are surrounded by powder particles around it, and heat flows in all directions as compared to the bulk, where it would be mostly directional.

In order to perform a more quantitative analysis, a probability plot was drawn. Probability plots are a "graphical technique for assessing whether or not a data set follows a given distribution such as the normal or Weibull." [114]. In Figure 4.17 the actual data set is represented by a solid line and the normal distribution is plotted with a dotted line. Grain size distributions generally follow the lognormal distribution and if the data were to truly follow log-normal distribution, they would all fall in a straight line. [115]. Deviation in the lower part of the line is known as lower tail departure and similarly, the deviation in upper tail is known as upper tail departure. Grain size distribution for scan 1 and 3 were plotted in Figure 4.17 which show that there is minimal to no different between

grain size on the top and on the bottom of the HX. There is a slight difference between the two data sets in the upper tail but it is not very significant. For both scans, there is a significant lower tail deviation which means that there might be many smaller grains.

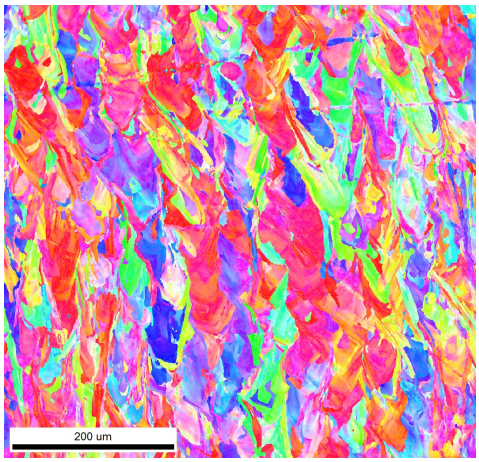

(a)

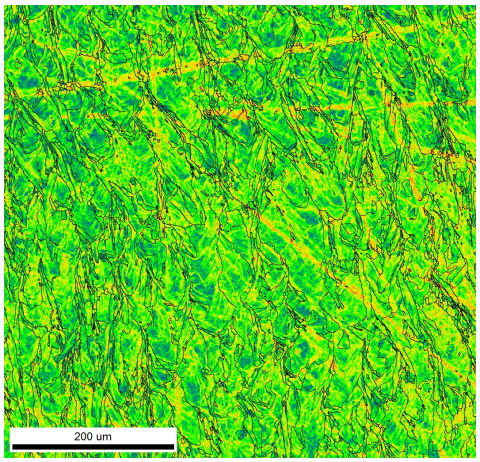

(b) Average KAM:1.65

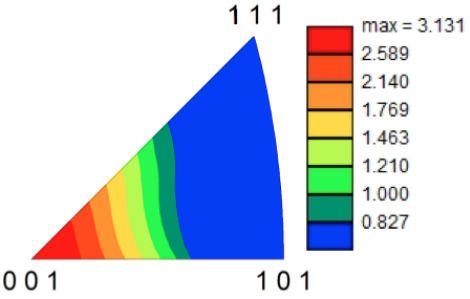

(c)

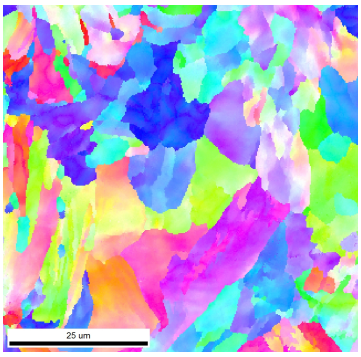

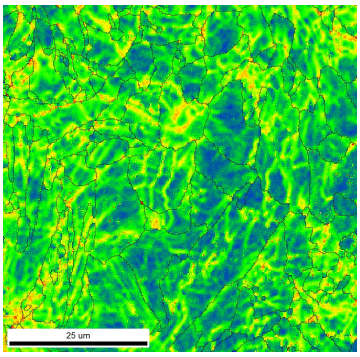

(d) (e) Average KAM:1.28

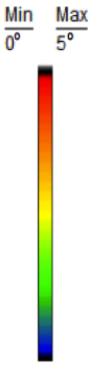

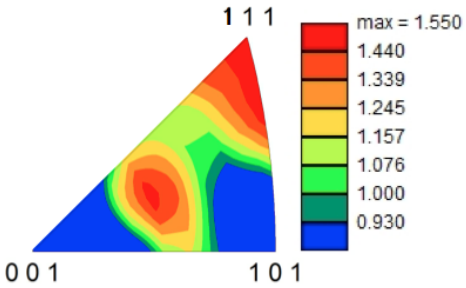

(f)

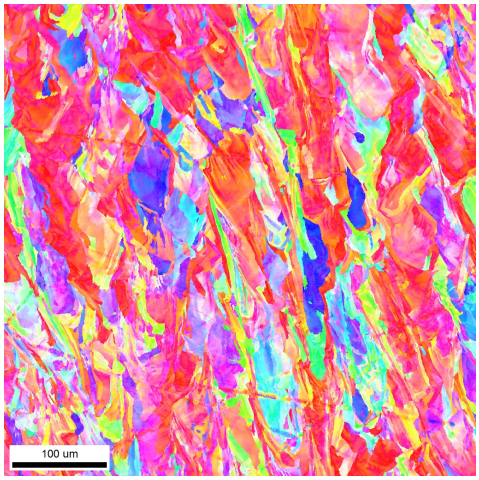

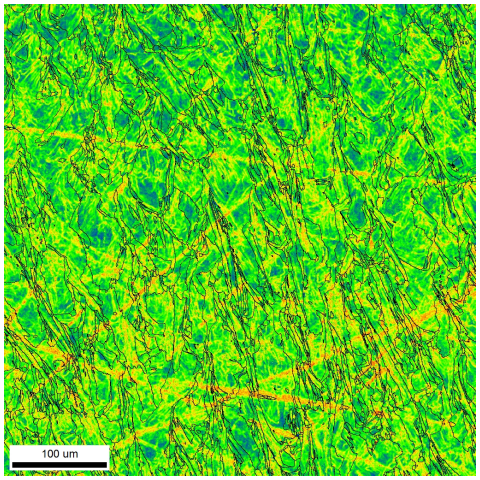

(g) (h) Average KAM: 1.63

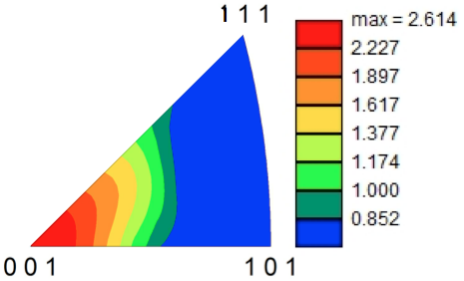

(i)

Figure 4.16: Scan 1 a) IPF map b) KAM c) IPF, scan 2 d) IPF map e) KAM f) IPF and scan 3 g) IPF map h) KAM i) IPF for Stainless Steel 316. KAM color bar is same for all three maps.

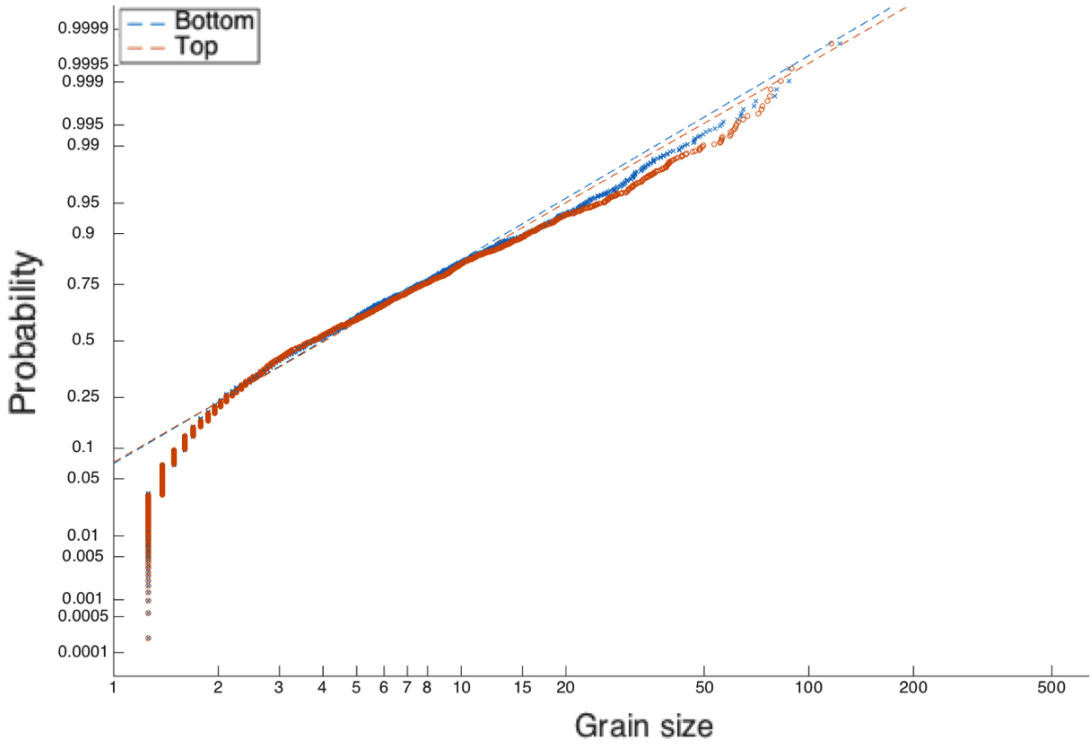

Figure 4.17: Grain size distribution for scan 1(top) and scan 3(bottom) for SS 316 EBSD scans.

4.9.1.2 Grain shape

Grain shape is quantitatively measured in terms of the average aspect ratio of grains. The aspect ratio of a grain is the ratio of its shortest diameter by its longest diameter. Krstic et al. reported that the "aspect ratio of the grain is the most important microstructural feature that controls mechanical properties in Si_3N_4 ceramics" [116]. As shown in Figure 4.18, the aspect ratio of grains in the pillar section is closest to 1 compared to scan 1 or 3 that are from the bulk of the sample. This means that the grains at the pillars are more equiaxed. Aspect ratio closer to 1 means that the grains are equiaxed and the aspect ratio closer to 0 means that the grains are highly elongated. Also, the shape distribution for all three scans, suggest a mixture of 1) a set of grains with shape=0.7, and 2) a broad distribution of high aspect ratio grains. This quantitative description,

therefore, supports the qualitative observation seen in Figure 4.16 a and g.

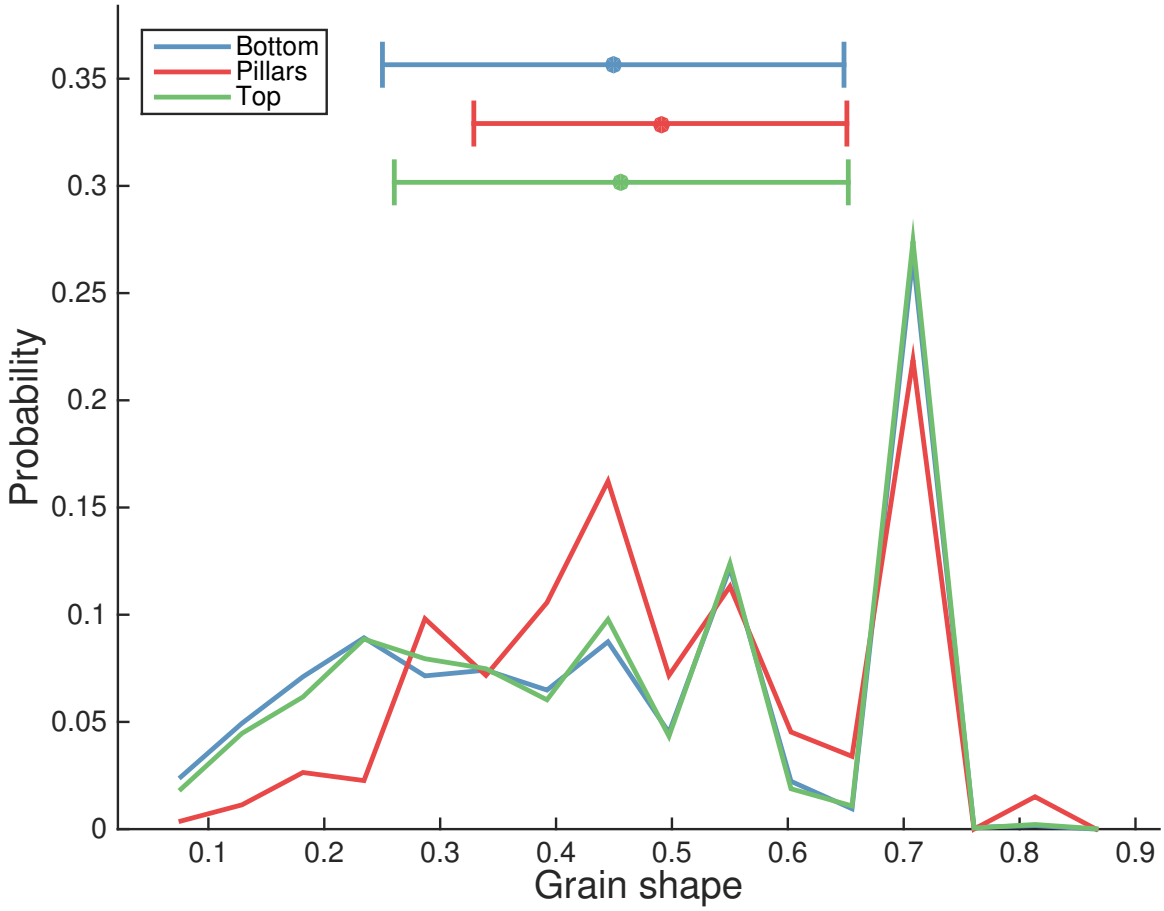

Figure 4.18: Grain shape distribution for scan 1 (top), scan 2 (middle) and scan 3 (bottom) for SS 316 EBSD scans.

4.9.1.3 Orientation gradient

As observed in IPF maps in Figure 4.16 a) and g), grains are highly anisotropic and oriented in ⟨001⟩ direction as shown by the dominant red color. ⟨001⟩ is the growth direction for fcc (face centered cubic) and bcc (body centered cubic) structures [117]. The strong ⟨001⟩ fiber texture is also represented in IPF standard stereographic triangle (SST)

in Figure 4.16 c) and i). MRD value of ~ 3 means that the $\langle 001 \rangle$ fiber texture in the IPF map is 3 times stronger than a random texture. The IPF is a normalized representation of all the orientations in the EBSD map. It makes it easier for visualization and helps assess the maximum intensity of orientation in a particular direction. By contrast, grains in scan 2 are highly isotropic, equiaxed and randomly oriented with less orientation gradients in them. Texture in smaller pillars is less strong as the bulk microstructure. This is also clear in the IPF that shows that the orientation is more homogeneously distributed. Another thing to note here is the melt pool region in scan 1 and 3 IPF maps.

KAM values for scan 1 and 3 are shown in Figure 4.16 b) and h) is higher than scan 2. From the previous study, as shown in Appendix B, higher KAM values signify larger local orientation gradient and higher accumulated strain. This indicates that scan 1 and 3 have higher dislocation density than compared to scan 2. There is no clear indication as to whether gradient is higher at the grain boundary compared to inside the grain in any of the 3 cases.

The above mentioned analysis indicates that microstructural properties for different build height for SS 316 were the same but depending on part geometry and morphology they could vary. Similar studies were performed in Inconel 718 HXs which will be discussed in the following sections.

4.9.2 As fabricated Inconel 718

4.9.2.1 Grain size and shape

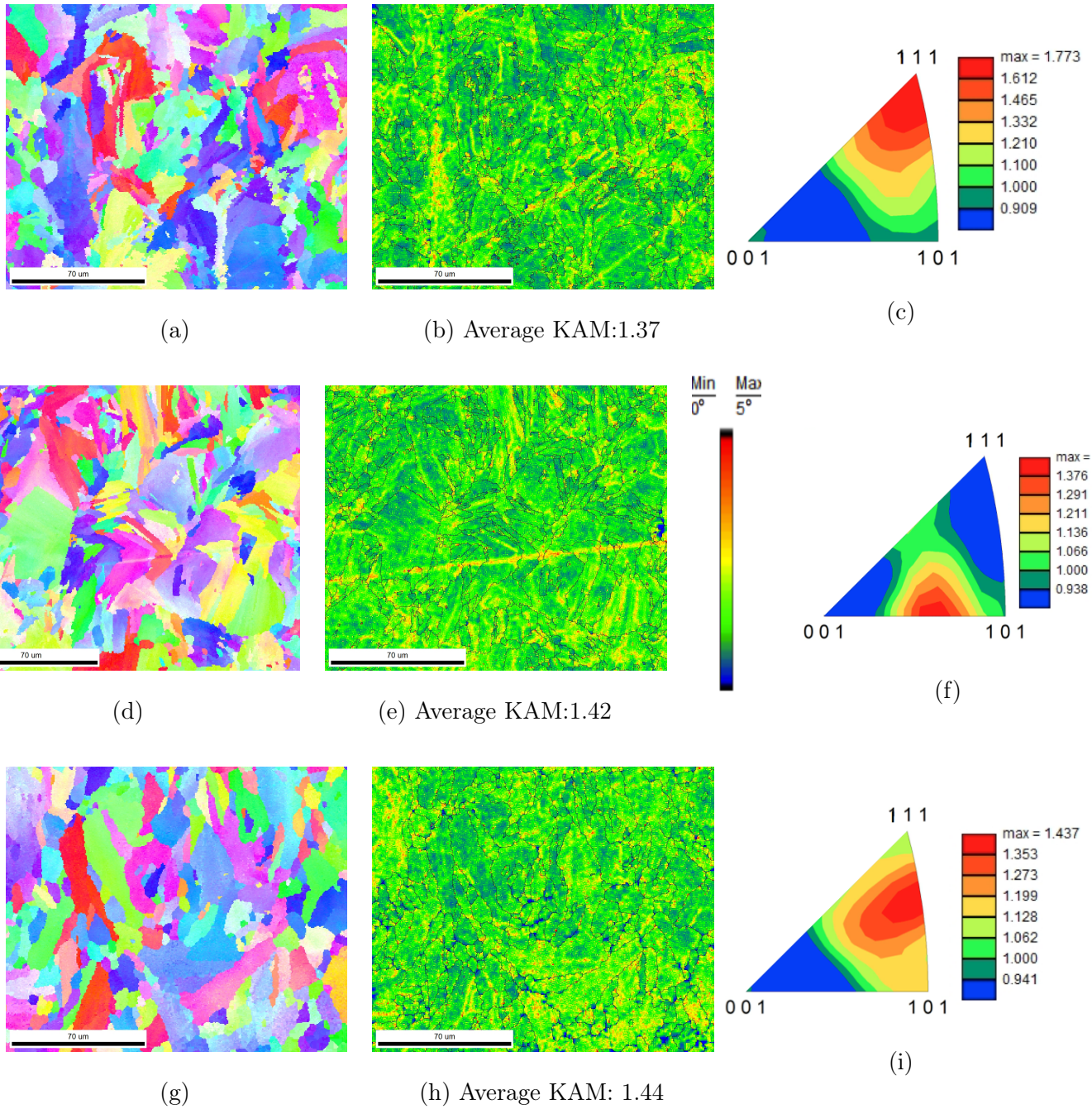

Figure 4.19: Scan 1 a) IPF map b) KAM c) IPF, scan 2 d) IPF map e) KAM f) IPF and scan 3 g) IPF map h) KAM i) IPF for Inconel 718 at three different build heights. KAM color bar is same for all three maps.

Similar to SS 316, EBSD was used to characterize grain size and shape information. IPF, KAM and IPF triangles drawn from three different parts of a HX (scan 1, scan 2 and scan 3 respectively) are shown in Figure 4.19. Although IN 718 has an FCC crystal structure and $\langle 100 \rangle$ is the favored growth direction, grains were not highly oriented in $\langle 111 \rangle$ direction as seen with SS 316. As shown in the Figure 4.19 grains for all three scans are isotropic and randomly oriented. This could be attributed to the slower cooling rate of Inconel 718 (i.e. 6.5 - 11.4 w/m.k) as compared to that of Stainless Steel (i.e. 13-17 w/m.k). A slower cooling rate could have led to a more random structure. Rapid solidification or higher cooling rates lead to a more heterogeneous microstructure.

Similarly, the average KAM values for all three maps are similar, unlike what was seen before with SS 316. Qualitatively, all three IPF maps look essentially the same. Therefore a statistical analysis was done. Probability plots of grain size and shape for all three scans are shown in Figures 4.20 and 4.21. The mean grain size of the scan at the bottom (that is closer to the build plate) is higher than the scan at the top and the middle. All three plots show lower tail deviation. The grains on the top scan show the most upper tail deviation. The aspect ratio of the grains in the middle section is slightly smaller than that of the top and bottom, as shown in Figure 4.21. This means that grains are more elongated in the middle which is in contrast with what was observed with SS 316.

It should be noted here that the size of the smaller pillar in scan 2 (for IN 718 build) was 200 μm instead of 500 μm and was highly compressed by the material above and underneath as shown in Figure 4.9a.

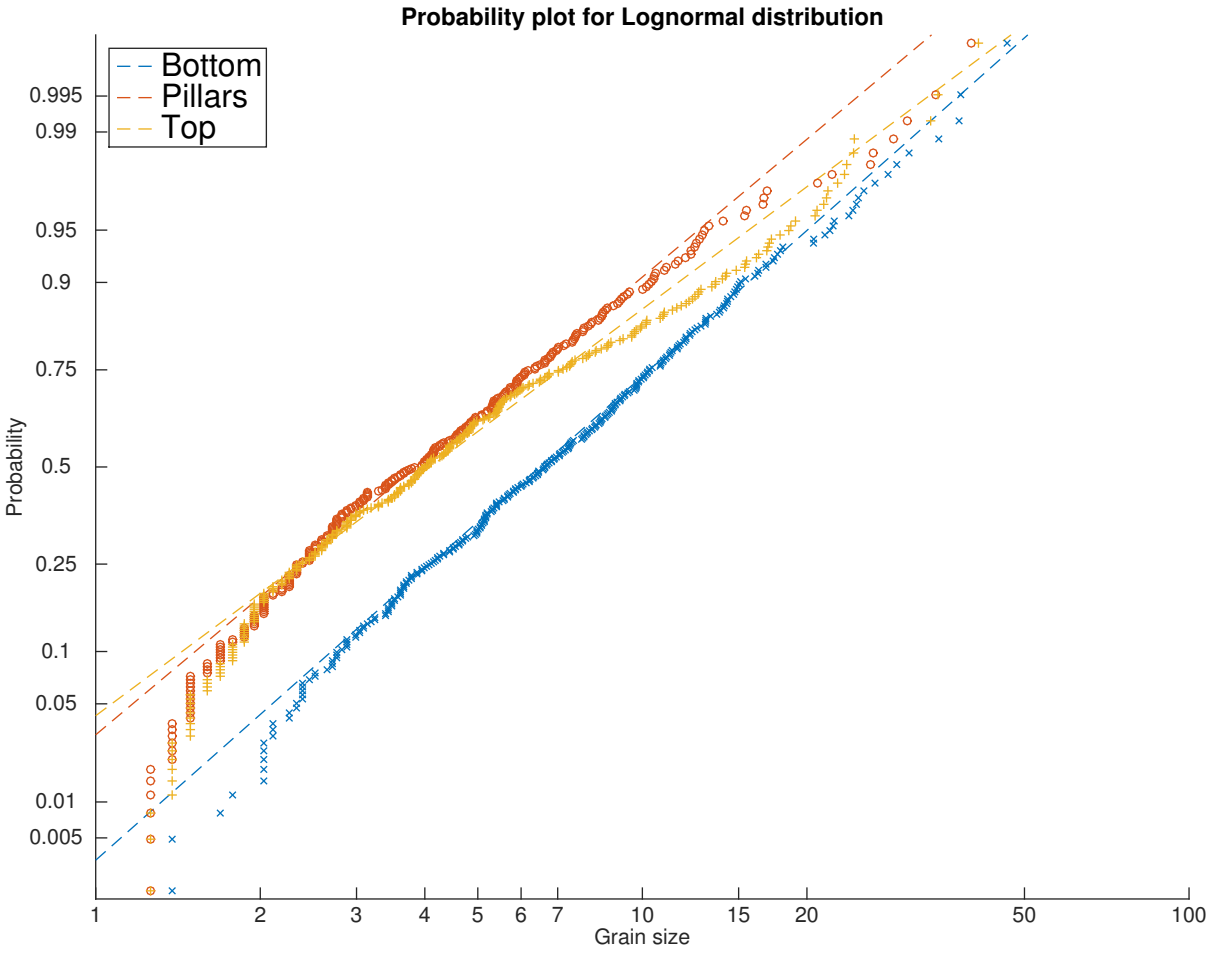

Figure 4.20: Grain size distribution for scan 1 (top), scan 2 (middle) and scan 3 (bottom) for IN 718 heat exchanger.

4.9.2.2 Twin fraction

Nickel-chromium superalloys, in general, have a large length fraction of $\Sigma 3$ twin boundaries. $\Sigma 3$ twin boundaries have 60° rotation about the $\langle 001 \rangle$ axis. OIM analysis software was used to compute the $\Sigma 3$ twin boundaries in as built IN 718 microstructure. Stein et al. [118] reported that the length fraction of $\Sigma 3$ boundaries make up 40% of all boundaries in LSHR low solvus high refractory (LSHR) nickel superalloy. And numerous studies including his have shown that these boundaries act as a site of fatigue crack

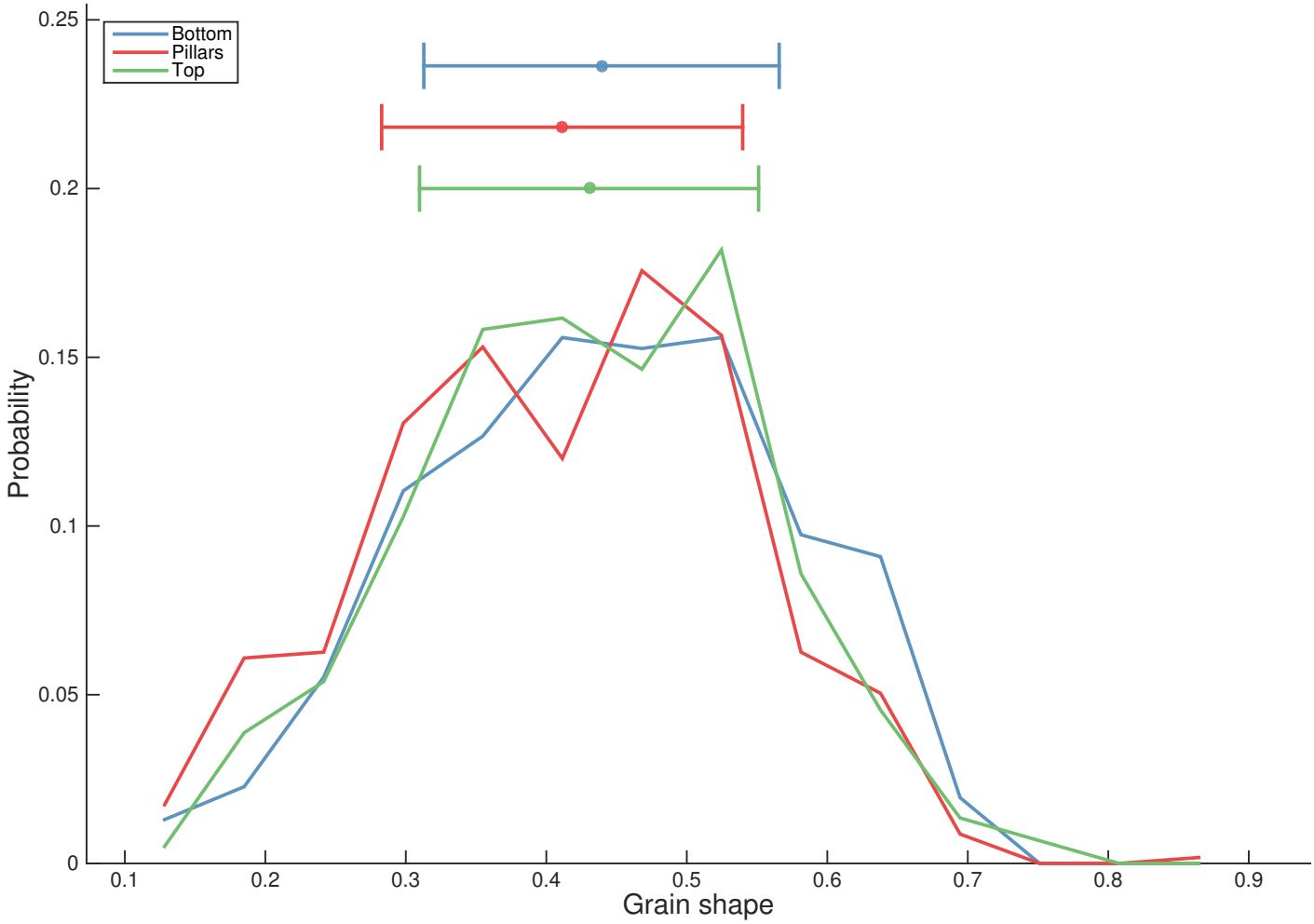

Figure 4.21: Grain shape distribution for three scans at three different build heights.

initiation [118]. Although 3D printed materials have a considerable porosity density, fatigue crack initiation at twin boundaries is always a concern.

From our calculation, the fraction of Σ3 twin boundaries in laser 3D printed Inconel 718 was less than 0.5%, as shown in the Table 4.1. This value is almost negligible considering the fraction of Σ3 boundaries found in other wrought or cast IN 718.

	Fraction of Σ3 boundaries
Top	0.49%
Pillars	0.49%
Bottom	0.2%

Table 4.1: Fraction of Σ3 twin boundaries at three different build heights for IN 718.

4.9.2.3 Porosity

Additively manufactured metals have a considerable number density of defects or porosity. This is intrinsic to the process as powder metal and laser melting is used to make the parts. Pores that are formed during the process act as a site of failure and thus are very detrimental, especially the ones near the surface. Different types of porosity that are observed are:

1. Lack of fusion/incomplete melting
2. Keyhole porosity
3. Gas pores

Lack or fusion, or incomplete melting, is seen if the laser energy is insufficient to melt all the powder and if there are unmelted powder particles. They can be generally identified by their irregular shapes [119, 120] Keyhole pores are produced during rapid solidification of metal, where deep and steep melt pool is formed without completely filling in the gaps with molten metal. Generally they are over 100 μm in size and have a characteristic "keyhole" shape with having wider upper head and pointy base. They tend to form at higher power. [121]. Gas pores are round, spherical pores formed because of trapped gas that formed bubbles and are less than 100 μm. A possible source of gas

pores is from the Argon gas used for making the powders [120, 79].

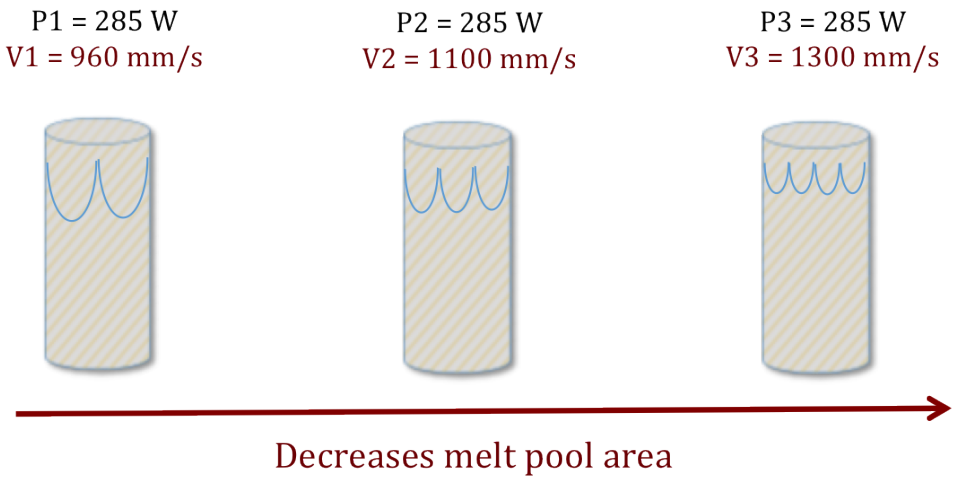

Figure 4.22: Schematics of decrease of melt pool area with an increase in laser velocity.

As shown in Figure 4.22, three different power and velocity combinations were tested. Power was kept constant but velocity was increased gradually. The idea behind this was to see if a decrease in melt pool area with increase in velocity would help print finer ($<$200 μm) features. As shown by the black horizontal line in Figure 4.6, all three velocities that were chosen were approximately from the 0.0101 mm^2 melt pool area or the standard melt pool region. Although, as shown in Figure 4.8, changing the process condition (PV combinations) did not result in improvement in part quality or in-built of smaller features, especially for larger aspect ratio, it was interesting to see how the 3D porosity content varied with the change in process parameters for Inconel 718.

	Vol. Scanned (mm^3)	Total no. of pores	Pore diameter range (μm)	Avg. equivalent diameter (μm)	Volumetric porosity %
P1V1	0.7841	1121	23.33-1.6	4.39	0.019
P2V2	0.8725	2210	31.433 to 1.6	4.613	0.051
P3V3	0.8463	2373	83.21 to 3.45	10.24	0.074

Table 4.2: Pore statistics for three different process conditions for bulk IN 718.

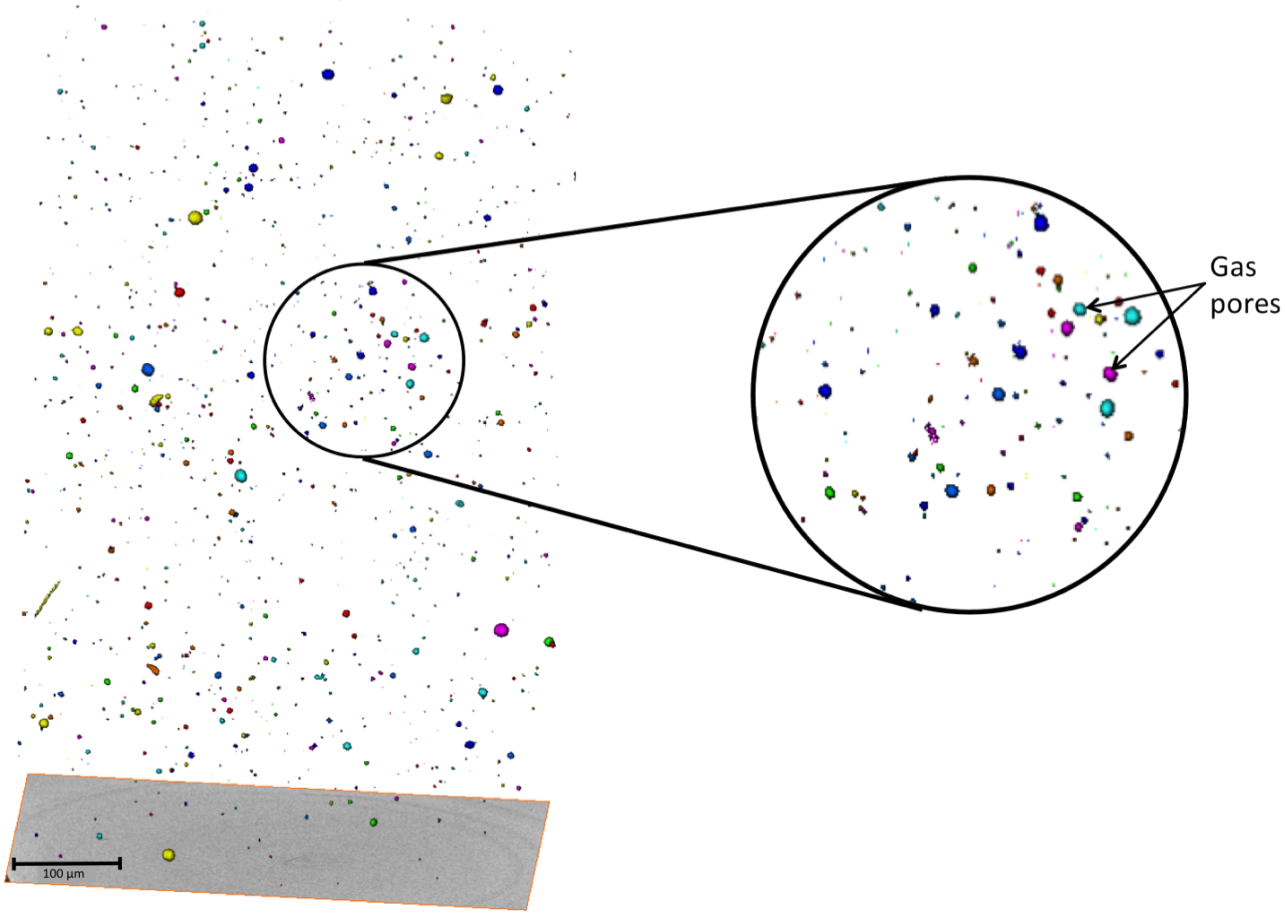

Figure 4.23: X-ray CT 3D-porosity result for P1V1 input parameters. Most of the pores observed are gas induced pores.

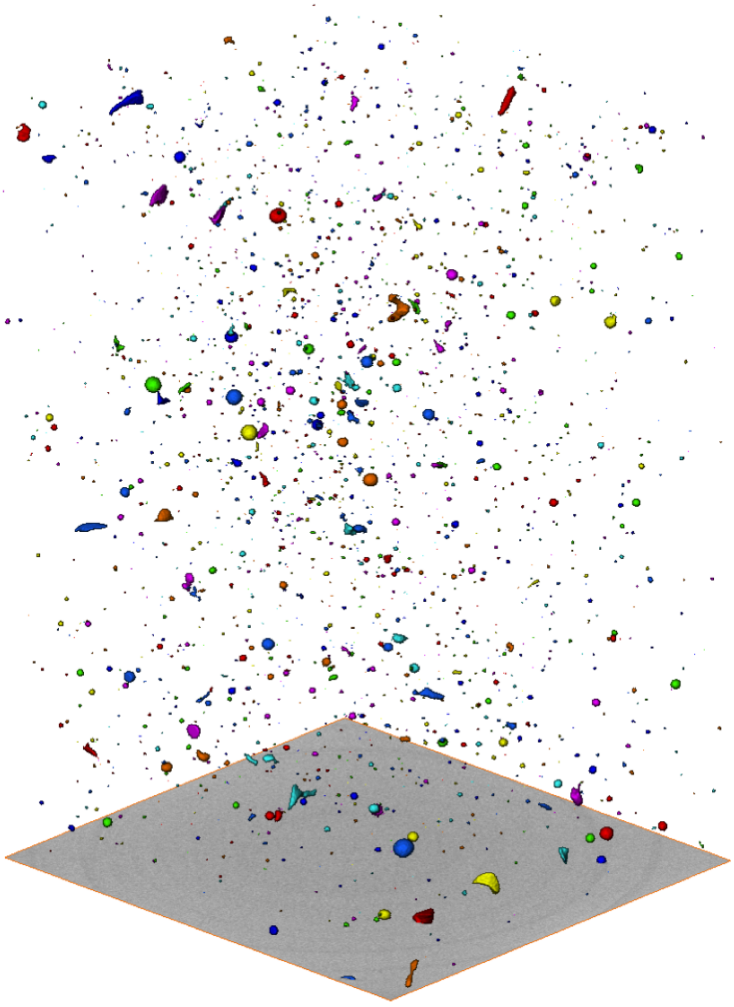

Figure 4.24: X-ray CT 3D-porosity result for P2V2 input parameters. Few lack of fusion pores are starting to form. The scale bar is same as Fig. 4.23.

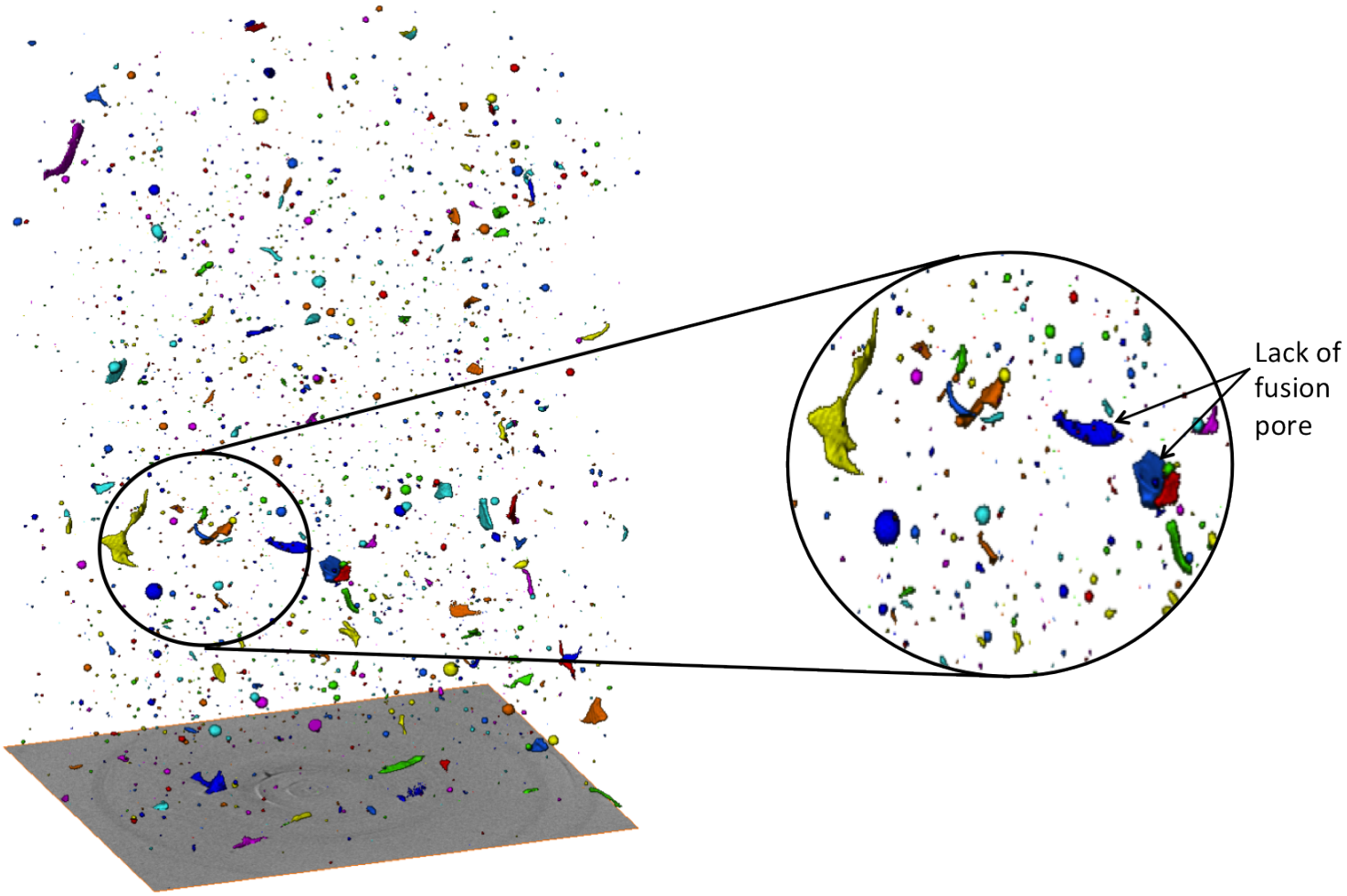

Figure 4.25: X-ray CT 3D-porosity result for P3V3 input parameters. Most of the pores observed are a combination of gas induced and lack of fusion pores. The scale bar is same as Fig. 4.23.

The results of the 3-dimensional porosity measurement from the x-ray micro CT experiment is shown in the Table 4.2. Qualitative results of synchrotron porosity data are shown in the Figure 4.23, Figure 4.24 and 4.25 for three different process parameters respectively. The minimum sized feature resolved was 0.65 μm. For V = 960 mm/s, there are mostly spherical pores, which means that they are mostly gas pores. For V= 1100 mm/s, there is a combination of gas and lack of fusion pores characterized by uneven shapes of the pores. And for V = 1300 mm/s large number of lack of fusion pores can

be observed, as highlighted in Figure 4.25. The higher the velocity of the laser beam the less time the powder gets to melt and fuse together, leading to the lack of fusion pores. Statistically, as shown in the Table 4.2, average equivalent pore diameter is increasing with an increase in velocity. Similarly, the volumetric porosity is increasing consecutively.

Another thing to note here is the faint ring marks on the base of thfe scans. This is one of the most common artifacts in x-ray CT scans introduced due to the detection calibration error [122]. It requires effort in post processing and cleanup to get rid of these marks. It is important to mention that each CT scan takes about 2 mins, however, reconstruction could take about 2 hrs for $\sim$30 GB scan file. Visualizing 3-dimensional pores in Avizo after cleanups and thresholding could take $\sim$2-3 hrs for each scan. Depending on the scan size and experience of working with each of these softwares could increase or decrease the processing time.

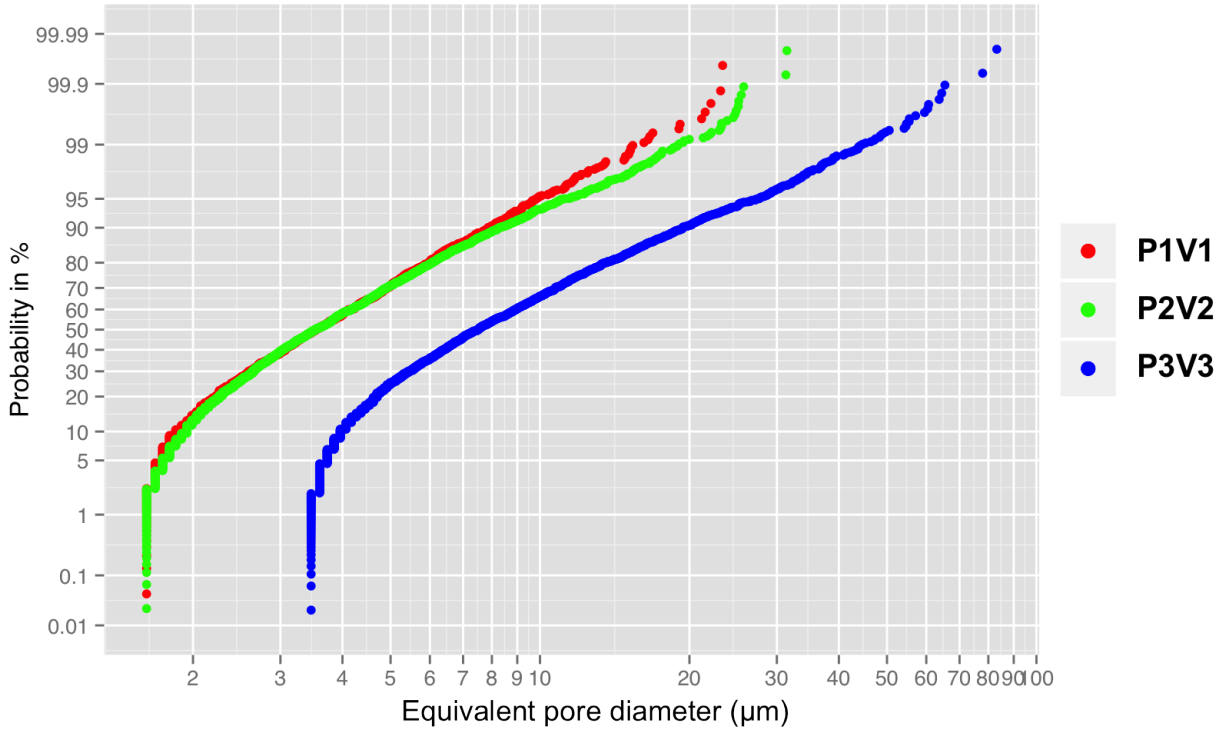

Figure 4.26: Cumulative pore size probability distribution for three input conditions. Increase in velocity results in increase in average equivalent pore diameter.

The cumulative pore size distribution of three PV combination is drawn in Figure 4.26. The overall volumetric porosity for all three PV combination is less than 1% which is not significant enough to affect the mechanical properties. However, the distribution shows that there are pores as big as 100 μm which could be detrimental to the part especially if they fall on the surface or at thin film features. It is evident from the distribution plot that with the increase in velocity, mean pore size diameter increases. There is an upper and lower tail deviation for all three data sets. In all three cases, there is a large spread in upper tail. Few points in the upper tail are significantly higher than the others. All this suggest that the nominal speed (P1V1) give the lowest porosity or highest density material and is the optimal parameter to use in fabrication of IN 718 using AM.

	Vol.Scanned (mm^3)	Total no. of pores	Pore diameter range (μm)	Avg. equivalent diameter (μm)	Volumetric porosity %
P1V1	0.143	203	54.6-1.6	7.2	0.34
P2V2	0.143	205	49.2-1.6	6.19	0.17
P3V3	0.143	204	46.4-1.6	5.33	0.12

Table 4.3: Pore statistics for three different process conditions for small pillar IN 718.

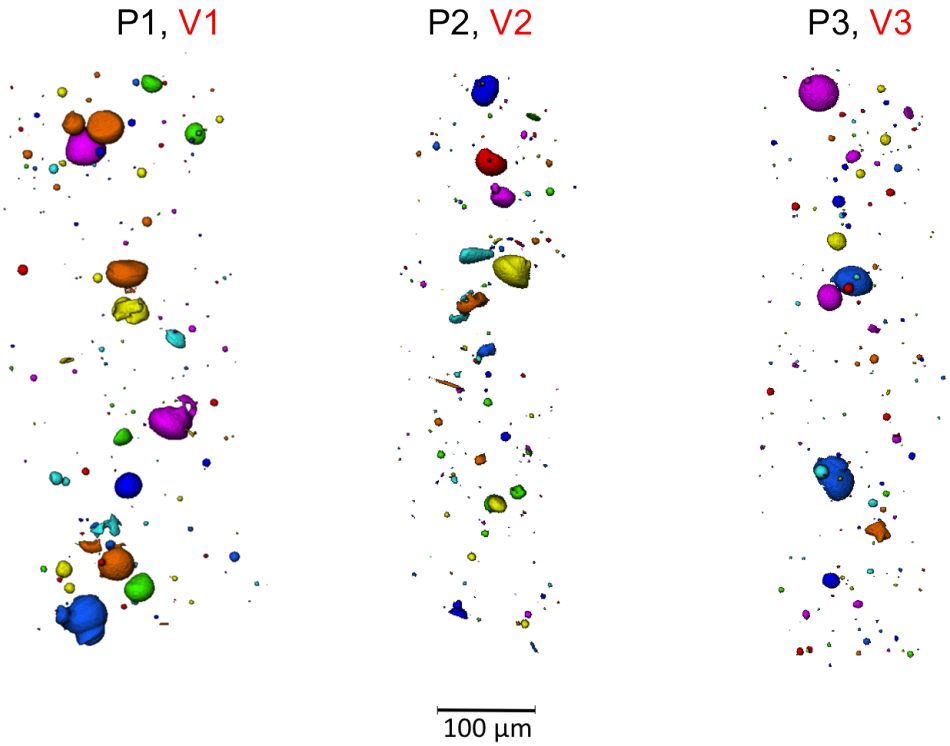

Figure 4.27: X-ray CT result for 200 μm pillars for all three PV combinations.

Similarly, x-ray CT was also done for smaller pillars for the same consecutive PV combination. In contrast to what was seen in the bulk material earlier, in 200 μm features, P1V1 has the largest average pore diameter and volumetric porosity, as shown in Table 4.3 and Figure 4.27. P1V1 is also the nominal speed given by EOS for IN 718. The total number density of pores for all three combinations are almost identical. The cumulative distributions in Figure 4.28 show that for all three data sets the "spread out"

looks almost the same. Above 15 μm, there are fewer pores as compared to below 15 μm. Also, the pores in the pillars are intermediate in size between the worst and best of the bulk builds (Figure 4.26).

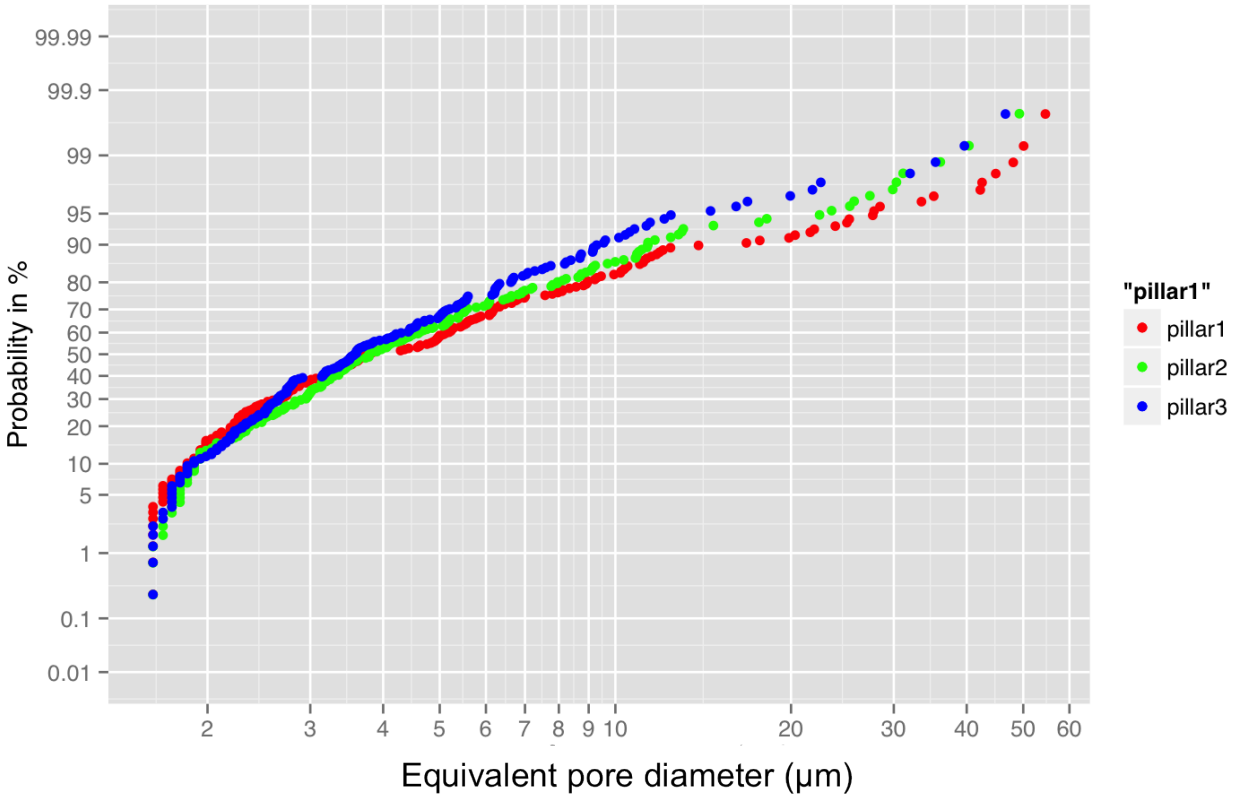

Figure 4.28: Cumulative pore size probability distribution for μm pillars for all three input conditions.

4.9.2.4 Macro-hardness mechanical testing

Macro-hardness mechanical testing was done using HRC. The main findings of the testing are presented in Table 4.4. At each build height, 5 hardness data points were collected and the average of those data point calculated. As shown in the table, the microstructure on the top has lower hardness compared to the one the bottom of the HX. This directly correlates to the grain size values calculated in Figure 4.17. The

bottom part of the HX has a larger grain size thus the lower hardness value compared to the top section. These values are similar to the hardness values reported by Tian et al. where depending on the cross section, hardness went from 25 to 45 [123]. IN 718 is a precipitate hardening alloy so with heat treatment of IN 718 this value is expected to go up.

	Hardness (HRC)
Top	28.46
Pillars	30.34
Bottom	25.52

Table 4.4: Hardness values at three different build heights for as-built IN 718 heat exchangers.

4.9.3 Heat treated Inconel 718

Two heat treatment procedures used to homogenize IN 718 microstructure are:
1. Recipe 1: Standard procedure recommended by EOS and that is in compliance with AMS 5662 or industrial standard heat treatment for wrought IN 718 [100] is solution anneal at 980° C (1800° F) for 1 hours, air cool. Aging/precipitation treatment: hold at 720° C (1330° F) 8 hours, furnace cool to 620° C (1150° F) in 2 hours, hold at 620° C (1150° F) 8 hours, air cool.

2. Recipe 2: Another slightly different heat treatment that was used is (968° C for 1.5 h), aged (718° C for 8 h to 612° C for 8 h and then cooled below 150° C).

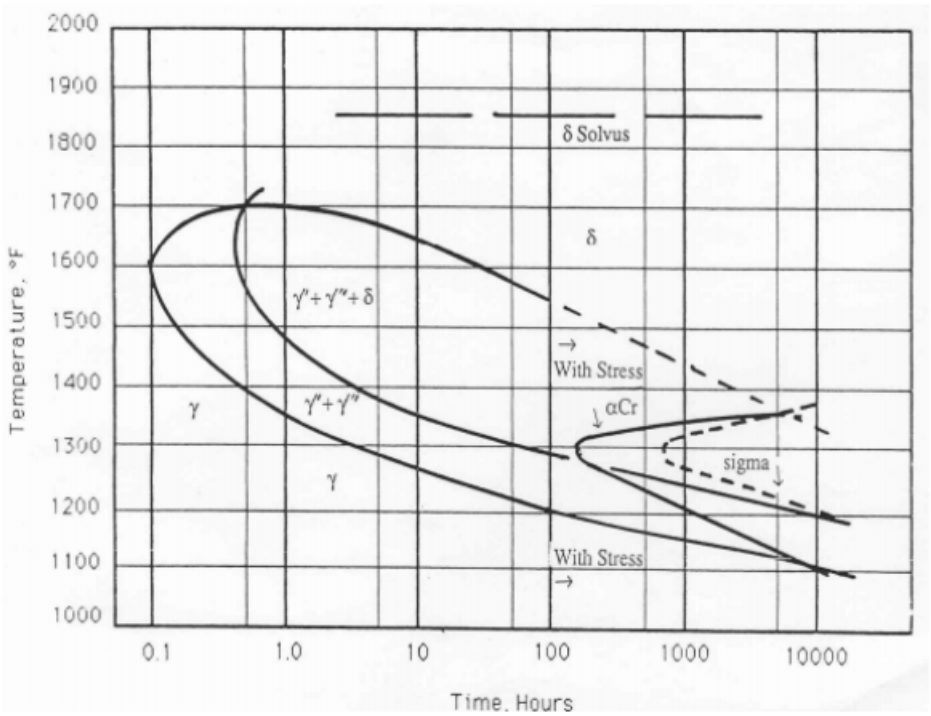

Figure 4.29: Time temperature transformation (TTT) diagram for alloy 718. [124]

In as-built IN 718, due to the rapid solidification, the cooling rate is very high i.e. million degree/sec. Therefore, no precipitate is expected to form. There have been reports of γ" precipitate forming that had a length scale of around 20 nm and could only be resolved using high resolution transmission electron microscopy (HRTEM) [123]. As shown in Figure 4.29, only γ-phase of IN 718 which is Ni matrix, with alloying element is expected.

After heat treatment, however, different (γ', γ" and δ) phases start to precipitate. The first step of heat treatment (HT) is solution anneal at 980° C which dissolves "segregated particles and strengthening phases into the matrix" incurred during solidification [100]. The second step is the aging treatment which results in the precipitation of different phases (γ' and γ") into the matrix, which strengthens the material. "The presence of the residual stress will result in an unstable state for the as-fabricated samples, once having enough thermal activation energy recovery, recrystallization and

grain growth will occur" [100]. The goal of IN718 post-processing is to produce a homogenous, precipitate hardened microstructure. Internal porosity may be removed by hot isostatic pressing (HIP).

4.9.3.1 Grain growth

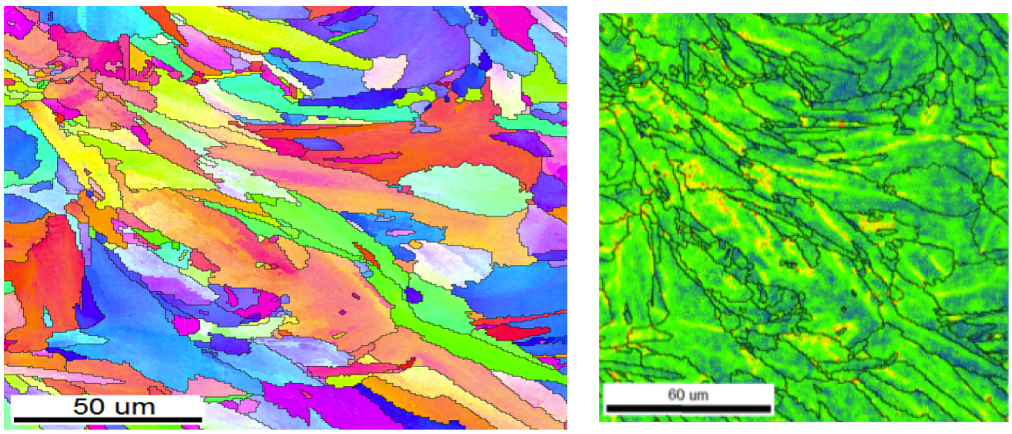

(a) (b) Average KAM:1.28

Figure 4.30: a) IPF b) KAM map after heat treatment recipe 1.

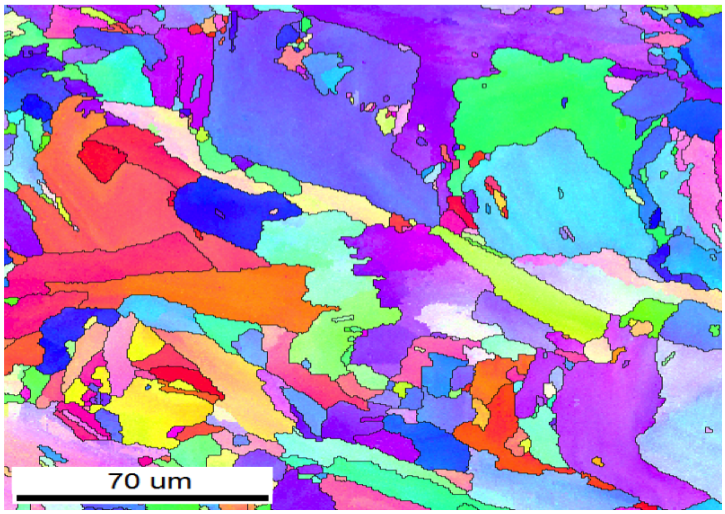

Figure 4.31: EBSD map after heat treatment recipe 2.

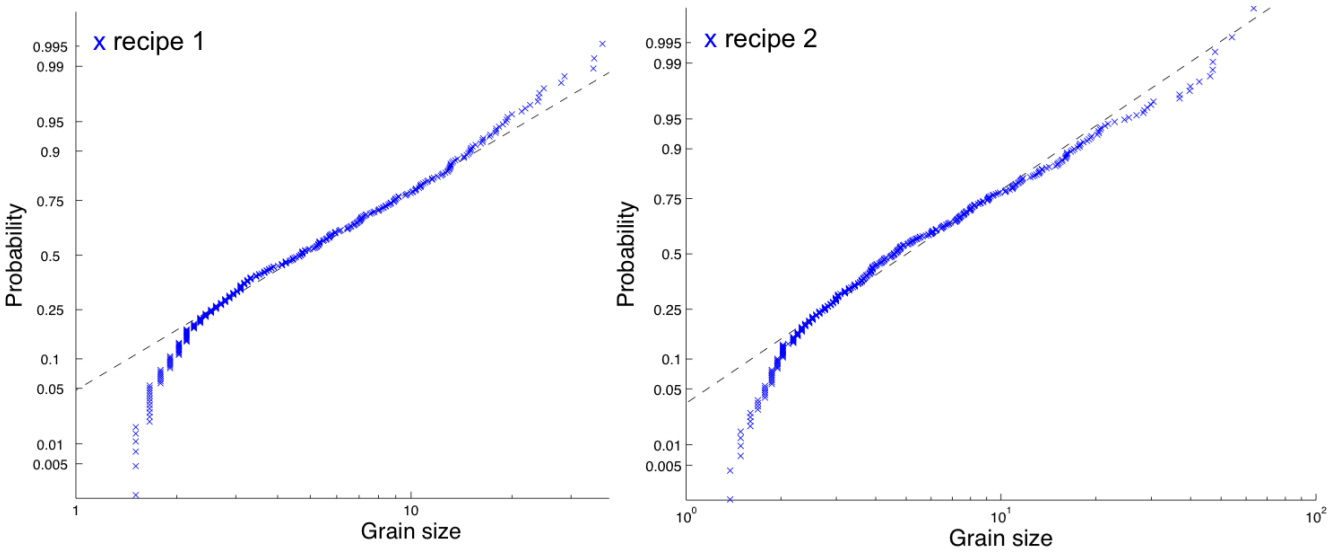

Figure 4.32: Grain size distribution of EBSD maps after two heat treatments.

As shown in Figure 4.30 - Figure 4.32, after heat treatment, the grains have grown larger. Grain size has increased from 4 μm to 8 μm. Average KAM value went down from 1.41 to 1.28, which means that the heat treated microstrucuture have less orientation graidents in them, compared to the as-built strucuture. However, there is still a significant amount of orientation gradients. This indicates that the grains did not go through full recrystallization. Dinda et al. mentioned that at 1000° C there is a little indication of recrystallization, at 1100° C it is mostly a combination of recrystallized and dendritic microstructure and at 1200° C grains were full recrystallized with a significant grain growth [87]. Similarly, Smith et al. [90] also reported a microstructure with significant orientation gradients after heat treatment at 954° C. All this indicates a more detailed heat treatment analysis, possibly with different heat treatment temperatures is required as it is clear that the conventional industrial standard HT for wrought or cast IN 718 is not optimum for 3D printed materials.

	Hardness (HRC)
Top	41.2
Pillars	39.03
Bottom	35.7

Table 4.5: Hardness values at three different build heights for heat treated IN 718 heat exchangers.

4.9.3.2 Hardness

Hardness testing was also conducted after heat treatment and the Table 4.5 summarizes the results. Hardness on average went up from 28 to 38 HRC which is expected of Inconel 718 after heat treatment owing to the appearance of precipitates. This compares very well to wrought Inconel 718 which has a hardness of around 41Rc after heat treatment [125].

4.9.3.3 Twin boundaries

The formation of annealing twin boundaries is one of the common phenomenon with superalloys. Annealing twin density increases with recrystallization [86] and primary recrystallization introduces high densities of twin into fcc metals [126]. However in this study, it was seen that even after heat treatment, the fraction of $\Sigma 3$ twin boundaries were less than 0.5%. This is consistent with what was seen earlier i.e. the printed IN 718 did not go through recrsytallization, hence, no twin formation. Twin boundaries in a heat treated EBSD map are shown in Figure 4.33. This is a very interesting finding as fatigue cracks generally occur at twin boundaries [118] and with laser printing it might be possible to create a twin-free superalloy.

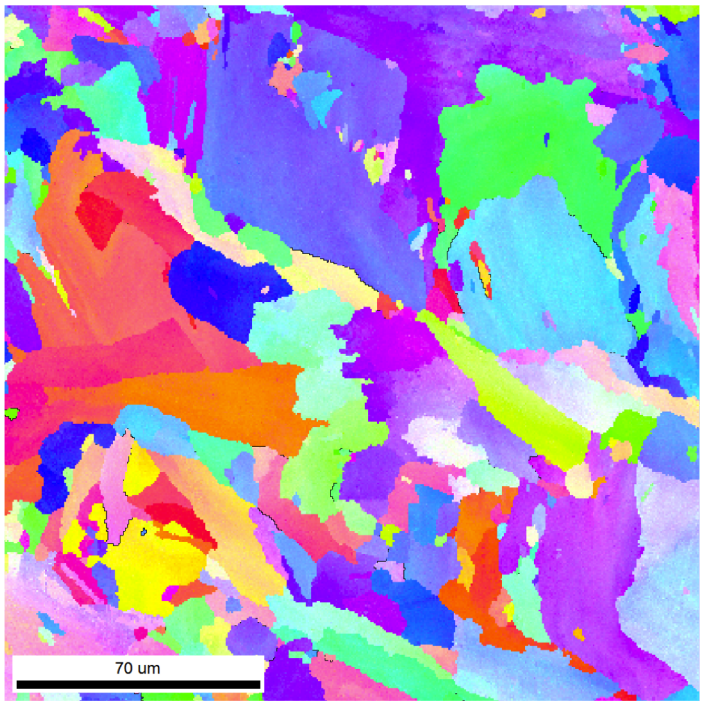

Figure 4.33: Grain map showing twin boundaries in black for heat treated 3D printed IN 718.

4.9.3.4 Micro-pillar compression testing

Micro-pillar compression testing was done in heat treated samples to capture micro or the grain level properties. Due to the very small grain size in as-printed samples, this test was not feasible. As shown in Figure 4.34, an EBSD map was taken to compute the grain orientation and tentative location of each micro pillar before the compression. The number markings show where the pillars were made. The list of orientations for each micro-pillar is shown in Table 4.6. The dimensions of each pillar are 4.3 x 10 μm.

This is a more accurate way to analyze strength in material. Macro-hardness gives us a bulk grain property but is sensitive to external factors such as surface roughness, indenter tip, etc. Micropillar compression is an effective technique that provides local stress-strain properties. The effect of slight variation in orientation, pores, grain boundary could be captured using this technique.

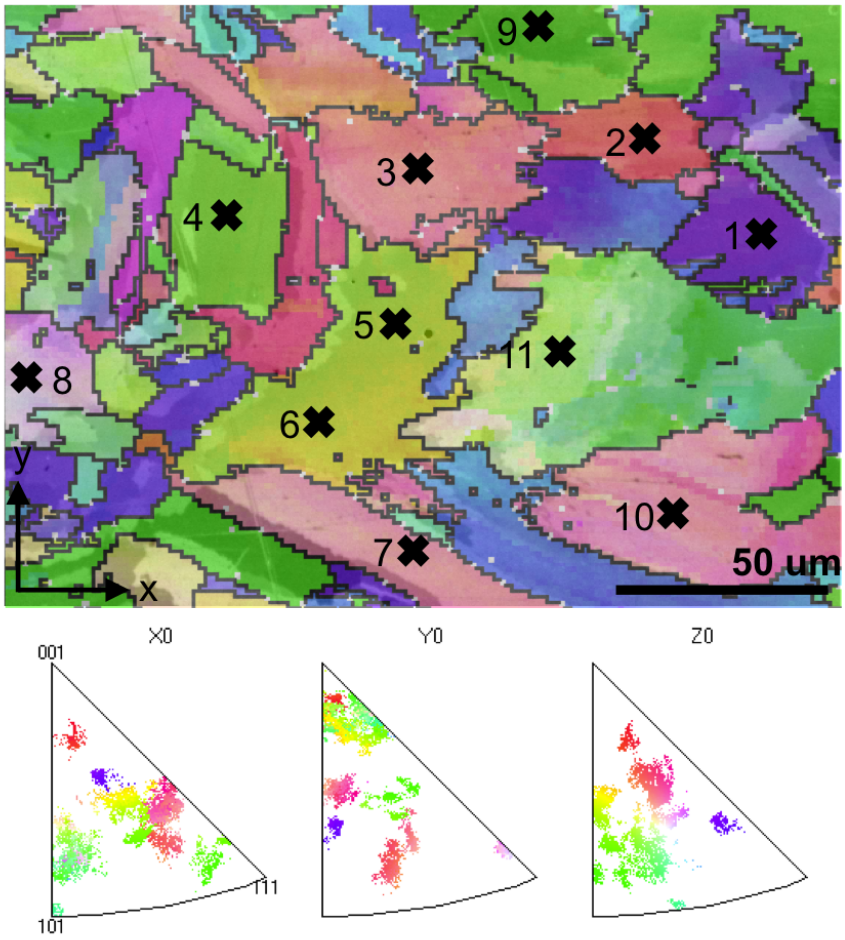

Figure 4.34: EBSD scan and markings of region of where and the grains where micro pillar testing was done.

SEM images of all 11 pillars before compression are shown in Figure 4.35. Micropillars such as 1 and 6 clearly have pores in them. Similarly, pillars such as 4 and 11 have interfaces in them, suggested by the color contrast of bands.

SEM images of 11 pillars after compression are shown in Figure 4.36. The slip bands and deformed regions can be clearly seen in the figure. Qualitatively, 1-6 and 9-11 have double slip bands. Micropillar 8 may have double slip and 7 exhibits single slip. When magnified any of these pillars, disc like plates could be seen. For example, the tip of the

Micropillar	IPF-Z (hkl)
1	2 3 5
2	1 1 6
3	2 1 5
4	0 3 5
5	1 0 2
6	1 0 2
7	1 2 5
8	2 1 4
9	5 1 6
10	2 1 5
11	1 4 6

Table 4.6: Micropillars and their corresponding orientations.

pillar AM_HT2_2 in Figure 4.35 show sub-micron to micron scale platelets, as shown in Figure 4.37. The typical morphology of carbides is black, irregular patches randomly distributed throughout the surface. According to the TTT diagram in Figure 4.29, after aging treatment, δ, γ' and γ" are expected to precipitate. Typically,

i δ precipitates form at the grain boundaries, as they tend to improve materials creep property by preventing grain boundary sliding. [82] δ precipitate is needle shaped ranging in length from 1-8 μm.;

ii γ' is a disc-like precipitate with 10 -40 nm size range, and

iii γ" are large discs with ~ 0.3 μm in diameter. [86, 90]

These precipitates are coherent with the austenitic (γ) matrix. At a high temperature, γ' dissolves into δ and γ". From the size, morphology and the fact they do not lie

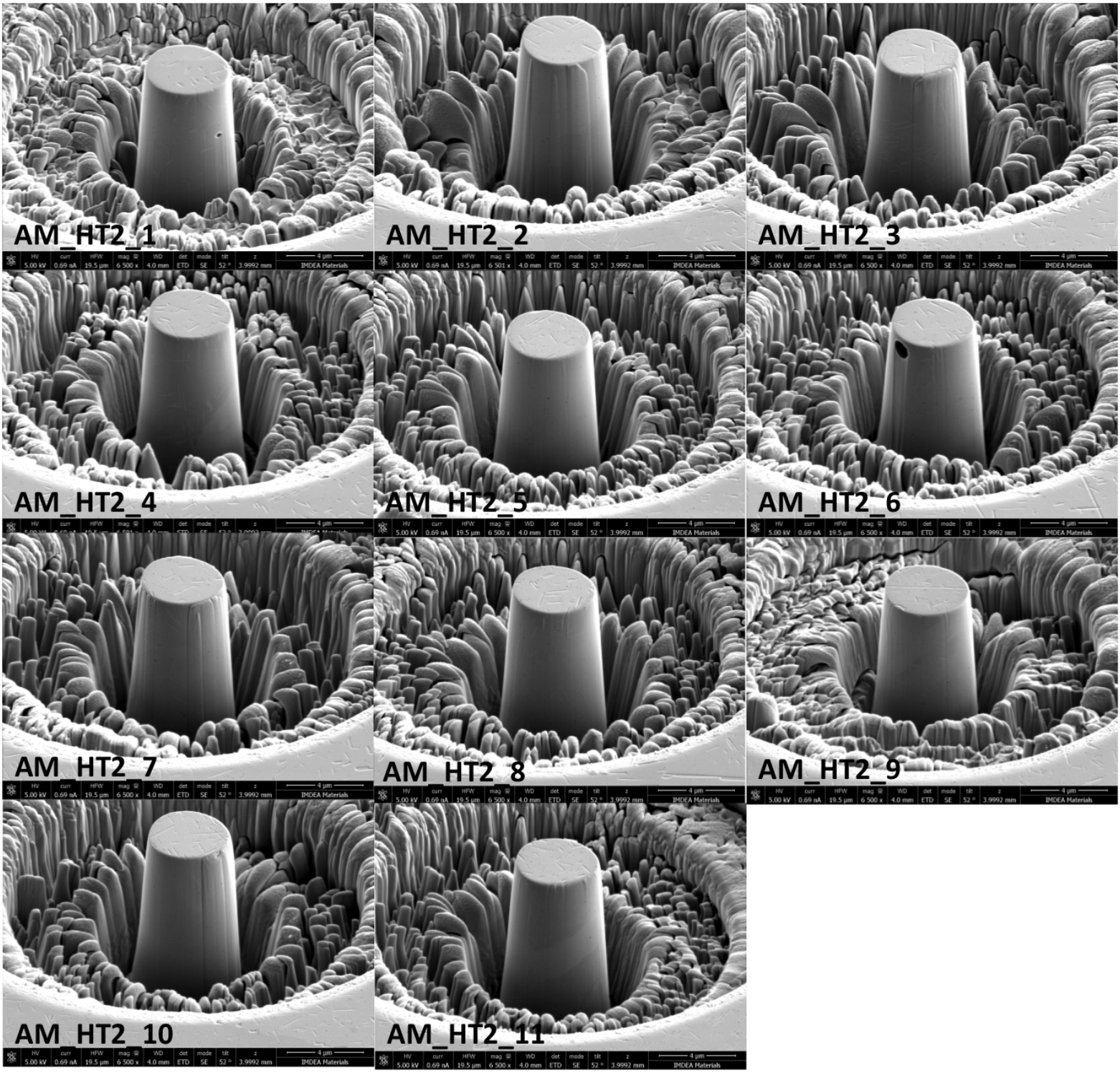

Figure 4.35: SEM images of micropillars before compression.

in the grain boundary, the precipitates seen in AM_HT2_2 in Figure 4.37 is thought to be γ". However, for the accurate assessment and detailed analysis on the precipitates,

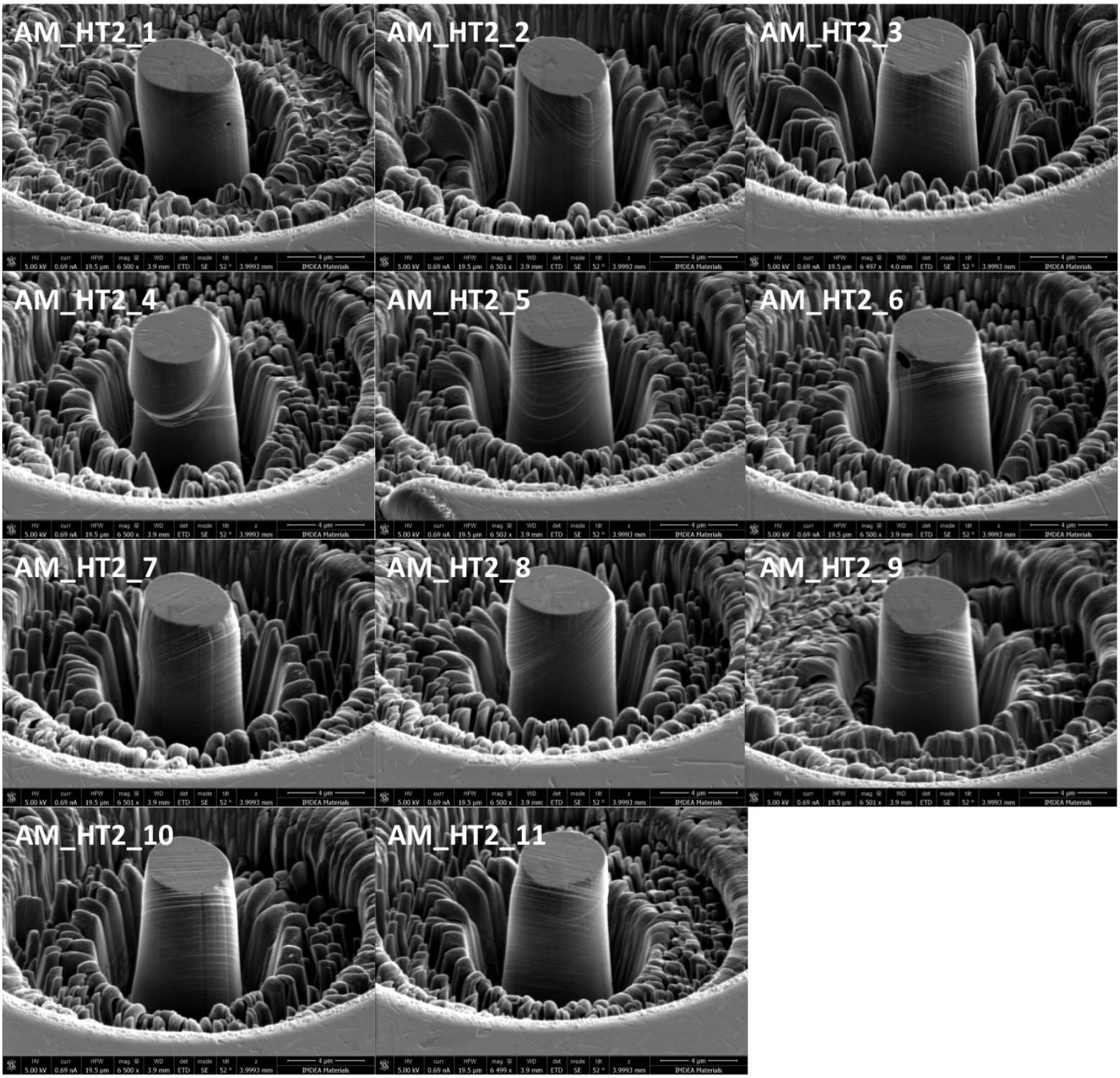

Figure 4.36: SEM images of micropillars after compression.

TEM studies are recommended.

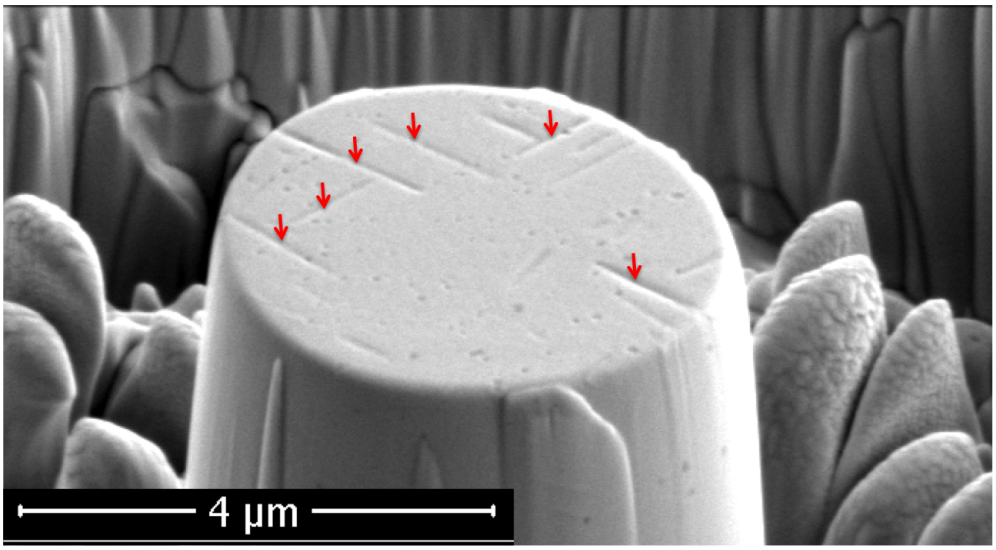

Figure 4.37: Magnified SEM image of AM_HT2_2 micropillar showing precipitates with red arrows.

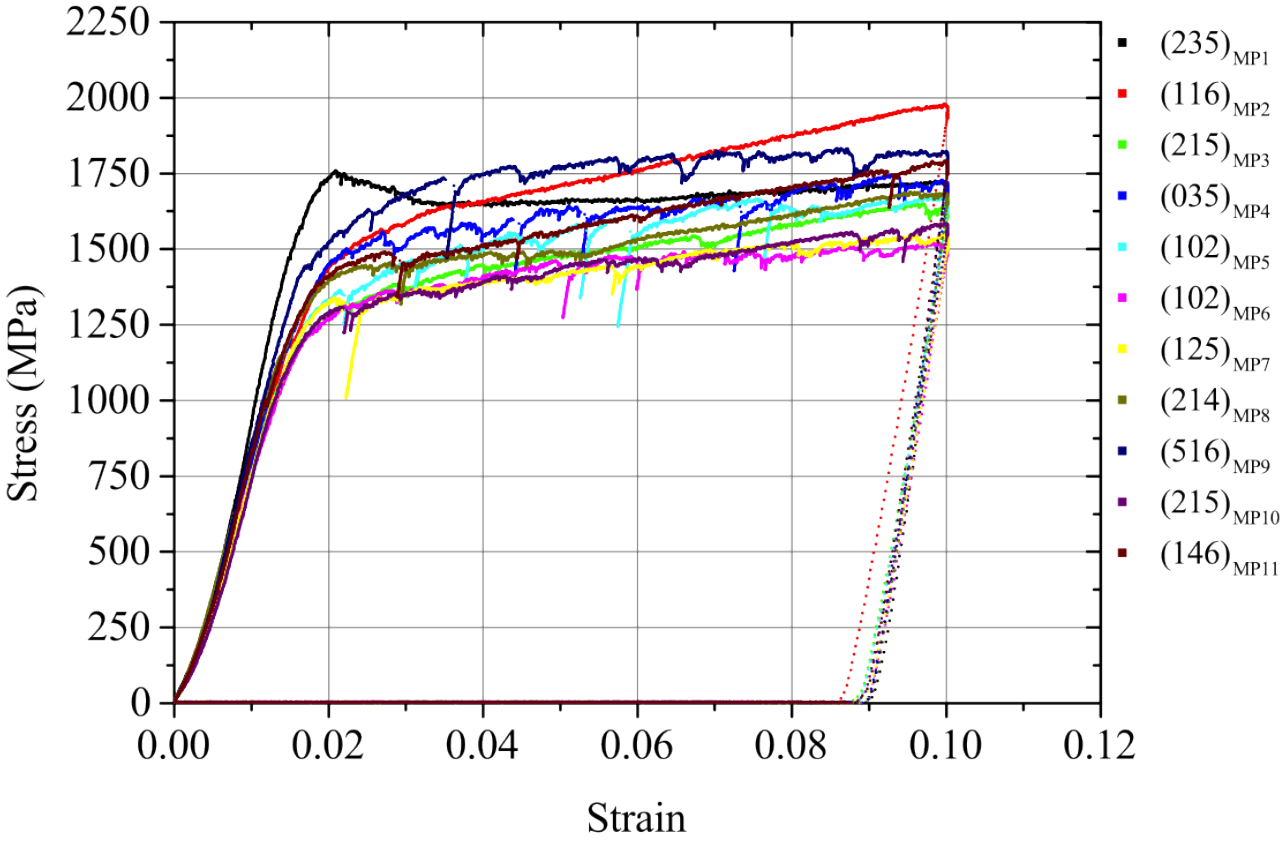

Figure 4.38: Stress strain graphs for all 11 micropillars.

The combined stress-strain graphs for all 11 micropillars are shown in Figure 4.38. As shown in the graph and table 4.8, the yield stress values locally vary from 860 to 1473 MPa within a small area i.e. 250μm x 250μm. This is a substantial variation considering how small the scan area is. The strength depends on the orientation of the grain, i.e. whether it is a soft or a hard grain. Comparing the IPF traingle in Figure 4.34 Z0 with Taylor factor values, it can be deduced that micropillars 1, 4, 9, and 11 are the hardest grain and micropillars 3, 7, 10 are the softest grains. Despite having a pore, pillar 1 has the highest yield stress value although there is a dip in the strength which could be due to the pore. Pillars 5 and 6, which are from the same grain have ≈100 MPa of difference, which could be attributed to the fact that pillar 6 has a pore in it. However, it is surprising that despite having a large pore, pillar 6 has relatively higher yield stress, which is rather counterintuitive. Micropillar 8 which is a softer grain, has the second highest yield strength even compared to 11 which is a harder grain plus has a grain boundary.

An important point to note here the yield strength for these heat treated IN 718 micro pillar. The values are very comparable and even higher [127] than conventionally manufactured IN 718.

The next step was to see if the pillars yielded due to slip or double slip for which Schmid and Taylor factor were calculated. The equation used to calculate the Schmid factor is:

$$m = cos\ \phi.cos\ \lambda \tag{4.3}$$

where, ϕ is the angle between the normal to the slip plane and applied force (or crystal direction), and λ is the angle between the slip direction and applied force (or crystal direction). Schematics of a slip system in a single crystal is shown in Figure 4.39

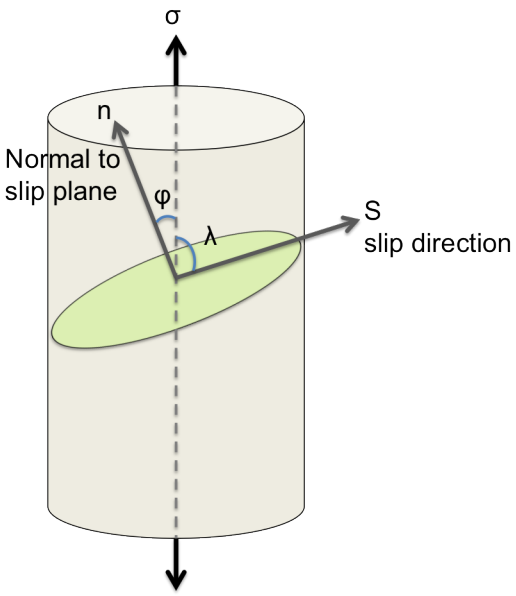

Figure 4.39: Slip system in a single crystal lattice.

The detailed set of calculations for each of the orientations using all 12 slip system are shown in Table 4.7. The maximum Schmid factor for each orientation is highlighted in red. The slip system with the highest Schmid factor is the active slip system. In a given crystal, slip begins when the resolved shear stress acting on a slip system reaches the critical resolved shear stress.

Similarly the Taylor factor is also calculated. Table 4.8 lists orientation, yield stress, Schmid factor and Tyalor factor for all the micropillars.

Yield stress vs. Taylor and Schmid factor were plotted in Figure 4.40 and Figure 4.41 to see if there was any correlation which could give an indication of whether the pillars failed due to single slip or multislip mode.

Systems	1	2	3	4	5	6	7	8	9	10
(111) [-101]	0.32	0.43	0.33	0.48	0.24	0.24	0.43	0.27	0.08	0.42
(111) [-110]	0.10	0	-0.11	0.29	-0.24	-0.24	0.11	-0.14	-0.32	0.25
(111) [0-11]	0.21	0.43	0.43	0.19	0.49	0.49	0.33	0.41	0.39	0.17
(-1-11) [011]	0	0.30	0.16	0.19	0.16	0.16	0.19	0.10	0	0.07
(-1-11) [-110]	0	0	-0.02	0.07	-0.08	-0.08	0.03	-0.02	0	0.02
(-1-11) [101]	0	0.30	0.19	0.12	0.24	0.24	0.16	0.12	0	0.05
(-111) [101]	0.45	0.45	0.38	0.48	0.24	0.24	0.49	0.35	0.14	0.49
(-111) [110]	0.32	0.13	0.16	0.29	0.08	0.08	0.24	0.17	0.08	0.35
(-111) [0-11]	0.13	0.32	0.22	0.19	0.16	0.16	0.24	0.17	0.07	0.14
(1-11) [011]	0.34	0.45	0.49	0.19	0.49	0.49	0.38	0.49	0.46	0.23
(1-11) [110]	0.21	0.13	0.24	0.07	0.24	0.24	0.16	0.29	0.40	0.11
(1-11) [-101]	0.13	0.32	0.24	0.12	0.24	0.24	0.22	0.19	0.07	0.11

Table 4.7: Schmid factor calculation for each orientation with 12 slip systems.

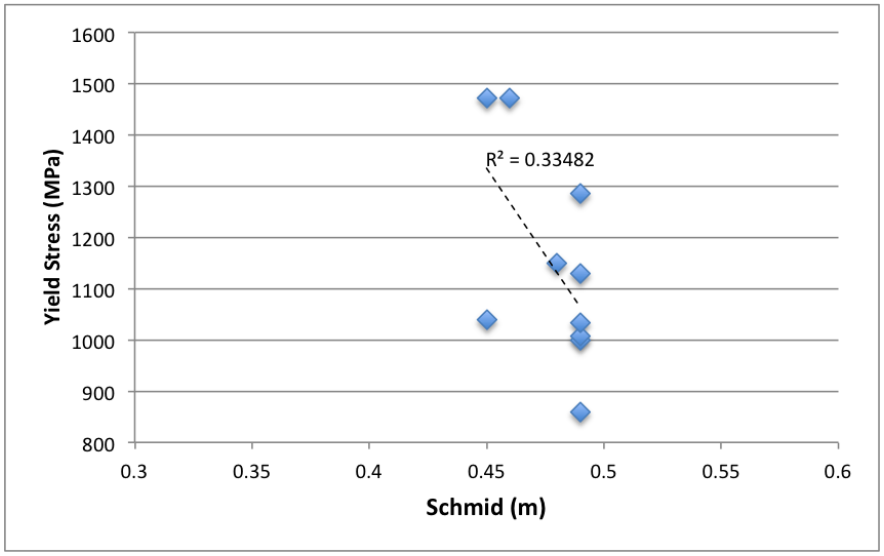

Figure 4.40: Yield Stress vs. Schmid factor, showing lack of correlation.

Micropillar	Orientation	Yield stress	Schmid factor	Taylor factor
1	2 3 5	1472	0.45	3.014
2	1 1 6	1039	0.45	2.288
3	2 1 5	1000	0.49	2.756
4	0 3 5	1149	0.48	3.242
5	1 0 2	1007	0.49	2.939
6	1 0 2	1130	0.49	2.939
7	1 2 5	860	0.49	2.756
8	2 1 4	1286	0.49	2.887
9	5 1 6	1473	0.46	3.556
10	2 1 5	980	0.49	2.756
11	1 4 6	1033	0.49	3.328

Table 4.8: Micropillar with their corresponding orientation, yield stress, and Schmid and Taylor calculation.

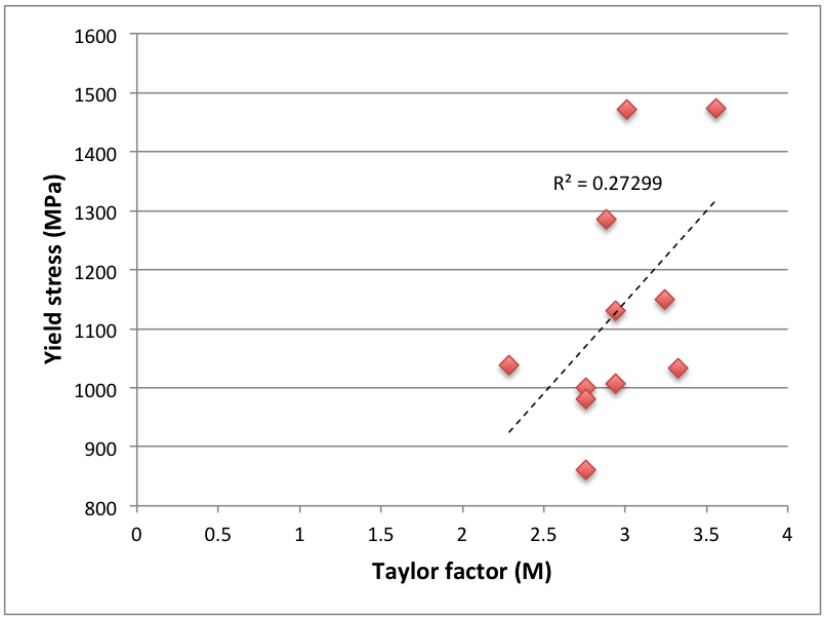

Figure 4.41: Yield Stress vs. Taylor factor, also showing lack of correlation.

However, as shown in the graphs, there was no particular trend observed. Yield stress does not have a strong correlation with neither Schmid or Taylor factor.

4.9.4 Summary & Discussion

Microstructural and mechanical properties of direct metal laser sintered 3D printed Inconel 718 were studied in this section. Compared to SS 316, grains in IN 718 were more equiaxed and randomly oriented. The mean grain size at the bottom of the grain was larger, leading to a low hardness, than the grains in the small pillar and bulk region. IN 718 is an age hardening alloy and the precipitation is expected after heat treatment. The hardness value and grain size increased significantly after heat treatment. However, full recrystallization was not observed. Orientation gradients were seen after heat treatment that signified partial or no recrystallization. The length fraction of $\Sigma 3$ twin boundaries was also very low, i.e. <0.5 % compared to conventionally manufactured IN 718. This leads to a very interesting question on why annealing twins do not form during recrystallization.

In as-built IN 718 microstructure, due to rapid solidification no precipitation is expected [86]. However, there are reports of very fine, $\sim$13 - 20 nm γ" precipitate [123], which can contribute to strength.

4.9.5 Hypothesis revisited

A monolithic mirochannel heat exchanger was fabricated using a laser based 3D printing technique with the nickel-chromium superalloy IN 718. Depending on the build height, design and process conditions, microstrucutral and mechanical properties such as grain size, shape, hardness, porosity and yield strength of printed material varied.

4.9.6 Future work

1. From the heat treatment results shown earlier, it was shown that full recrystallization did not happen. Rather there was a large orientation gradient in the microstructure. Dinda et al. reported that above 1200° C, for a DMLS IN 718, full recrystallization happens with significant grain growth. Therefore, in the future, it is recommended to do heat treatments at various temperatures, not following the standard heat treatment produces, and see how the microstructural features and mechanical properties change.

2. As mentioned earlier, the fraction of the $\Sigma 3$ twin boundaries was very small. It will be very interesting from a fatigue stand point to see if fatigue crack initiation starts at porosity or twin boundaries. Therefore, fatigue testing in these 3D printed samples should be conducted to see if fatigue crack initiation is different.

3. TEM study:

   The base plate in a laser based sintering system is heated to a relatively low temperature. Therefore, there is a high temperature gradient between the melt pool and the rest of the part. This leads to a rapid solidification. The cooling rate is on the order of 1 million°/ sec. According to the TTT diagram shown in Figure 4.29, when rapid solidification happens hardly any γ or γ" precipitate is expected. However, there are reports of precipitate forming at the nanoscale level. After heat treatment precipitates are expected to grow bigger or appear at the nanoscale to micron level. As mentioned earlier these precipitates govern the mechanical properties of Inconel 718. Therefore, it is important to understand where and how the precipitates form before and after the heat treatment. Considering the nano size scale of the precipitate HRTEM is recommended. HRTEM also could be used to study dislocation behavior and how it affects strength properties, similar to the

Cu-Nb study earlier.

4. Neutron characterization could be done to calculate the residual stress. This helps identify in which region in the printed part the stress is higher and how much of the stress can be relieved after heat treatment. For this x-ray at 6BM at APS is recommended because of the fine scale.

5. Solidification modeling:

   From a modeling perspective, the thermal profile of the melt pool could be calculated using a Rosenthal equation [98, 113]

$$T = T_o + \frac{Q_p}{2\pi R\kappa} exp\left[\frac{-\nu(\xi + R)}{2\alpha}\right] \tag{4.4}$$

   where, T is the local temperature, T_o is the plate temperature, Q_p is the laser beam power, $R = (\xi^2 + y^2 + z^2)^{1/2}$ is the radial distance from the beam position, κ is thermal conductivity, ν is the beam speed, ξ is the distance from the beam position along the travel direction and α is thermal diffusivity.

Chapter 5

Summary & Future directions

5.1 Summary & Conclusions

Microstructural and mechanical properties of different multilayered materials fabricated using some of unique techniques were studied in this thesis. The two main materials that were studied are Copper-Niobium nanolaminates and laser 3D printed IN 718. Both materials were uniquely fabricated and therefore possessed some distinct interface and microstructural properties. To analyze their properties, various tools and techniques such as EBSD, ASTAR^{TM} in TEM, data fitting, in-situ TEM compression and tension, x-ray CT, micro pillar compression tests were used.

In the first chapter, 18 nm individual thickness Copper-Niobium nanocomposite was analyzed after the material had been subjected to two different severe plastic deformation (SPD) methods. The first SPD performed was accumulated roll bonding and the second was high pressure torsion. The materials' response at extreme plastic strain was examined. ASTAR^{TM} was adopted in order to characterize the deformed nanolayer and to understand the orientation and texture behavior in detail. ASTAR^{TM} is an orientation mapping technique in TEM which has been applied to characterize ARB Cu-Nb in the

past, however, this is the first time this technique has been applied to study ARB followed by HPT material. Obviously, this means that the material is very highly deformed, with a high deformation gradient that required proper care to collect and index the pattern. With ASTAR^{TM}, it was observed that the texture developed during ARB was largely destabilized at 10.8 HPT. A significant orientation gradients within each layer and layer fragmentation were observed. Orientation development was random and isotropic except for the fully developed fold case. The interface boundaries were not clear as many folds and bends were seen. From the x-ray diffraction experiment shown by Ekiz et al. [15], these folds were characterized to have texture that were unlike the shear texture of Cu or Nb. There was no indication of shear banding either. However, it is important to realize that x-ray measurements give the bulk material texture and hence might have failed to capture the local fold properties. ASTAR^{TM} was crucial to measure local orientation and to characterize the fold microstructures. In this study, ODF for each different type of folds was drawn and compared to the ideal ODF for both Cu and Niobium. By analyzing the ODFs, we concluded that these folds are the result of shear deformation.

On a similar note, it was very important to analyze dislocation accumulation and movement in order to model the strength behavior of these nanolaminates. The strength in nanolamintes, similar to any other polycrystal material, follows Hall-Petch, where strength increases with decreasing layer thickness, until about 100 nm. From 100 nm to about 5 nm, a confined layer slip (CLS) model is popularly believed to govern the strength properties, where 1-2 dislocations are confined within each layer to form an Orowan bowing type controlling strength behavior at this thickness. However, there was enough evidence in the literature that indicated that there might be traces of dislocations in the interfaces. From the modeling study, it was found that the CLS equation did not predict the strength behavior accurately. It would either under or over predict the

strength behavior and therefore required additional terms to fit the data. Therefore, an alternative theory based on stored dislocation density in the interface was formulated. Hall-Petch with modified coefficients provided a good fit down to about 5 nm, below which experimental data starts to deviate. It is suggested that at this layer thickness, dislocations accumulate in the interface, and assuming there is a constant dislocation density in each interface, the strength varies as $h^{-1/2}$. A viewpoint Scripta Materialia paper has been submitted on this study.

In-situ TEM tensile and compression experiments are also presented in this work. Dislocation nucleation, movement and storage was seen in Cu-Nb layer thickness of below 20 nm. It was found out that dislocations, like what was stated in literature, do form a loop and glide in the individual layers. However, it was also noticed that the dislocations migrated towards the interface and seem to be nucleating from there. In other words, interfaces seem to be sites for dislocation storage and thus cannot be disregarded.

In the last and fourth chapter, 3D laser printed Inconel 718 microchannel heat exchangers, which can be categorized as multilayered as they are printed layer by layer, were investigated. Laser based 3D printing requires no preheat and the operating temperature of the build chamber relatively low compared to the power of the beam. This differential heating and cooling leads to rapid solidification and high residual strain. The microstructures produced with this technique were heterogeneous, and so were the hardness and yield strength values. Hardness values after heat treatment (HT) clearly increased due to the formation of precipitates, when compared with the as-built parts. Measured hardness was comparable to the wrought or cast IN 718. Micropillar compression tests of HT IN 718 were carried out to obtain stress-strain

curves and to locally study strength behavior. About 200 MPa of difference in yield strength was observed in any given grain, when compressions were done at two locations. In a scan area of $\sim$ 200 x 200 μm, about 500 MPa difference in yield strength was observed when two tests were conducted on two different grains. This highlights the amount of heterogeneity in strength even in a small area. The yield strength values were comparable to or even higher than conventionally manufactured IN 718. An IPF map after HT showed significant orientation gradients in each grain. This signifies partial or no recrystallization and only grain growth during HT. Therefore, solution annealing at a higher temperature, at around 1200^{o}C, is recommended for full recrystallization. Similarly, process parameters and their effect on the amount and types of defects, i.e. porosity, was studied. Porosity is one of the primary concerns in 3D printed parts, as they act as the site of fatigue failure, especially the ones on the surface. It was seen that the nominal process parameter set gave the best part quality i.e. most dense part. The study was done using X-ray Computed microtomography at APS at Argonne National Lab. The twin content of these superalloys was also very low, i.e. less than 0.5 % both before and after heat treatment. Regularly manufactured IN 718, however has over 40 % length fraction of twin boundaries.

From this it can be concluded that different tools and techniques were applied to study these multilayered materials in details. The localized strain properties of ARB fabricated HPT material were understood better. Microstructural instability was the result of shear deformation. A model that can accurately predict strength behavior at the CLS range was formulated. With in-situ TEM testing, the role of interface in dislocation nucleation and storage was discovered. For the first time, in-situ TEM tensile tests were conducted in 18 nm Cu-Nb. Similarly, in additively manufactured IN 718, we attempted to integrate laser scan parameters, fabrication method, heat treatment

procedures to the resulting microstructure and mechanical properties.

5.2 Future Directions

Detailed future directions has been highlighted in each chapter. Here is a summary of possible future work.

1. HRTEM work focusing on Cu-Nb interface to image the dislocations. Possibly, only zooming in over one of the interfaces to watch dislocations moving in and out during straining.

2. Studying dislocation behavior in 140 nm Cu-Nb nanolaminates, as the 140 nm sample preparation did not go as expected.

3. In this thesis, a 10.8 strain HPT sample was studied using ASTAR^{TM}. 4.2 and 6.5 strain regions should also be studied to have a deeper understanding of the initiation of the folds.

4. Study dislocation behavior of a Cu-Nb case, where a fine layer (< 5 nm) is situated next to a coarser layer.

5. Multiple consecutive heat treatments (using higher temperature) could be performed in 3D printed IN 718. Micropillar compression test is recommended in orientation free material to check the consistency in yield strength.

6. Study recrystallization behavior of IN 718 in more detail.

7. The theory behind the surprisingly low twin density in printed samples of IN 718 should be studied. It is important to understand the driving force for it.

8. TEM characterization is recommended to understand the precipitate formation and its effect on the material strength.

9. Fatigue experiments are recommended to predict the failure for parts manufactured using different processing conditions.

Chapter 6

List of Publications from this Work

1. S. Subedi, R, Pokharel, A.D Rollett, “Orientation gradients in relation to grain boundaries at varying strain level and spatial resolution" in *Material Science and Engineering A*, 638(25):348-356, 2015

2. E. Rasouli, S. Subedi, V. Narayanan, A.D. Rollett, J. Beuth, K. Drost, “Design of Compact Heat Exchangers for Supercritical Carbon dioxide Cycles", *Proceedings of the First Pacific Rim Thermal Engineering Conference*, March, 2016

3. S. Subedi, A.D. Rollett, I.J. Beyerlein, R.A. LeSar, “Strength of Nanoscale Metallic Multilayers", *Scripta Materialia*, Viewpoint paper, “accepted", 2017

4. S. Subedi, I.J. Beyerlein, E. Ekiz, P. Bellon, A.D. Rollett, “Investigation of microstructural and mechanical stability of CuNb composites after high-pressure torsion (HPT)" (in preparation)

5. S. Subedi, S. Singh, A.D. Rollett, M. DeGraef, “A dictionary approach to automated indexing of EBSD patterns in finely twinned microstructures" (in preparation)

6. S. Subedi, E. Rasouli, V. Narayanan, A.D. Rollett, “Fabrication of Microchannel Monolithic Heat Exchanger Using Additive Manufacturing", (in preparation)

Appendices

Appendix A

Additive Manufacturing of Advanced Heat Exchanger

More advanced prototype of heat exchangers were 3D printed, as shown in Figure A.1

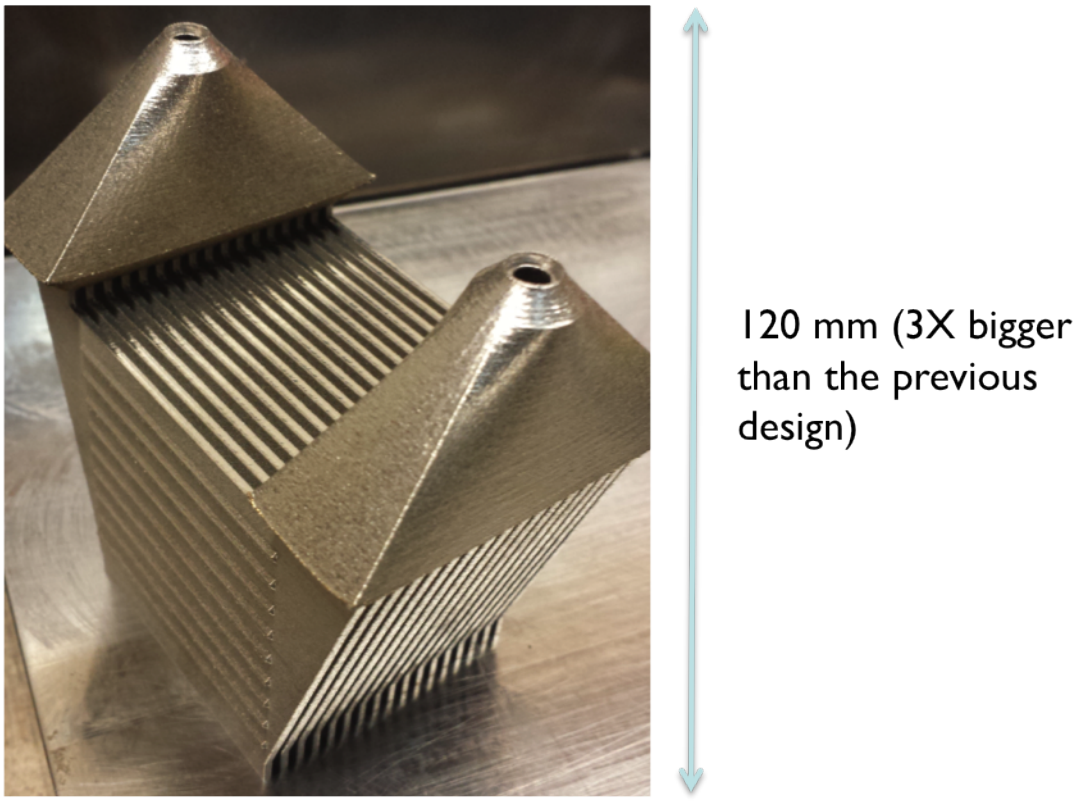

Figure A.1: More advanced prototype of heat exchanger

Appendix B

Orientation Gradients in Relation to Grain Boundaries at Varying Strain Level and Spatial Resolution

B.1 Introduction

Plastic deformation in polycrystals at mesoscale is known to be heterogeneous, which can be attributed in part to crystallographic anisotropy exhibited by individual grains and in part to the tendency of dislocations to be stored in a non-uniform manner. Diffraction microscopy methods can provide spatially resolved discrete orientation maps either from surface EBSD or bulk near-field High-Energy Diffraction Microscopy (nf-HEDM) [128] of the sample. This discrete data provides an opportunity to investigate orientation gradient development and orientation change during plastic deformation at a local level. A previous study utilized the nf-HEDM method to study spatially-resolved microstructure evolution in Cu, where lattice rotation, orientation change, and orientation gradient development were reported up to 14 % tensile strain [40, 128]. Experimental observations were compared with a crystal plasticity model. Experimental results illus-

trated high KAM values near boundaries at lower strain levels, while at larger strains, a broader distribution in KAM values was observed away from the grain boundaries. However, in computer simulations (using FFT based visco-plastic simulation (VPFFT)), high KAM values were predicted near grain boundaries [40, 128]. The latter is an expected phenomenon since dislocations generally accumulate at the grain boundary (GB)[129, 130, 131]. This significant discrepancy between experiment and simulation highlights the importance of conducting a thorough experiment, to test the dependence of KAM on step size.

One possible explanation of this discrepancy is an inadequate spatial resolution in nf-HEDM. In this particular study, the spatial resolution of the orientation maps obtained from nf-HEDM scans was 2.8 μm. However, the size of the subgrain structures for copper is known to be at a submicron length scale [40, 128, 131, 36]. It is hypothesized that the step size used in HEDM was too coarse to capture sub-grain features in copper. Kamaya et al. [35] stated that the orientation spread depends on "the degree of plastic strain but not on the data density of the crystal orientation map," while Takamaya et al. [39, 132] reports that "the magnitude of KAM is affected by step size." Similarly, Wright et al. [41] also clearly mentions that KAM is highly sensitive to the step size. Furthermore, Li observed "sharpening of boundaries" and "convergence" of KAM features with increasing spatial resolution [133].

In this work, we have used KAM as a metric for quantifying local orientation gradient and investigated the resolution dependance on KAM calculation. EBSD allows for finer resolution for mapping crystal orientation at approximately 50 nm spatial resolution [134]. This work was performed on the same sample of copper on which HEDM was performed. A resolution study at different strain levels was carried out to see how the

experimental KAM behavior changes in relation to grain boundaries when step sizes are changed and a direct comparison between the two methods is presented in this study.

B.2 Hypothesis

We hypothesize that analysis of orientation gradients at high strain is affected by spatial resolution because the spatial distributions of orientations is not random. This will be tested by performing EBSD on a deformed polycrystalline copper.

B.3 Materials and Experimental Method

For this experiment, a highly annealed 99.9995 % pure copper specimen, having a 1 mm diameter gauge section (shown in Figure B.1a), was pulled to failure in tension and cross-sectioned parallel to the tensile axis. The sample was polished on a mechanical polisher using 600, 800, and 1200 grit SiC paper for about 3 minutes each in order to remove the surface roughness of the sample. Next, 9, 3 and 1 μm diamond polishing was performed using an oil-based suspension for 5 minutes. Final polishing was done using colloidal silica slurry for a high quality surface finish for EBSD. A fiducial mark was made in order to have an estimate of where the scans were being taken.

Once the sample was prepared, EBSD scans were taken using EDAX/TSL acquisition software with a Hikari EBSD detector on a Quanta 200 FEG SEM. The microscope settings used were an accelerating voltage of 20 KV, a spot size of 5 and an aperture size 5. 150×150 μm square grid scans were taken at regions of different strain level. Step sizes were varied from 2.5, 1, 0.5 and 0.2 μm at both high strain and low strain scans. Each of these maps was cleaned using the single dilation cleanup with the single iteration

option. Further analysis on KAM spread was done using built-in KAM functions in TSL.

B.4 Results and Discussion

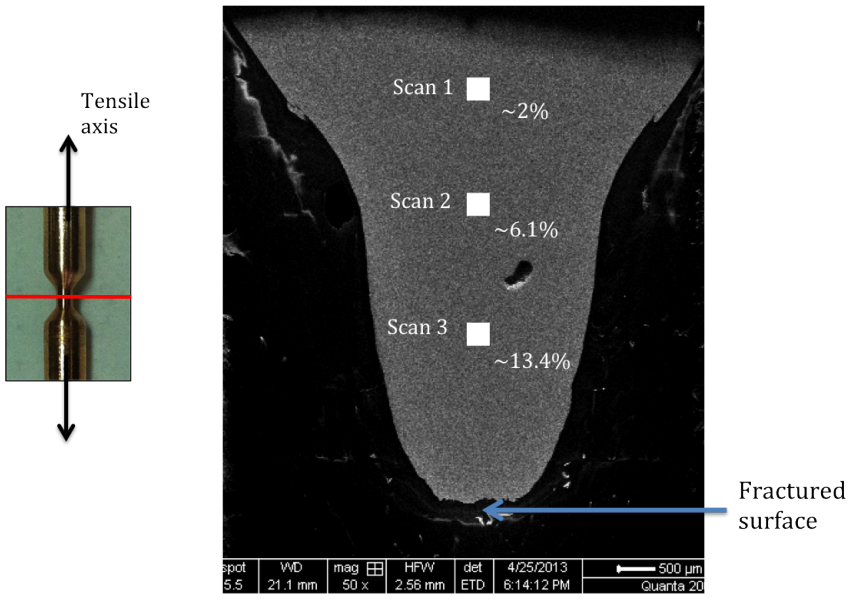

(a) (b)

Figure B.1: a) Copper sample with a cylindrical gauge section of 1 mm diameter and 1 mm height. b) Cross-section gauge section showing three different scan regions with their respective estimated strain. A fiducial mark (between 2nd and 3rd mark) was made to aid in locating and orienting the EBSD scans relative to the low magnitude images of the cross-section.

As shown in Figure B.1b), EBSD maps were taken at three scan regions, with each having a different level of plastic strain. Scan 3 (closest to the fractured surface) clearly has high strain while Scan 1 (farthest from the fractured surface) has comparatively low strain. Change in diameter at each scan region were recorded in order to estimate

the amount of strain. It should be noted that while grinding the gauge section care was taken to ensure that the section was in plane relative to the centerline. The initial diameter of the gage section was 1000 μm. The final diameters at region 1-3 were measured to be 990, 970, and 935.1 μm respectively. The strain at each point was thus estimated to be 2 %, 6.1 % and 13.4 % by using the strain formula for diameter:

$$\text{T}true\ strain = \ln\left(\frac{A_o}{A}\right) = \ln\left(\frac{d_o^2}{d^2}\right) \tag{B.1}$$

Here $A_\circ$ is the initial and A is the current cross-sectional area. Similarly, $d_\circ$ is the initial and d is the local diameter.

After the approximate strain was calculated at each scan point, misorientation distributions were examined.

B.4.1 KAM behavior dependent on strain

Orientation maps were generated for the three selected regions shown in Figure B.1b). The initial EBSD scan was performed using a 2.5 μm step size, which is similar to the spatial resolution used in the nf-HEDM study. Inverse pole figure (IPF) maps are plotted for scans 1-3, which are shown in Figure B.2a. From the IPF maps, it is obvious that the grains are elongated parallel to the tensile axis with increasing strain. Misorientation development is evident through a decrease in average confidence index (CI) and image quality (IQ) values of the measured Kikuchi pattern. KAM was calculated from 2D orientation maps up to the second nearest neighbors. KAM maps as shown in Figure B.2b) (given by orientation imaging microscopy (OIM) analysis software) illustrate that the average KAM value increases with increasing strain. In general, as the plastic strain increases, dislocation density and KAM accumulation in the microstructure increases, with corresponding decreases of average CI and IQ.

At lower strains, higher KAM values seem to be localized near some grain boundaries, but no obvious trend can be seen from the KAM maps in Figure B.2b). In order to quantify the relationship between orientation gradient and microstructural features, a more statistical approach was taken by correlating KAM and distance from grain boundary (GB). For this, a Euclidean distance map [135, 131] was computed based on the distance from the nearest grain boundary. For the pair of variables, one variable was chosen as the independent variable (distance from GB) and the values of the other variable (KAM) were binned against it [135]. Thus, the average KAM against distance from GB was plotted. The binning process could be repeated for the complementary choice of independent variable.

From Figure B.2c) it is clear that, at low strain, the largest KAM values occur close to grain boundaries. On average, KAM decreases with increasing distance from a boundary towards the interior of a grain. Counter-examples of this overall trend, however, were found in the high strain region. Here large KAM values were observed inside the grain, which is, in fact, consistent with what was observed with the HEDM study. With increasing distance from GB, KAM first increases and then falls off. This behavior is not as expected but could be explained using grain fragmentation phenomenon which explains that there is a development of sub-grains structures at high plastic strains [136]. Thus step size becomes crucial since it needs to be fine enough to capture those sub-grain features inside the grain.

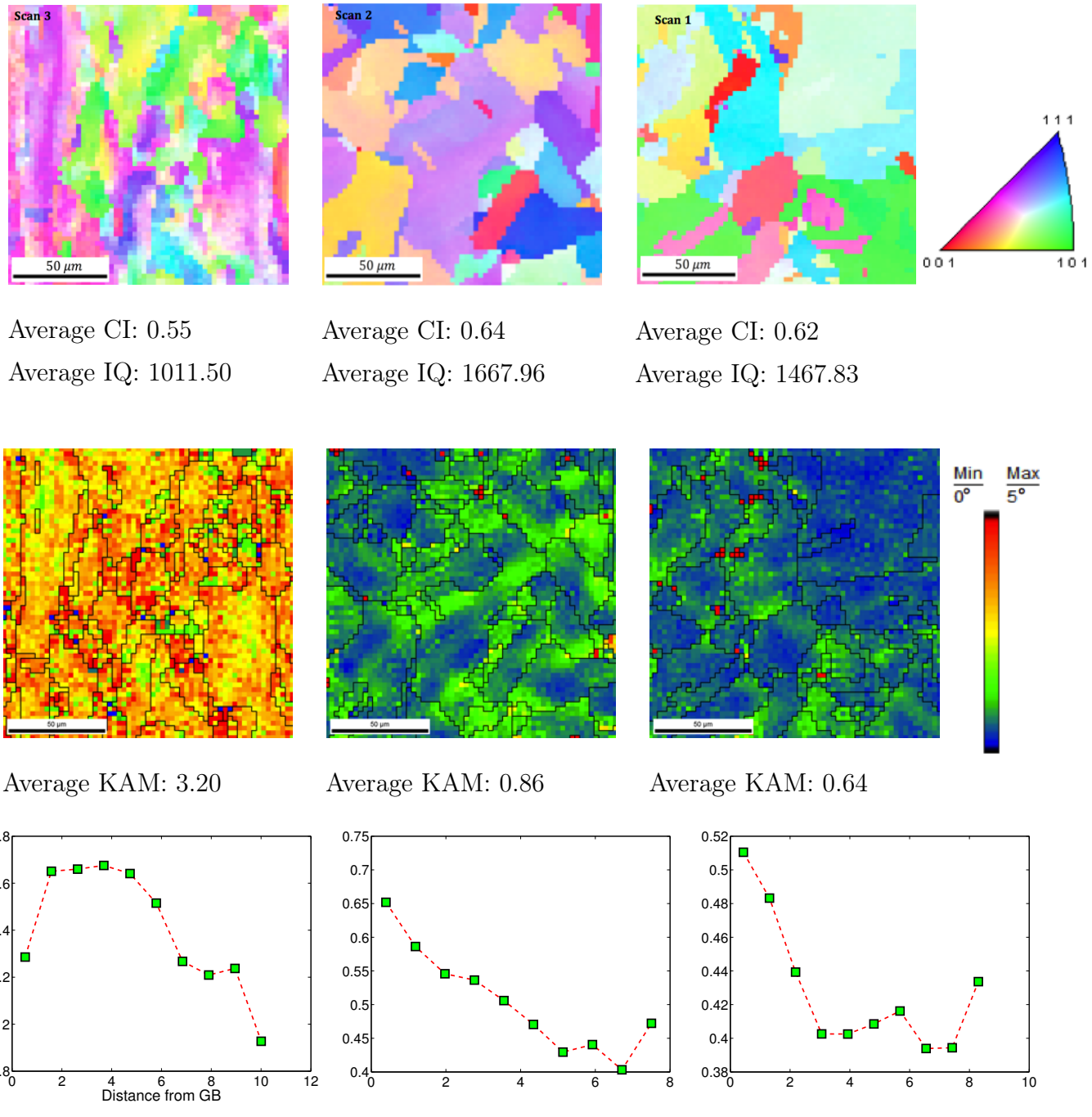

Figure B.2: a) IPF maps showing orientation mapping, average CI and IQ b) KAM map c) KAM vs. Distance from GB binned by distance. Each box represents a pixel. Thus the unit of distance is 2.5 μm for a maximum of 25 μm in the case of the righthand column.

B.4.2 KAM behavior dependent on step size/resolution

A resolution study was performed at all three regions ('Scan 1', 'Scan 2' and 'Scan 3' respectively). Correlation plots were made to quantify the relationship between KAM and boundary distance as a function of spatial resolution/step size at varying strain levels. Scans 1 and 2 showed a similar lack of significant difference between 2.5 μm and 0.5 μm step size scans, as the strain was evidently not high enough to create very small sub-grain structures. We, therefore, report the details of only the 1st and 3rd scans.

B.4.2.1 Low strain region ('Scan 1')

For 2 % strain, as shown in Figure B.3a, the spatial resolution of the microstructure was refined by changing the step size from 2.5 to 0.5 μm. KAM maps were obtained at both resolutions in order to see if high KAM is localized in a particular region, specifically near grain boundaries. As shown in Figure B.3b, although some high KAM values (indicated by the traces of red and yellow colors) are seen at some grain boundaries, it is not clear that the KAM is localized at grain boundaries. Thus correlation plots were made for these corresponding microstructures. As shown in Figure B.3c for both resolutions, KAM is high at the boundary and gradually decreases towards the interior of the grains. This confirms that due to the coarse dislocation substructure at low strain the calculation of KAM is not sensitive to the step size used.

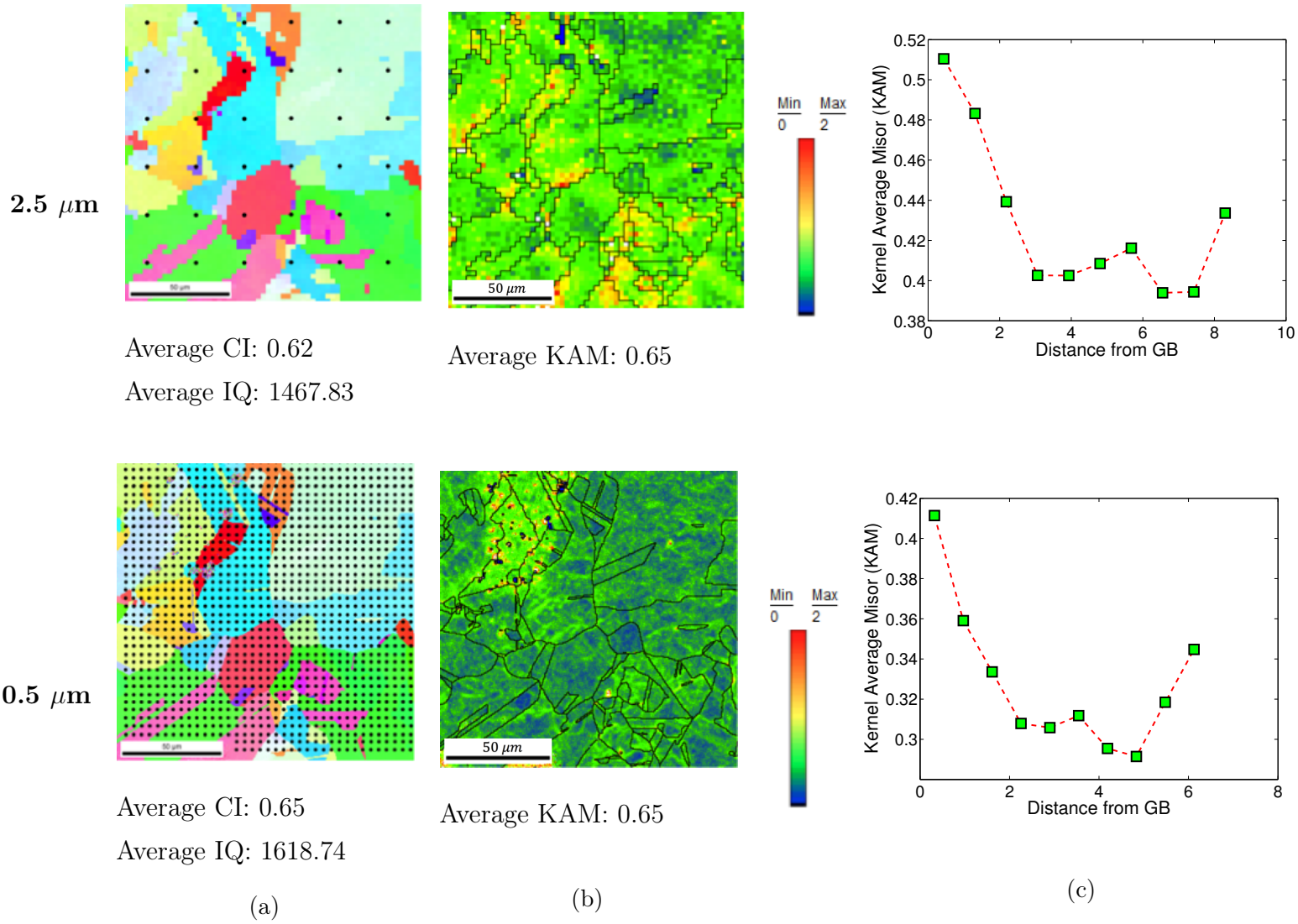

Figure B.3: a) IPF maps showing orientation mapping, black dotted points/grids are to show schematic of step size, average CI and IQ b) KAM map c) KAM vs. Distance from GB binned by distance

B.4.2.2 High strain region ('Scan 3')

The resolution study at the high strain region was of most interest as this is the region where the HEDM study was conducted and the inconsistency with the computational

approach was observed. The highly strained region developed large misorientations and subgrain structures so it is essential to choose the correct step to do the KAM calculation lest incorrect conclusions be drawn. The results from the resolution study are reported in Figure B.4, B.5 and B.6.

Scans with different resolution were taken in the 13.4 % strain region by changing the step size from 2.5 to 1 to 0.5 to 0.2 μm. In this study, 2.5 μm is considered to be a coarse step size, while a submicron step size is considered to be a fine step size. As a result, the nature of the graph changed as the step sizes were changed and the spatial resolution of the microstructure was refined with each consecutive scan as shown in Figure B.4a) and B.4b) below. The finer the resolution the more closely the graph approaches what was expected from previously published research; higher KAM at the GB and lower inside the grain (shown in Figure B.4c) and d) [135, 35]. Box plots (shown in Figure B.5) were also made for these microstructures to show in more detail the distribution of orientation data at each bin, which very closely follows the same trend as earlier.

We note in passing the interesting feature, circled, of a grain with low KAM values that is divided by a twin-related grain with high KAM values. There is a weak dependence on orientation gradient [40] but the sharp difference evident in this location is more likely a consequence of the large local difference in orientation across the pair of twin boundaries.

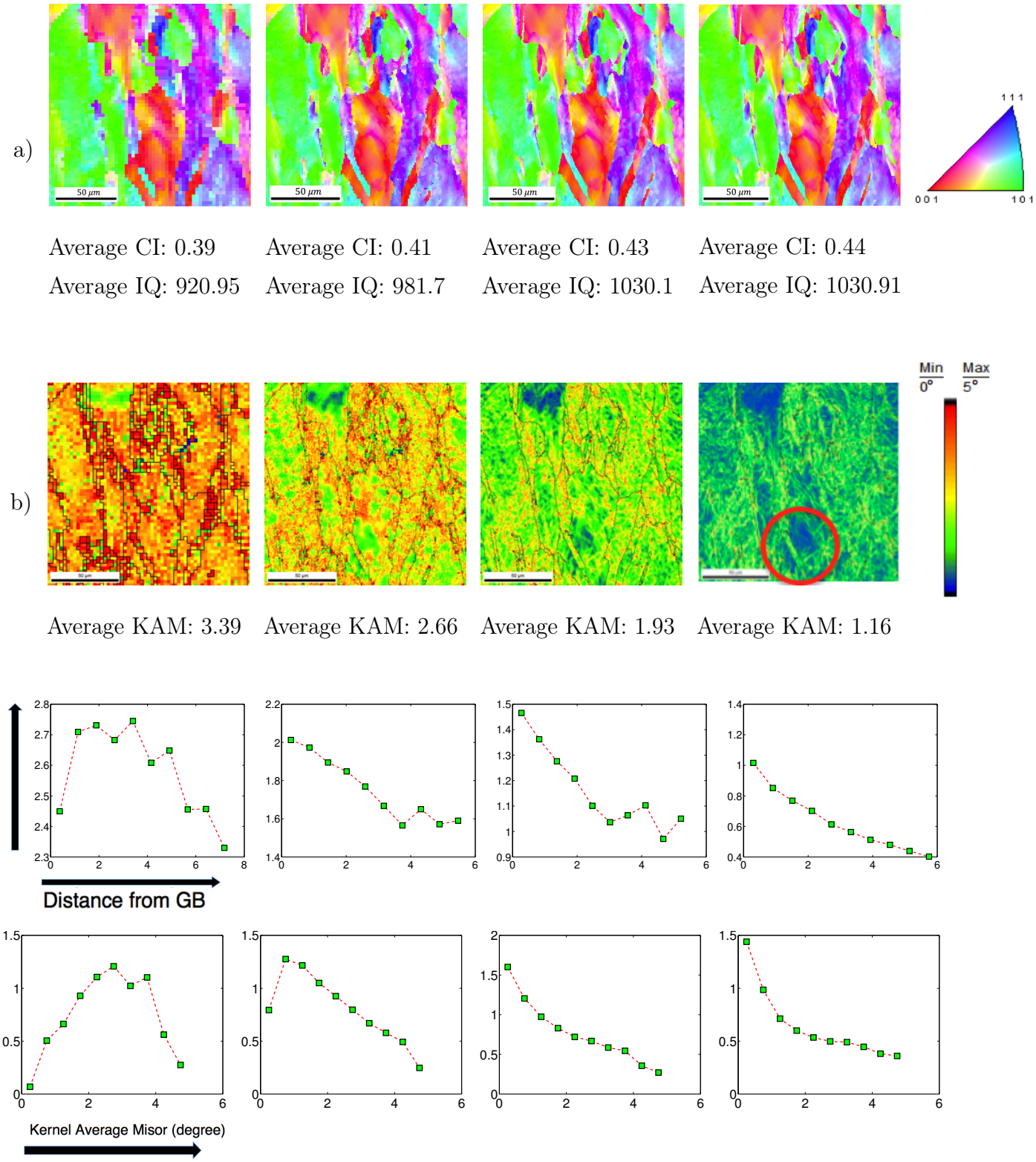

(a) 2.5 μm (b) 1 μm (c) 0.5 μm (d) 0.2 μm

Figure B.4: a) IPF maps showing orientation mapping, average CI and IQ b) KAM maps c) KAM vs. Distance from GB binned by distance d) Distance vs. KAM binned by KAM for (i) 2.5 μm ii 1 μm (iii) 0.5 μm (iv) 0.2 μm scan respectively.

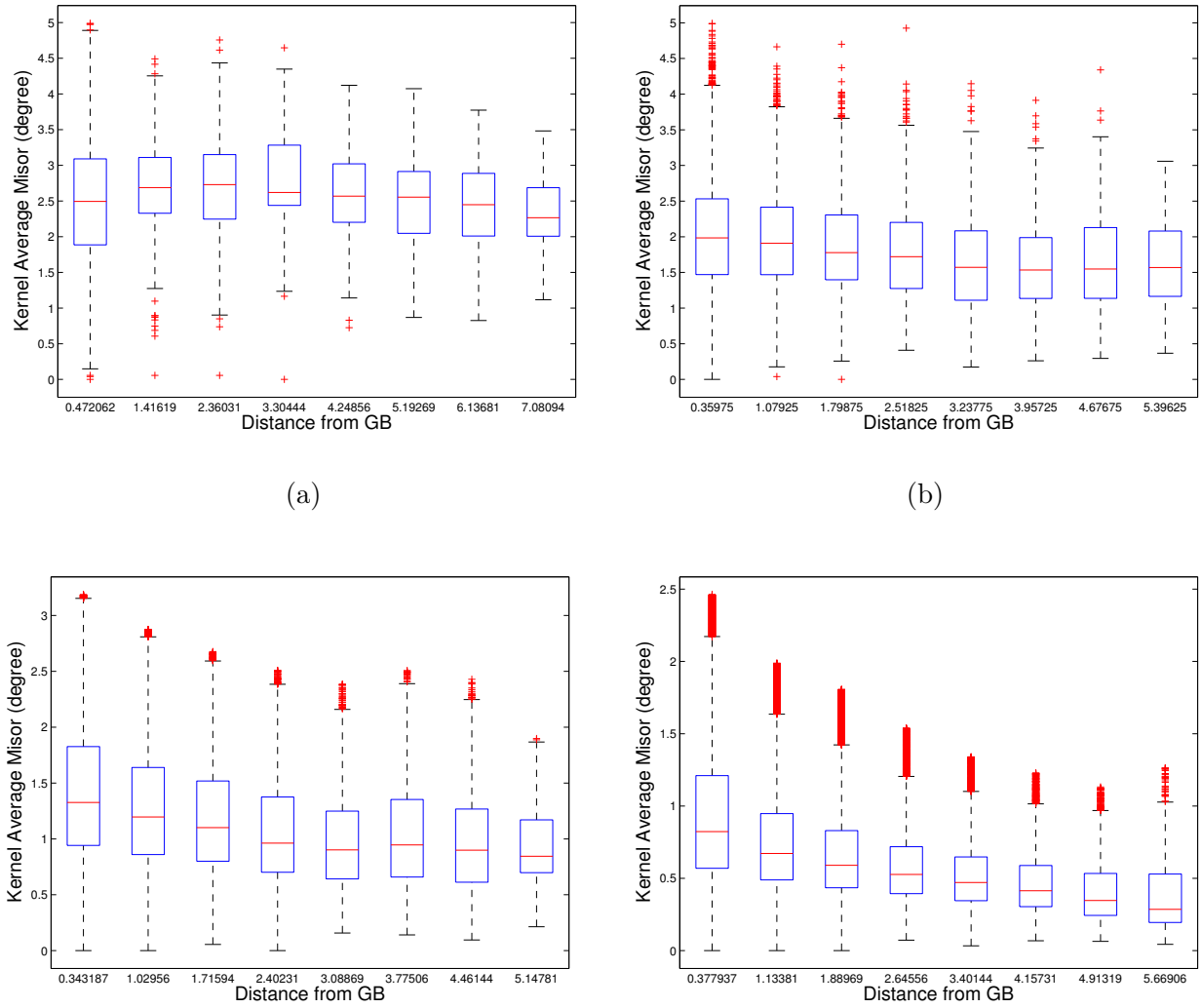

Figure B.5: Box plots for different resolution microstructures i.e. a) 2.5 μm b) 1 μm c) 0.5 μm d) 0.2 μm for 13.4 % strain. Here, the red line is the median of the data, the upper blue line of the rectangular box is the 3rd quartile and the lower blue line is the 1st quartile. The differences between two is the interquartile range (IQR). Any data point more than 1.5 IQR above the third quartile and below the first quartile is an outlier, here denoted by a red cross.

As shown in the box plot for 2.5 μm resolution, the trend closely follows what was observed in Figure B.4c. A large number of outliers can be observed in the 0.2 μm

resolution box plot, but note that as the resolution is refined the number of points evaluated increases as the square of the linear point density. The 0.2 μm dataset has 62.5 times as many data points as 2.5 μm and 25 times as many as 1 μm. So the outliers that are shown in the plot are not significant compared to the number of data points being analyzed. The percentage of data that are outliers is 0.08 % for 2.5 μm, 0.81 % for 1 μm, 2.6 % for 0.5 μm and approximately 7 % for 0.2 μm.

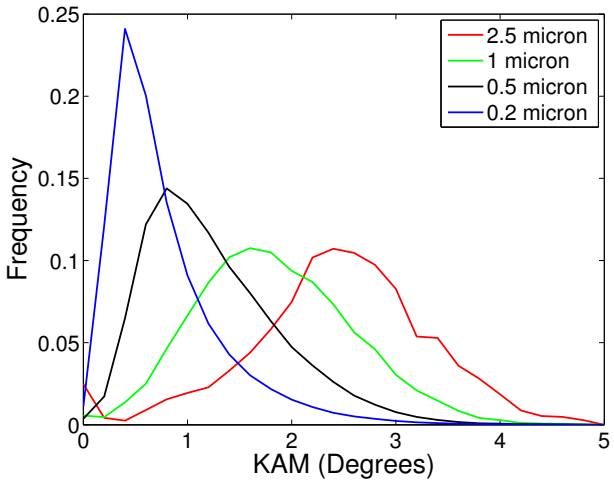

Figure B.6: KAM distribution shown for different resolution scans, with step sizes given in the legend.

Similarly, frequency plots for different spatial resolution scans were also drawn in order to visualize the misorientation distribution for each resolution. The mdeian misorientation value is ≈2.5° at a 2.5 μm step size whereas it is ≈0.3° at 0.2 μm. This drastic change in misorientation distribution with step size again emphasizes the strong influence of step size on KAM values.

B.4.2.3 Sub-sampling

In the 13.4 % strain region, subsampling was also done on the 0.2 μm step size scan to see whether the same result would be obtained as for varying the physical step size, i.e. the results shown in Figure B.4. For this study the finest scan i.e 0.2 μm scan was taken

and alternate rows and columns were removed to coarsen the scan; in other words, to artificially increase the step size from 0.2 μm to step sizes of 0.4, 0.8, 1.6, 2.4 μm. Then the corresponding KAM values as a function of distance from GB and distance from GB as a function of KAM were plotted, as shown in Figure B.7. The result demonstrated that the same variation in KAM distribution is found from sub-sampling as was obtained with physical variations in step size.

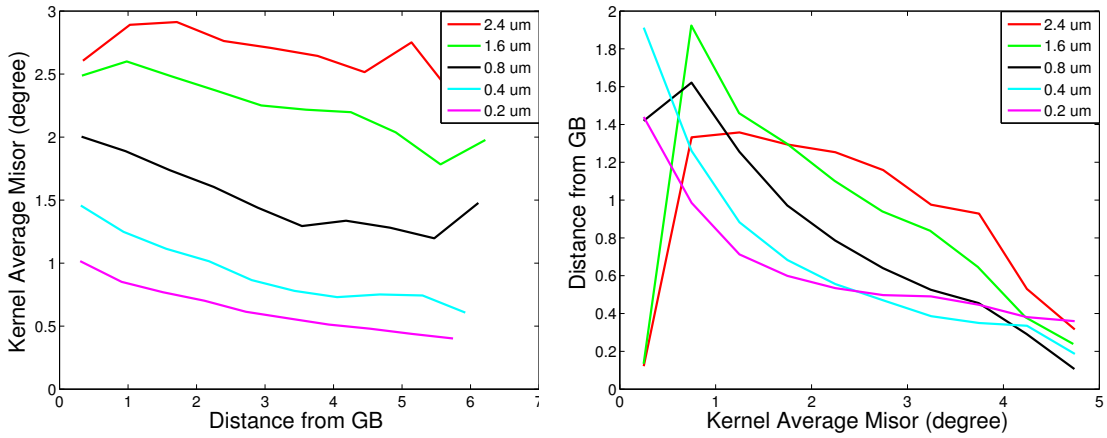

(a) (b)

Figure B.7: Sub-sampling results for a) KAM vs. distance b) Distance vs. KAM. The effective spatial resolution is shown in the legend.

B.5 Hypothesis revisited

As shown above in the results and discussion section, the measurement of orientation as quantified by KAM depends on the spatial resolution of the scans. This helps explain the discrepancy observed between experimental and simulated results in the previous HEDM study which it can be concluded that due to the coarse resolution used (2.8 microns) high concentration of KAM gradient were seen inside the grain. If the resolution could be increased, a more reasonable result would have been obtained.

B.6 A model to rationalize the variation in the KAM-distance relationship with resolution

In this section, we propose a simple model to rationalize the observation that lower KAM values are obtained near grain boundaries at coarse step sizes (above about a micron in the investigated copper). It is hypothesized that the orientation gradients perpendicular to the grain boundaries are larger than those parallel to GB. For a point adjacent to a grain boundary, such as the one shown in Figure B.8, some of the points are naturally excluded because they lie outside the grain and have misorientations greater than the typical threshold of 5°. Out of the remaining points, if the orientation gradients parallel to the boundary are not as strong then, overall, the average KAM value decreases.

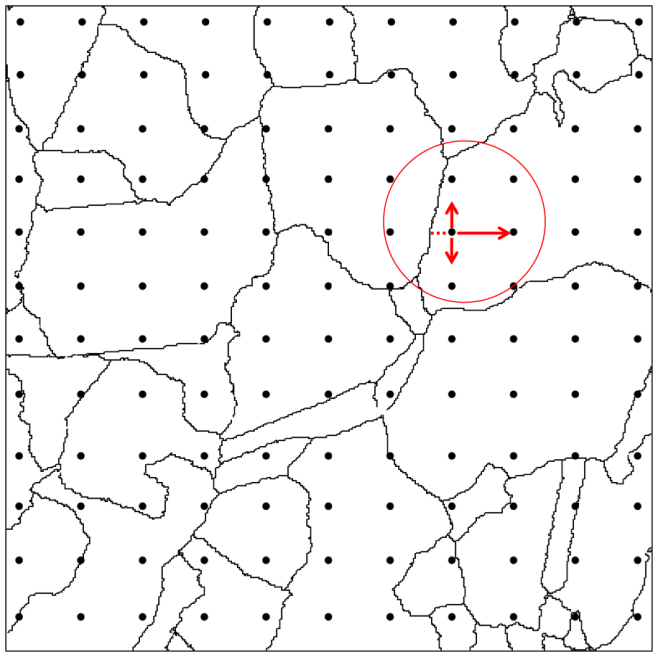

Figure B.8: Schematics of KAM calculation at GB is shown, where dotted line represents the direction in which a neighboring point is ignored. A solid long arrow indicates a stronger gradient whereas a shorter arrow indicates a weaker gradient.

In order to assess the hypothesis quantitatively, multiple parallel and perpendicular traces of misorientation values relative to the initial point were extracted from the orientation maps. Average values of both these types of misorientation trace are plotted in Fig. B.9a. It is clear that the average misorientation value perpendicular to grain boundaries is larger than the average misorientation value parallel to grain boundaries, which supports the hypothesis. A typical example of what a perpendicular and parallel line plot for misorientation versus distance from GB is shown in Fig. B.9b and c. We note that gradients in orientation near grain boundaries have been remarked on in the literature several times. Mishra et al., for example, measured enough gradients perpendicular to boundaries to make the case that larger gradients are found near boundaries than in the interior of grains [129]. The analysis of perpendicular versus parallel orientation gradients is, however, new to this work.

B.7 Conclusion

Orientation gradients, quantified in terms of KAM, were measured as a function of strain and spatial resolution. Local orientation information from EBSD was analyzed to map KAM vs. Distance from GB for different resolution scans. In both the low and high strain regions, the spatial resolution of the microstructure was varied by changing the step size of the scan. The resolution effect on KAM calculation was thus tested at both strain regions. Listed below are the key findings:

1. At low strain, since the scale of the dislocation substructure in the grains is coarse enough, the calculation of KAM is not resolution dependent. Irrespective of the step size used, high values of KAM are seen near the grain boundaries and

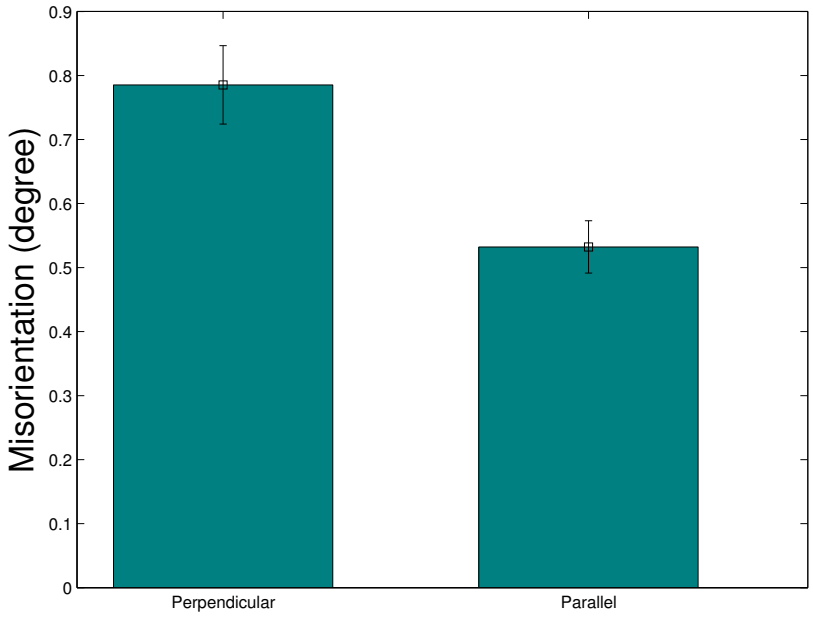

(a)

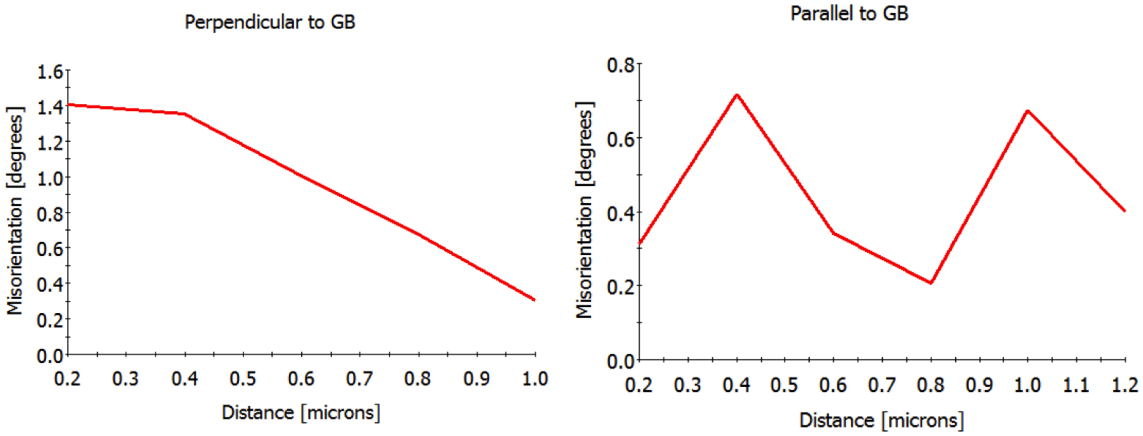

(b) (c)

Figure B.9: a) Bar chart showing average misorientation value parallel and perpendicular to grain boundaries b) perpendicular line plot c) parallel line plot.

gradually decrease towards the interior of the grain.

2. However, at high strain, due to the highly misoriented grains and the formation of submicron dislocation structures, it is crucial to choose the correct step size. Using

a coarser (2.5 μm) step size, high KAM was seen inside the grain whereas using a finer (0.5 μm) step size the location of the highest KAM values moved to the grain boundary. Since dislocations generally accumulate at the grain boundary resulting in high misorientation, the latter is believed to be a more accurate observation especially when allied with the computational results.

3. From this study, it can be concluded that one must choose a fine enough step size such that the dislocation substructure is sampled with sufficient resolution. Based on the results reported here, it can be deduced that in pure copper 0.5 μm or at least a sub-micron step size should be considered in order to capture all the post deformation features.

Bibliography

[1] A. Misra and R.G. Hoagland. Plastic flow stability of metallic nanolaminate composites. *Journal of Materials Science*, 42(5):1765–1771, 2007.

[2] A Misra, M Verdier, Y.C Lu, H Kung, T.E Mitchell, M Nastasi, and J.D Embury. Structure and mechanical properties of Cu-X (X = Nb, Cr, Ni) nanolayered composites. *Scripta materialia*, 39(4–5):555 – 560, 1998.

[3] A. Misra, J. P. Hirth, and H. Kung. Single-dislocation-based strengthening mechanisms in nanoscale metallic multilayers. *Philosophical Magazine A - Physics of Condensed Matter Structure Defects and Mechanical Properties*, 82:2935–2951, 2002.

[4] A. F. Jankowski. Vapor deposition and characterization of nanocrystalline nanolaminates. *Surface and Coatings Technology*, 203(5-7):484 – 489, 2008. Proceedings of the 35th International Conference on Metallurgical Coatings and Thin Films.

[5] K. O. Schweitz, J. Chevallier, J. Bottiger, W. Matz, and N. Schell. Hardness in Ag/Ni, Au/Ni and Cu/Ni multilayers. *Philosophical Magazine A*, 81(8):2021–2032, 2001.

[6] M.A. Phillips, B.M. Clemens, and W.D. Nix. A model for dislocation behavior during deformation of Al/Al3Sc (fcc/$L1_2$) metallic multilayers. *Acta Materialia*, 51(11):3157 – 3170, 2003.

[7] X. Zhang, A. Misra, H. Wang, T.D. Shen, M. Nastasi, T.E. Mitchell, J.P. Hirth, R.G. Hoagland, and J.D. Embury. Enhanced hardening in Cu/330 stainless steel multilayers by nanoscale twinning. *Acta Materialia*, 52(4):995 – 1002, 2004.

[8] R. Li. Defect mediated plasticity in Cu/Ag nanoscale multilayered metal composites: deformation twinning and wavy interface formation. Master's thesis, University of Illinois at Urbana-Champaign, 2013.

[9] Niaz Abdolrahim, Hussein M. Zbib, and David F. Bahr. Multiscale modeling and simulation of deformation in nanoscale metallic multilayer systems. *International Journal of Plasticity*, 52:33 – 50, 2014. In Honor of Hussein Zbib.

[10] J.S. Carpenter, S.C. Vogel, J.E. LeDonne, D.L. Hammon, I.J. Beyerlein, and N.A. Mara. Bulk texture evolution of Cu-Nb nanolamellar composites during accumulative roll bonding. *Acta Materialia*, 60(4):1576 – 1586, 2012.

[11] W. Han, M.J. Demkowicz, N. A. Mara, E. Fu, S. Sinha, A.D. Rollett, Y. Wang, J.S. Carpenter, I.J. Beyerlein, and A. Misra. Design of radiation tolerant materials via interface engineering. *Advanced Materials*, 25(48):6975–6979, 2013.

[12] N.A. Mara and I.J. Beyerlein. Interface-dominant multilayers fabricated by severe plastic deformation: Stability under extreme conditions. *Current Opinion in Solid State and Materials Science*, 19(5):265 – 276, 2015.

[13] I.J. Beyerlein, N.A. Mara, J.S. Carpenter, T. Nizolek, W.M. Mook, T.A. Wynn, R.J. McCabe, J.R. Mayeur, K. Kang, S. Zheng, J. Wang, and T.M Pollock. Interface-driven microstructure development and ultra high strength of bulk nanostructured Cu-Nb multilayers fabricated by severe plastic deformation. *Journal of Materials Research*, 28:1799–1812, 2013.

[14] M.J. Demkowicz and L. Thilly. Structure, shear resistance and interaction with point defects of interfaces in Cu-Nb nanocomposites synthesized by severe plastic deformation. *Acta Materialia*, 59(20):7744 – 7756, 2011.

[15] E.H. Ekiz, T.G. Lach, R.S. Averback, N.A. Mara, I.J. Beyerlein, M. Pouryazdan, H. Hahn, and P. Bellon. Microstructural evolution of nanolayered Cu-Nb composites subjected to high-pressure torsion. *Acta Materialia*, 72:178–191, 2014.

[16] B.L. Hansen, J.S. Carpenter, S.D. Sintay, C.A. Bronkhorst, R.J. McCabe, J.R. Mayeur, H.M. Mourad, I.J. Beyerlein, N.A. Mara, S.R. Chen, and G.T. Gray III. Modeling the texture evolution of Cu/Nb layered composites during rolling. *International Journal of Plasticity*, 49:71 – 84, 2013.

[17] J.S. Carpenter, X. Liu, A. Darbal, N.T. Nuhfer, R.J. McCabe, S.C. Vogel, J.E. LeDonne, A.D. Rollett, K. Barmak, I.J. Beyerlein, and N.A. Mara. A comparison of texture results obtained using precession electron diffraction and neutron diffraction methods at diminishing length scales in ordered bimetallic nanolamellar composites. *Scripta Materialia*, 67(4):336 – 339, 2012.

[18] J. S. Carpenter, R. J. McCabe, S. J. Zheng, T. A. Wynn, N. A. Mara, and I. J. Beyerlein. Processing parameter influence on texture and microstructural evolution in Cu-Nb multilayer composites fabricated via accumulative roll bonding. *Metallurgical and Materials Transactions A*, 45(4):2192–2208, 2014.

[19] D. Bhattacharyya, N.A. Mara, P. Dickerson, R.G. Hoagland, and A. Misra. Compressive flow behavior of Al-TiN multilayers at nanometer scale layer thickness. *Acta Materialia*, 59(10):3804–3816, 2011.

[20] A. Mira and L. Thilly. Structural metals at extremes. *MRS Bulletin*, 35:965–972, 12 2010.

[21] D. Raabe, P Choi, Y. Li, A. Kostka, X. Sauvage, F. Lecouturier, K. Hono, R. Kirchheim, R. Pippan, and D. Embury. Metallic composites processed via extreme deformation: Toward the limits of strength in bulk materials. *MRS Bulletin*, 35:982 – 991, 12 2010.

[22] E.H Ekiz. *Microstructural evolution and phase stability of Cu/Nb nanolaminates subjected to severe plastic deformation by high pressure torsion.* PhD thesis, University of Illinois at Urbana-Champaign, 2014.

[23] X. Liu, N.T. Nuhfer, A.D. Rollett, S. Sinha, S.-B. Lee, J.S. Carpenter, J.E. LeDonne, A. Darbal, and K. Barmak. Interfacial orientation and misorientation relationships in nanolamellar Cu/Nb composites using transmission-electron-microscope-based orientation and phase mapping. *Acta Materialia*, 64:333 – 344, 2014.

[24] Crystal plasticity, presentation. University of Science and Technology, Korea, 2009, 2009.

[25] S.B. Lee, J.E. LeDonne, S.C.V. Lim, I.J. Beyerlein, and A.D. Rollett. The heterophase interface character distribution of physical vapor-deposited and accumulative roll-bonded Cu-Nb multilayer composites. *Acta Materialia*, 60(4):1747 – 1761, 2012.

[26] D.E. Laughlin D.J. Chakrabarti. The Cu-Nb (Copper-Niobium) system. *Bulletin of Alloy Phase Diagrams*, 2(4):455–460, 1982.

[27] S.C.V. Lim and A.D. Rollett. Length scale effects on recrystallization and texture evolution in Cu layers of a roll-bonded Cu-Nb composite. *Materials Science and Engineering: A*, 520:189 – 196, 2009.

[28] Y. Zhu, R.Z. Valiev, T.G. Langdon, N. Tsuji, and K. Lu. Processing of nanostructured metals and alloys via plastic deformation. *MRS Bulletin*, 35:977 – 981, 12 2010.

[29] F. J. Humphreys and M. Hatherly. *Recrystallization and related annealing phenomena*. Elsevier Science, Oxford, UK, Oxford, UK, 173-220.

[30] O. Engler and V. Randle. *Introduction to texture analysis: macrotexture, microtexture and orientation mapping*. CRC Press, Taylor and Francis group, FL, USA, 2010.

[31] *Texture and Anisotropy: Preferred Orientations in Polycrystals and Their Effect on Materials Properties*. Cambridge University Press, Cambridge, UK, 2000.

[32] E.F. Rauch, S. Rouvimov, S. Nicolopoulos, and P. Moeck. High throughput automated crystal orientation and phase mapping of nanoparticles from hrem - tem images. *Microscopy and Microanalysis*, 15:756–757, 7 2009.

[33] X. Lui. *Electron Diffraction-Based Metrology of Nanocrystalline Materials*. PhD thesis, Carnegie Mellon University, Pittsburgh, PA, 2014.

[34] C. Maurice, J.H. Driver, and R. Fortunier. On solving the orientation gradient dependency of high angular resolution EBSD. *Ultramicroscopy*, 113:171 – 181, 2012.

[35] M. Kamaya, A. J. Wilkinson, and J. M. Titchmarsh. Measurement of plastic strain of polycrystalline material by electron backscatter diffraction. *Nuclear Engineering And Design*, 235(6):713–725, 2005.

[36] J. Jiang, T.B. Britton, and A.J. Wilkinson. Measurement of geometrically necessary dislocation density with high resolution electron backscatter diffraction: Effects of detector binning and step size. *Ultramicroscopy*, 125:1–9, 2013.

[37] S. Ghosh and D. Dimiduk. *Computational methods for microstructure-property relationships*. 2011.

[38] A.J. Schwartz, M. Kumar, B.L. Adams, and D. Field. *Electron Backscatter Diffraction in Materials Science*. Springer, New York, 2nd edition, 2009.

[39] Y. Takayama, J.A. Szpunar, and H. Kato. Analysis of intragranular misorientation related to deformation in an Al-Mg-Mn alloy. *Materials Science Forum*, 495-497(PART 2):1049–1054, 2005.

[40] R. Pokharel. *Spatially resolved in-situ of plastic deformation in polycrystalline copper using high energy X-rays and full-field simulations*. PhD thesis, Carnegie Mellon University, 2013.

[41] S.I. Wright, M.M. Nowell, and D.P. Field. A review of strain analysis using electron backscatter diffraction. *Microscopy and Microanalysis*, 17(3):316–329, 2011.

[42] W. F. Hosford. The mechanics of crystals and textured polycrystals. *Crystal Research and Technology*, 29(4):532–532, 1994.

[43] L. B. Freund. The stability of a dislocation threading a strained layer on a substrate. *Journal of Applied Mechanics*, 54(3):553–557, 1987.

[44] W. D. Nix. Mechanical properties of thin films. *Metallurgical Transactions A*, 20(11):2217–2245, 1989.

[45] H. J. Frost. Deformation mechanisms in thin films. *MRS Proceedings*, 265, Jan 1992.

[46] J.D. Embury and J.P. Hirth. On dislocation storage and the mechanical response of fine scale microstructures. *Acta Metallurgica et Materialia*, 42(6):2051–2056, 1994.

[47] X. Chu and S.A. Barnett. Model of superlattice yield stress and hardness enhancements. *Journal of Applied Physics*, 77(9):4403–4411, 1995.

[48] A. Misra, M. Verdier, H. Kung, J.D. Embury, and J.P. Hirth. Deformation mechanism maps for polycrystalline metallic multilayers. *Scripta Materialia*, 41(9):973–979, 1999.

[49] A. Misra, J.P. Hirth, and R.G. Hoagland. Length-scale-dependent deformation mechanisms in incoherent metallic multilayered composites. *Acta Materialia*, 53(18):4817–4824, 2005.

[50] I. J. Beyerlein, N. A. Mara, J. S. Carpenter, T. Nizolek, W. M. Mook, T. A. Wynn, R. J. McCabe, J. R. Mayeur, K. Kang, S. Zheng, J. Wang, and T. M. Pollock. Interface-driven microstructure development and ultra high strength of bulk nanostructured Cu-Nb multilayers fabricated by severe plastic deformation. *Journal of Materials Research*, 28:1799 –1812, 7 2013.

[51] J. Lian and B. Baudelet. A modified Hall-Petch relationship for nanocrystalline materials. *Nanostructured Materials*, 2(4):415–419, 1993.

[52] H.J. Choi, S.W. Lee, J.S. Park, and D.H. Bae. Positive deviation from a Hall-Petch relation in nanocrystalline aluminum. *Materials Transactions*, 50(3):640–643, 2009.

[53] A. Misra, J.P. Hirth, R.G. Hoagland, J.D. Embury, and H. Kung. Dislocation mechanisms and symmetric slip in rolled nano-scale metallic multilayers. *Acta Materialia*, 52(8):2387 – 2394, 2004.

[54] P.M. Anderson, T. Foecke, and P.M. Hazzledine. Dislocation-based deformation mechanisms in metallic nanolaminates. *MRS Bulletin*, 24(2):27?33, Feb 1999.

[55] Linli Zhu, Haihui Ruan, Xiaoyan Li, Ming Dao, Huajian Gao, and Jian Lu. Modeling grain size dependent optimal twin spacing for achieving ultimate high

strength and related high ductility in nanotwinned metals. *Acta Materialia*, 59(14):5544 – 5557, 2011.

[56] Z.S. You, L. Lu, and K. Lu. Tensile behavior of columnar grained Cu with preferentially oriented nanoscale twins. *Acta Materialia*, 59(18):6927 – 6937, 2011.

[57] A. Misra, X. Zhang, D. Hammon, and R.G. Hoagland. Work hardening in rolled nanolayered metallic composites. *Acta Materialia*, 53(1):221 – 226, 2005.

[58] K. Nyilas, A. Misra, and T. Ungár. Micro-strains in cold rolled CuNb nanolayered composites determined by x-ray line profile analysis. *Acta materialia*, 54(3):751 – 755, 2006.

[59] G.J. Fan, H. Choo, P.K. Liaw, and E.J. Lavernia. A model for the inverse Hall-Petch relation of nanocrystalline materials. *Materials Science and Engineering: A*, 409(1–2):243 – 248, 2005.

[60] N. Hansen. Hall-Petch relation and boundary strengthening. *Scripta materialia*, 51(8):801 – 806, 2004.

[61] X.Y. Qin, X.J. Wu, and L.D. Zhang. The microhardness of nanocrystalline Silver. *Nanostructured Materials*, 5(1):101 – 110, 1995.

[62] T. Kizuka, H. Ichinose, and Y. Ishida. Structure and hardness of nanocrystalline Silver. *Journal of Materials Science*, 32(6):1501 – 1507, 1997.

[63] E. Arzt. Size effects in materials due to microstructural and dimensional constraints: a comparative review. *Acta materialia*, 46(16):5611 – 5626, 1998.

[64] M. J. Demkowicz, R. G. Hoagland, and J. P. Hirth. Interface structure and radiation damage resistance in Cu-Nb multilayer nanocomposites. *Physical Review Letters*, 100(13), 2008. 136102.

[65] E. Martínez, A. Caro, and I. J. Beyerlein. Atomistic modeling of defect-induced plasticity in cunb nanocomposites. *Phys. Rev. B*, 90:054103, Aug 2014.

[66] I. J. Beyerlein, N. A. Mara, J. Wang, J. S. Carpenter, S. J. Zheng, W. Z. Han, R. F. Zhang, K. Kang, T. Nizolek, and T. M. Pollock. Structure - property - functionality of bimetal interfaces. *JOM*, 64(10):1192–1207, 2012.

[67] I. J. Beyerlein, J. Wang, and R. Zhang. Mapping dislocation nucleation behavior from bimetal interfaces. *Acta Materialia*, 61(19):7488 – 7499, 2013.

[68] J. P. Hirth. The influence of grain boundaries on mechanical properties. *Metallurgical Transactions*, 3(12):3047–3067, 1972.

[69] W. Blum and X.H. Zeng. A simple dislocation model of deformation resistance of ultrafine-grained materials explaining Hall-Petch strengthening and enhanced strain rate sensitivity. *Acta Materialia*, 57(6):1966 – 1974, 2009.

[70] W. Blum and X.H. Zeng. A simple dislocation model of deformation resistance of ultrafine-grained materials explaining Hall-Petch strengthening and enhanced strain rate sensitivity. *Acta Materialia*, 59(15):6205 – 6206, 2011.

[71] H. Van Swygenhoven, P. M. Derlet, and A. Hasnaoui. Atomic mechanism for dislocation emission from nanosized grain boundaries. *Phys. Rev. B*, 66:024101, Jun 2002.

[72] D. Farkas and W. A. Curtin. Plastic deformation mechanisms in nanocrystalline columnar grain structures. *Materials Science and Engineering: A*, 412(1-2):316 – 322, 2005.

[73] R. Yuan, I. J. Beyerlein, and C. Zhou. Statistical dislocation activation from grain boundaries and its role in the plastic anisotropy of nanotwinned copper. *Acta Materialia*, 110:8 – 18, 2016.

[74] M. M. Chaudhri. Subsurface strain distribution around vickers hardness indentations in annealed polycrystalline Copper. *Acta materialia*, 46:3047–3056, 1998.

[75] E. Nes, K. Marthinsen, and Y. Brechet. On the mechanisms of dynamic recovery. *Scripta Materialia*, 47(9):607 – 611, 2002.

[76] N. Li, J. Wang, A. Misra, and J.Y. Huang. Direct observations of confined layer slip in Cu/Nb multilayers. *Microscopy and Microanalysis*, 18(5):1155–1162, Oct 2012.

[77] P.J. Imrich, C. Kirchlechner, D. Kiener, and G. Dehm. Internal and external stresses: In situ {TEM} compression of cu bicrystals containing a twin boundary. *Scripta Materialia*, 100:94 – 97, 2015.

[78] L.E. Murr, E. Martinez, K.N. Amato, S.M. Gaytan, J. Hernandez, D.A. Ramirez, P.W. Shindo, F. Medina, and R.B. Wicker. Fabrication of metal and alloy components by additive manufacturing: Examples of 3D materials science. *Journal of Materials Research and Technology*, 1(1):42 – 54, 2012.

[79] N.T. Aboulkhair, N.M. Everitt, I. Ashcroft, and C. Tuck. Reducing porosity in AlSi10Mg parts processed by selective laser melting. *Additive Manufacturing*, 1-4:77–86, 2014. Inaugural Issue.

[80] S. L. N Ford. Additive manufacturing technology : Potential implications for u . s . manufacturing competitiveness. *Journal of International Commerce and Economics (USA)*, 6:1 – 35, 2015.

[81] S. Azadian, L. Y. We, F. Niklasson, and R. Warren. Precipitation in spray-formed in 718. *The minerals and materials society*, 6:617 – 626, 2001.

[82] J. Thompson. Relating microstructure to process variable in beam-based additive manufacturing of IN 718. Master's thesis, Wright State University, 2014.

[83] S. Tin T. M. Pollock. Nickel-Based superalloys for advanced turbine engines: Chemistry, microstructure, and properties. *Materials Characterization*, 22(2):361 – 374, 2006.

[84] J.J. Schirra, R.H. Caless, and R.W Hatala. The effect of laves phase on the mechanical properties of wrought and cast + HIP Inconel 718. *The Minerals, Metals & Materials Society,*, 6:375 – 388, 1991.

[85] X. Cao, B. Rivaux, M. Jahazi, J. Cuddy, and A. Birur. Effect of pre- and post-weld heat treatment on metallurgical and tensile properties of Inconel 718 alloy butt joints welded using 4 kW Nd:YAG laser. *Journal of Materials Science*, 44(17):4557–4571, 2009.

[86] W. J. Sames V. *Additive Manufacturing of Inconel 718 using Electron Beam Melting: Processing, Post-Processing, & Mechanical Properties*. PhD thesis, Texas A&M University, 2015.

[87] G.P. Dinda, A.K. Dasgupta, and J. Mazumder. Laser aided direct metal deposition of Inconel 625 superalloy: Microstructural evolution and thermal stability. *Materials Science and Engineering: A*, 509(1-2):98 – 104, 2009.

[88] K.N. Amato, S.M. Gaytan, L.E. Murr, E. Martinez, P.W. Shindo, J. Hernandez, S. Collins, and F. Medina. Microstructures and mechanical behavior of Inconel 718 fabricated by selective laser melting. *Acta Materialia*, 60(5):2229 – 2239, 2012.

[89] G.P. Dinda, A.K. Dasgupta, and J. Mazumder. Texture control during laser deposition of nickel-based superalloy. *Scripta Materialia*, 67(5):503 – 506, 2012.

[90] D.H. Smith, J. Bicknell, L. Jorgensen, B.M. Patterson, N.L. Cordes, I. Tsukrov, and M. Knezevic. Microstructure and mechanical behavior of direct metal laser sintered Inconel alloy 718. *Materials Characterization*, 113:1 – 9, 2016.

[91] S. X. Li, F. Z. Xuan, and S. T. Tu. In situ observation of interfacial fatigue crack growth in diffusion bonded joints of austenitic stainless steel. *Journal of Nuclear Materials*, 366(1-2):1 – 7, 2007.

[92] M. Ghazvini, V. Narayanan, M.K. Drost, and B.K. Paul. Microscale combustor-heat exchanger, 2015. US Patent App. 14/322,104.

[93] E. Rasouli. *Single-Phase and Flow Boiling Heat Transfer and Flow Characterization in Microscale Pin Fin Heat Sinks*. PhD thesis, Oregon State University, 2015.

[94] W. J. Sames, F. A. List, S. Pannala, R. R. Dehoff, and S. S. Babu. The metallurgy and processing science of metal additive manufacturing. *International Materials Reviews*, 61(5):315–360, 2016.

[95] What is binder jetting? `http://www.exone.com/Resources/Technology-Overview/What-is-Binder-Jetting`. Accessed: 2017-01-3.

[96] EOS nickelalloy HX material data sheet EOS M 290. `https://cdn0.scrvt.com/eos/ff2fe7fc83afe675/924df8fd599a/NilAll-HX-M280_M290_Material_data_sheet_05-14_en.pdf`. Accessed: 2017-01-18.

[97] Montgomery C, J. Beuth, L. Sheridan, and N. Klingbeil. Process mapping of Inconel 625 in laser powder bed additive manufacturing. *Solid Freeform Fabrication Proceedings, Univ. Tex. Austin*, pages 1195–1204, 2015.

[98] J. Beuth, J. Fox, J. Gockel, C. Montgomery, R. Yang, H. Qiao, P. Reeseewatt, A. Anvari, S. Narra, and N. Klingbeil. Process mapping for qualification across multiple direct metal additive manufacturing processes. *Solid Freeform Fabrication Proceedings*, pages 655–665, 2013.

[99] N. Shamsaei, A. Yadollahi, L. Bian, and S.M. Thompson. An overview of direct laser deposition for additive manufacturing; part II: Mechanical behavior, process parameter optimization and control. *Additive Manufacturing*, 8:12 – 35, 2015.

[100] D. Zhang, W. Niu, X. Cao, and Z. Liu. Effect of standard heat treatment on the microstructure and mechanical properties of selective laser melting manufactured Inconel 718 superalloy. *Materials Science and Engineering: A*, 644:32 – 40, 2015.

[101] I. Yadroitsava and I. Yadroitsev. Residual stress in metal specimens produced by direct metal laser sintering. *Solid Freeform Fabrication Proceedings*, pages 614–625, 2015.

[102] Emanuel Sachs, Edward Wylonis, Samuel Allen, Michael Cima, and Honglin Guo. Production of injection molding tooling with conformal cooling channels using the three dimensional printing process. *Polymer Engineering & Science*, 40(5):1232–1247, 2000.

[103] E.M. Sachs, M.J. Cima, J.F. Bredt, and S. Khanuja. Process for removing loose powder particles from interior passages of a body, 1996. US Patent 5,490,882.

[104] HKL EBSD - Caltech, center for the science and engineering of materials (CSEM), 2003. `http://ingmat.chem.polimi.it/doc/Workshop%202014-2015%20Seita-ElectronBackscatterDiffraction-08_01_2015.pdf`. Accessed: 2017-01-3.

[105] Buehler sum-met^{TM} the science behind materials preparation: A guide to materials preparation & analysis. 2007 Buehler.

[106] A.J. Schwartz, M. Kumar, B.L. Adams, and D.P. Field. *Electron Backscatter Diffraction in material science.* Springer Science+Business Media, New York, NY, 2 edition, 2009.

[107] D. Stojakovic. Electron backscatter diffraction in materials characterization. *Processing and Application of Ceramics*, 6(1):1– 13, 2012.

[108] N. V. Karthik, H. Gu, D. Pal, T. Starr, and B. Stucker. High frequency ultrasonic non destructive evaluation of additively manufactured components. *Solid Freeform Fabrication Proceedings, Univ. Tex. Austin*, pages 311–325, 2013.

[109] Advanced Photon Source, Argonne National Lab. `https://www.anl.gov/photos/advanced-photon-source`.

[110] A. Cruzado, B. Gan, M. Jimenez, D. Barba, K. Ostolaza, A. Linaza, J.M. Molina-Aldareguia, J. Llorca, and J. Segurado. Multiscale modeling of the mechanical behavior of IN718 superalloy based on micropillar compression and computational homogenization. *Acta Materialia*, 98:242 – 253, 2015.

[111] Microstructural control of additively manufactured metallic materials. *Annual Review of Materials Research*, 46(1):63–91, 2016.

[112] A.A. Antonysamy, J. Meyer, and P.B. Prangnell. Effect of build geometry on the β-grain structure and texture in additive manufacture of Ti6Al4V by selective electron beam melting. *Materials Characterization*, 84:153 – 168, 2013.

[113] M. Tang, C. Pistorius, S. Narra, and J. Beuth. Rapid solidification: Selective laser melting of AlSi10Mg. *The minerals and materials society*, 68(3):960 – 966, 2016.

[114] J. Chambers, W. Cleveland, B. Kleiner, and P. Tukey. *Graphical Methods for Data Analysis*. Wadsworth, 1983.

[115] S.P. Donegan, J.C. Tucker, A.D. Rollett, K. Barmak, and M. Groeber. Extreme value analysis of tail departure from log-normality in experimental and simulated grain size distributions. *Acta Materialia*, 61(15):5595 – 5604, 2013.

[116] Zoran Krstic, Zhengbo Yu, and Vladimir D. Krstic. Effect of grain width and aspect ratio on mechanical properties of Si_3N_4 ceramics. *Journal of Materials Science*, 42(14):5431–5436, 2007.

[117] Sindo Kou. *Welding Metallurgy.* Wiley, NJ, USA, 2nd edition, 2002.

[118] C.A. Stein, A. Cerrone, T. Ozturk, S. Lee, P. Kenesei, H. Tucker, R. Pokharel, J. Lind, C. Hefferan, R.M. Suter, A.R. Ingraffea, and A.D. Rollett. Fatigue crack initiation, slip localization and twin boundaries in a nickel-based superalloy. *Current Opinion in Solid State and Materials Science*, 18(4):244 – 252, 2014. Slip Localization and Transfer in Deformation and Fatigue of Polycrystals.

[119] S. Tammas-Williams, H. Zhao, F. Leoonard, F. Derguti, I. Todd, and P.B. Prangnell. XCT analysis of the influence of melt strategies on defect population in Ti-6Al-4V components manufactured by selective electron beam melting. *Materials Characterization*, 102:47 – 61, 2015.

[120] R. Cunningham, S. P. Narra, T. Ozturk, J. Beuth, and A. D. Rollett. Evaluating the effect of processing parameters on porosity in electron beam melted ti-6al-4v via synchrotron x-ray microtomography. *JOM*, 68(3):765–771, 2016.

[121] H. Gong, H. Gu, K. Zeng, J. J. S. Dilip, P. Deepankar, B. Stucker, D. Christiansen, J. Beuth, and J. J. Lewandowski. Melt pool characterization for selective laser melting of Ti-6Al-4V pre-alloyed powder. *Solid Freeform Fabrication Proceedings, Univ. Tex. Austin*, pages 256–267, 2014.

[122] J. F. Barrett and N. Keat. Artifacts in CT: Recognition and avoidance. *Radiographics*, 24(6):1679–1691, 11 2004. Date revised - 2006-01-01; Last updated - 2011-12-13.

[123] Yuan Tian, Donald McAllister, Hendrik Colijn, Michael Mills, Dave Farson, Mark Nordin, and Sudarsanam Babu. Rationalization of microstructure heterogeneity in Inconel 718 builds made by the direct laser additive manufacturing process. *Metallurgical and Materials Transactions A*, 45(10):4470–4483, 2014.

[124] Modeling the material properties and behavior of Ni-based superalloys. *TMS*, 2004.

[125] J.J. Schirra. Effect of heat treatment variations on the hardness and mechanical properties of wrought Inconei 718. *The Minerals, Metals & Materials Society*, 6:431 – 438, 1997.

[126] Y. Jin, B. Lin, M. Bernacki, G.S. Rohrer, A.D. Rollett, and N. Bozzolo. Annealing twin development during recrystallization and grain growth in pure nickel. *Materials Science and Engineering: A*, 597:295 – 303, 2014.

[127] M. Moiz. The influence of grain size on the mechanical properties of Inconel 718. Master's thesis, 2013.

[128] R. Pokharel, J. Lind, A.K. Kanjarla, R.A. Lebensohn, S.F. Li, P. Kenesei, R.M. Suter, and A.D. Rollett. Polycrystal plasticity: Comparison between grain - scale observations of deformation and simulations. *Annual Review of Condensed Matter Physics*, 5(1):317–346, 2014.

[129] S.K. Mishra, P. Pant, K. Narasimhan, A.D. Rollett, and I. Samajdar. On the widths of orientation gradient zones adjacent to grain boundaries. *Scripta Materialia*, 61(3):273–276, 2009.

[130] S.I. Wright, M.M. Nowell, R. De Kloe, and L. Chan. Orientation precision of electron backscatter diffraction measurements near grain boundaries. *Microscopy and Microanalysis*, 20(3):852–863, 2014.

[131] J. Jiang, T.B. Britton, and A.J. Wilkinson. Accumulation of geometrically necessary dislocations near grain boundaries in deformed copper. *Philosophical Magazine Letters*, 92(11):580–588, 2012.

[132] Y. Takayama and J. A. Szpunar. Stored energy and taylor factor relation in an Al-Mg-Mn alloy sheet worked by continuous cyclic bending. *Materials Transactions*, 45(7):2316–2325, 2004.

[133] S.F. Liu. *Imaging of Orientation and Geometry in Microstructures: Development and Applications of High Energy X-ray Diffraction Microscopy.* PhD thesis, Carnegie Mellon University, 2011.

[134] S. I. Wright and B. L. Adams. Automated lattice orientation determination from electron backscatter Kikuchi diffraction patterns. *Textures and Microstructures*, 14:273–278, 1991. Part 1-2.

[135] A.D. Rollett, F. Wagner, N. Allain-Bonasso, D.P. Field, and R.A. Lebensohn. Comparison of gradients in orientation and stress between experiment and simulation. *Materials Science Forum*, 702-703:463–468, 2012.

[136] D.A. Hughes. Microstructure and flow stress of deformed polycrystalline metals. *Scripta Metallurgica et Materialia*, 27(8):969–974, 1992.